AD

USAAVLABS TECHNICAL REPORT 66-26

DEVELOPMENT OF A METHOD FOR PREDICTING THE PERFORMANCE AND STRESSES OF VTOL-TYPE PROPELLERS

By

A. R. Trenka

June 1966

U. S. ARMY AVIATION MATERIEL LABORATORIES
FORT EUSTIS, VIRGINIA

CONTRACT DA 44-177-AMC-75(T)
CORNELL AERONAUTICAL LABORATORY, INC.
BUFFALO, NEW YORK

Disclaimers

The findings in this report are not to be construed as an official Department of the Army position unless so designated by other authorized documents.

When Government drawings, specifications, or other data are used for any purpose other than in connection with a definitely related Government procurement operation, the United States Government thereby incurs no responsibility nor any obligation whatsoever; and the fact that the Government may have formulated, furnished, or in any way supplied the said drawings, specifications, or other data is not to be regarded by implication or otherwise as in any manner licensing the holder or any other person or corporation, or conveying any rights or permission, to manufacture, use, or sell any patented invention that may in any way be related thereto.

Trade names cited in this report do not constitute an official endorsement or approval of the use of such commercial hardware or software.

Disposition Instructions

Destroy this report when no longer needed. Do not return it to the originator.

DEPARTMENT OF THE ARMY
U. S. ARMY AVIATION MATERIEL LABORATORIES
FORT EUSTIS, VIRGINIA 23604

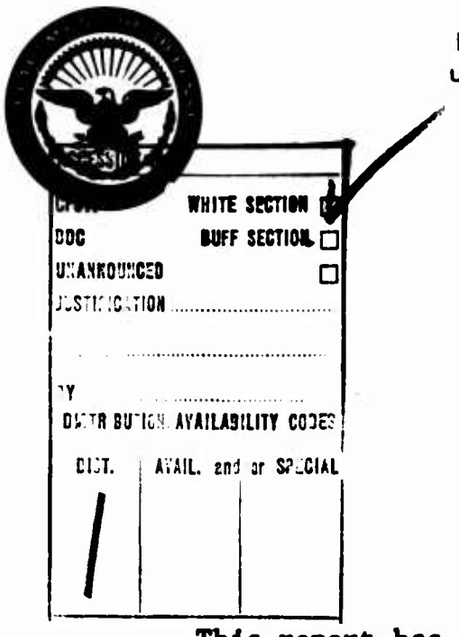

This report has been reviewed by the U. S. Army Aviation Materiel Laboratories, and the results and conclusions are considered to be technically sound. The report is published for the exchange of information and the stimulation of new ideas.

Task 1D121401A142
Contract DA 44-177-AMC-75(T)
USAAVLABS Technical Report 66-26
June 1966

DEVELOPMENT OF A METHOD FOR PREDICTING THE PERFORMANCE AND STRESSES OF VTOL-TYPE PROPELLERS

CAL Report BB-1846-S-1

by

A. R. Trenka

Prepared by
Cornell Aeronautical Laboratory, Inc.
Buffalo, New York

for

U. S. ARMY AVIATION MATERIEL LABORATORIES
FORT EUSTIS, VIRGINIA

SUMMARY

This report presents the initial efforts to develop an improved method for the prediction of performance and stress characteristics of a single VTOL-type propeller-wing-nacelle combination operating in various flight conditions.

The problem of determining the airloads is treated by replacing the propeller blade by a bound vortex of unknown strength and approximating the wake by a mesh of trailing and shed vortex elements.

Engineering beam theory is used to model the elastic behavior of a twisted rotating blade.

An iterative approach is used to solve the aeroelastic equations on a digital computer.

Experimental values of thrust, torque, and blade strains obtained on the propellers of the 0.6-scale model of the XC-142 are presented, along with theoretical results for corresponding flight configurations. However, because of the insufficient accuracy of the experimental data collected, no definite evaluation of the model developed is made.

FOREWORD

The technical effort reported herein was conducted at Cornell Aeronautical Laboratory, Inc., by Mr. Andrew R. Trenka during the period from July 1963 to July 1965. This program was sponsored by the U. S. Army Aviation Materiel Laboratories, Fort Eustis, Virginia, and was administered by Mr. Patrick A. Cancro.

Recognition is given to Dr. I. C. Statler, Mr. R. P. White, Jr., Mr. F. A. DuWaldt, and Mr. R. A. Piziali for their assistance.

The digital program was written by Mr. S. Samet.

Acknowledgement is made to Mr. Stanley O. Dickinson of the National Aeronautics and Space Administration (NASA), whose cooperation during the experimental phase of this work was greatly appreciated.

BLANK PAGE

TABLE OF CONTENTS

LIST OF ILLUSTRATIONS

LIST OF SYMBOLS

a_j	local slope of lift curve for airfoil section $(dc_l/d\alpha)_j$
b_j	local blade semichord, ft
C_j	local blade chord, ft
c_{d_j}	local section drag coefficient
c_{l_j}	local section lift coefficient
$c_{l_{o_j}}$	local section lift coefficient corresponding to α_{o_j}
$c_{m_{c/4_j}}$	local section moment coefficient about quarterchord
d_j	local drag per unit span, lb/ft
h_j	local elastic motions perpendicular to airfoil chord $+V_f \cos\tau$, ft/se
I_j	quasi-steady part of $\Gamma_j + \Gamma_{o_j}$, ft^2/sec
l_j	local lift per unit span, lb/ft
M	number of vibration modes
m_j	local moment per unit span, ft-lb/ft
$\overline{NA}$	number of azimuthal stations
$\overline{NC}$	number of blades
NF	normal force, lb
$\overline{NR}$	number of radial stations
PM	pitching moment, ft-lb
p	number of harmonics
Q	torque, ft-lb
SF	side force, lb
T'	time for one rotor revolution, sec
T	thrust, lb
V_j	local total velocity at a blade section, ft/sec
V_f	free-stream velocity, ft/sec
v_j	local total velocity perpendicular to the airfoil chord, ft/sec
v_j^I	local velocity perpendicular to airfoil chord due to wake, ft/sec
v_j^N	local velocity perpendicular to airfoil chord due to nacelle, ft/sec
v_j^W	local velocity perpendicular to airfoil chord due to wing, ft/sec

ω_j	local elastic displacement of the elastic axis perpendicular to the prop plane, ft
X_j	radial distance to j^{th} element, ft
X_o, Y_o, Z_o	nonrotating coordinates fixed at prop hub.
X, Y, Z	rotating coordinates aligned with the blade
YM	yawing moment, ft-lb
α_{e_j}	local effective angle of attack, radians
α_F	angle of attack of fuselage, deg.
α_f	angle of attack of flap, deg.
α_{I_j}	angle local total velocity makes with the prop plane, radians
α_{o_j}	local reference angle of attack, radians
α_P	flap angle, deg.
α_w	angle of attack of wing, deg.
α_Y	yaw angl he fuselage, deg.
β_j	local built-in twist, radians
Γ_j	local bound vortex strength, ft^2/sec
Γ_{o_j}	local bound vortex strength corresponding to α_{o_j}, ft^2/sec
Γ_W	strength of wing bound vortex, ft^2/sec
ϵ_j	local distance from elastic axis to quarterchord, ft
θ_j	local total geometric angle ($=\beta_j + \phi_j$) of a blade section, radians
ρ	density of air, $slugs/ft^3$
$\bar{\sigma}_{ij}$	geometric portion of Biot-Savart law for the effect of the i^{th} vortex element at the j^{th} point, $1/ft$
τ	angle free-stream velocity makes with thrust axis, deg
ϕ_j	local torsional displacement, radians
ψ	azimuthal position of the blade, deg.
Ω	rotor speed, radians/sec

BLANK PAGE

INTRODUCTION

With the advent of VTOL aircraft, more stringent requirements were placed on the designer's ability to predict accurately the static thrust and torque characteristics of propellers. The static thrust and torque had to be predicted much more accurately than was heretofore considered acceptable. Now, the accuracy with which these quantities are predicted may well determine whether the aircraft will fulfill its anticipated role as a VTOL vehicle. Since the entire lifting capability rests on the propellers, a small underestimate of the thrust might greatly reduce the payload.

In addition to the performance prediction problems, oscillatory stresses of unexpectedly large amplitudes were observed on the propellers of such VTOL aircraft during wind-tunnel and full-scale tests. In particular, these stresses were noted in the transitional range from a hover to an axial flight configuration.

Propeller designers suddenly found themselves reexamining "tried and true" propeller performance and stress theories and finding them to have, at best, questionable applicability. No proven theoretical approach was available for the skewed flight range in which high oscillatory stresses were observed. Furthermore, they found that much of the experimental data upon which previous correlation with theory had been based were not sufficiently accurate to aid in the development of more accurate theories or in the extension of existing ones.

The U. S. Army's recognition of these problems and Cornell Aeronautical Laboratory's (CAL) previous work in rotary-wing aircraft (as exemplified by References 1, 2, 3, 5, 6, 8, 9, 10, and 11) led to the effort reported herein. The purpose of the effort was to develop an improved method for predicting the performance and stresses of VTOL-type propellers through their entire flight range. The basic

method developed by Cornell Aeronautical Laboratory and reported in Reference 11 for the prediction of rotary-wing airloads in hovering and forward flight was modified, extended, and applied to the problem of VTOL-type propellers.

The program undertaken was twofold. On the one hand, a theoretical method was developed, while on the other, experimental data were gathered in an attempt to provide a consistent set of performance and stress data of high accuracy for correlation with theory.

Throughout this report the term performance will be synonymous with the mean forces and moments acting on the shaft; namely, thrust, torque, normal and side force, and pitching and yawing moment.

THEORETICAL PROGRAM

STATEMENT OF THE AEROELASTIC PROBLEM

Solution of the aeroelastic problem requires a knowledge of the interaction of the aerodynamic, elastic, and inertial forces acting on a wing section. Once these interactions are known, the loads and motions of the section, and hence the total wing loads and motions, may be determined. The problem is a difficult one for conventional wings. For rotary wings, i.e., propeller blades, the problem is compounded by the nature of the wake shed from the blades, which now takes on the geometry of a distorted helix; by the rotation-induced elastic coupling between various blade motions; and by the complicated inertia loads which arise when motions occur in a rotating frame.

In addition, there are interference effects from wings and nacelles which lie in the slipstream and which may be quite close to the propeller plane. To define the interaction of these forces, the following aerodynamic and structural models were employed. (The discussion will be limited to steady-state flight.)

Aerodynamic Model

The aerodynamic model accounts for the effects on the blade of (1) a distorted wake, (2) a wing and nacelle lodged in the propeller slipstream, (3) forward flight, and (4) blade deformations under load.

The entire model rests upon periodicity and the ability to predict the wake position with sufficient accuracy.

Representation of the Blade

The blade is represented by a bound vortex of strength, Γ, placed at the blade quarterchord. The Γ of the bound vortex varies both with radius and with time. Since steady-state flight conditions only are

being considered, the time variation is periodic of period T'. T' is the time for one rotor revolution; hence, the time variation of Γ is equivalent to the azimuthal variation. Thus, the radial and azimuthal variations of Γ are given by $d\Gamma/dX$ and $d\Gamma/d\psi$ (X is the radial position and ψ is the azimuthal angle), respectively. The radial distribution is represented by breaking the bound vortex up into $\overline{NR}$ spanwise segments of constant Γ. The azimuthal variation is similarly accounted for by allowing each radial segment to assume a new value of Γ as it is stepped through $\overline{NA}$ azimuthal stations. Thus, the radial and azimuthal variation of Γ is represented by ($\overline{NR} \times \overline{NA}$) values of Γ. The magnitude of Γ is determined by requiring that the chordwise boundary condition of zero normal velocity at the three-quarterchord of the blade be satisfied.

Representation of the Wake

Because of the variation of Γ with X and ψ, a continuous sheet of vorticity is deposited into the wake. Because of the steady-state flight conditions, the variation of Γ with X and ψ is repeated for each and every blade revolution. The wake is represented in a fashion analogous to the representation of the bound Γ distribution. The continuous wake is modeled by a mesh of "trailing" and "shed" vortex elements. The "trailing" vortex element is deposited in the wake from the ends of the segmented bound vortex and is equal to the difference between adjacent bound Γ's. A "shed" vortex is deposited in the wake from each bound vortex element as the blade moves from one azimuthal position to the next. Its strength is equal to the difference between bound Γ's at successive azimuthal positions. Thus, if a given trailing vortex is followed back into the wake, it is found that its strength varies in a stepwise fashion. It is constant for the interval corresponding to the increment between successive azimuthal positions of the blade. Similarly, consider the shed vortex deposited in the wake at some azimuthal position. It varies in stepwise fashion along its

span. The variation corresponds to the spanwise variation of the bound vortex which existed on the blade when the blade was in that azimuthal position.

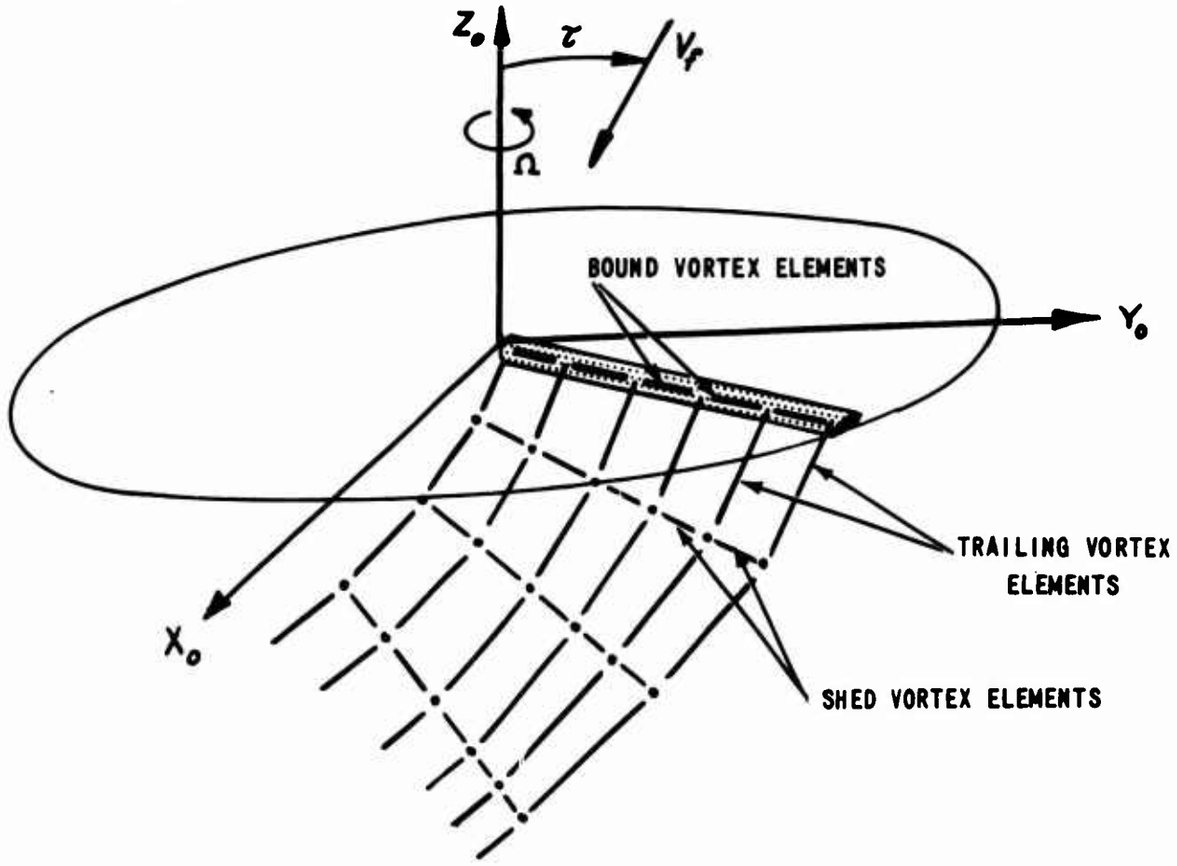

Figure 1. PICTORIAL REPRESENTATION OF BLADE WAKE MESH

Thus, the continuous sheet of vorticity deposited in the wake has been replaced by a mesh of shed and trailing vortex elements whose strengths are proportional to the strength of the bound vortex. This mesh is repeated in a continuous fashion once per revolution of the blade and for each blade in the propeller set.

Now, consider the problem: "How is the wake positioned relative to the blades which generated it?" The wake position is determined by the interplay of such effects as (1) self-induced velocities of the wake, (2) free-stream velocity, and (3) interference velocities from wings, nacelles, fuselages, etc., in and in the proximity of the slipstream. The present method attempts to account for the

effects of (1) wake contraction and radial and axial variation of the wake velocity, (2) free-stream velocity, and (3) the perturbing effect of a wing and nacelle completely immersed in the slipstream.

The wake contraction and axial and radial velocity variation is estimated for hovering flight by using a system of finite-core, ring vortices. The theory was developed at CAL under Office of Naval Research sponsorship and is reported in detail in Reference 1. Briefly, the approach replaces the slipstream by an axial system of discrete, finite-core, ring vortices. The system is treated as a starting problem by periodically releasing a new vortex ring in the reference plane while allowing the individual rings to move under mutual influence according to the laws of vortex dynamics. After a sufficient number of rings have been released, a stabilized trajectory is determined down which all successive rings move. The solution was obtained using a digital approach, and the program output yields a time history of the coordinates and velocities of all vortex rings.

This model was applied to the propeller slipstream problem in which the wake is treated as a mesh. The tip-trailing vortex was assumed to move down the surface generated by the stabilized ring vortex trajectory. This was done by requiring that the tip vortex move with the velocities with which the rings move. Thus, at the tip of the blade, the trailing vortex was deposited in the wake with the velocities of the ring at the instant the ring was deposited in the reference plane which now corresponds to the prop plane. This tip vortex, then, was allowed to move for the interval of time corresponding to $1/N\overline{A}$ rotor revolutions. At the end of this period, it would assume new values of velocities corresponding to the velocities which the ring experienced at that position in the wake, and so on down the wake. Since the ring velocity distribution is axially symmetric, tip vortices deposited at various azimuthal stations all move down the wake with the same velocity time history but are displaced in time with respect to one another (see Figure 2).

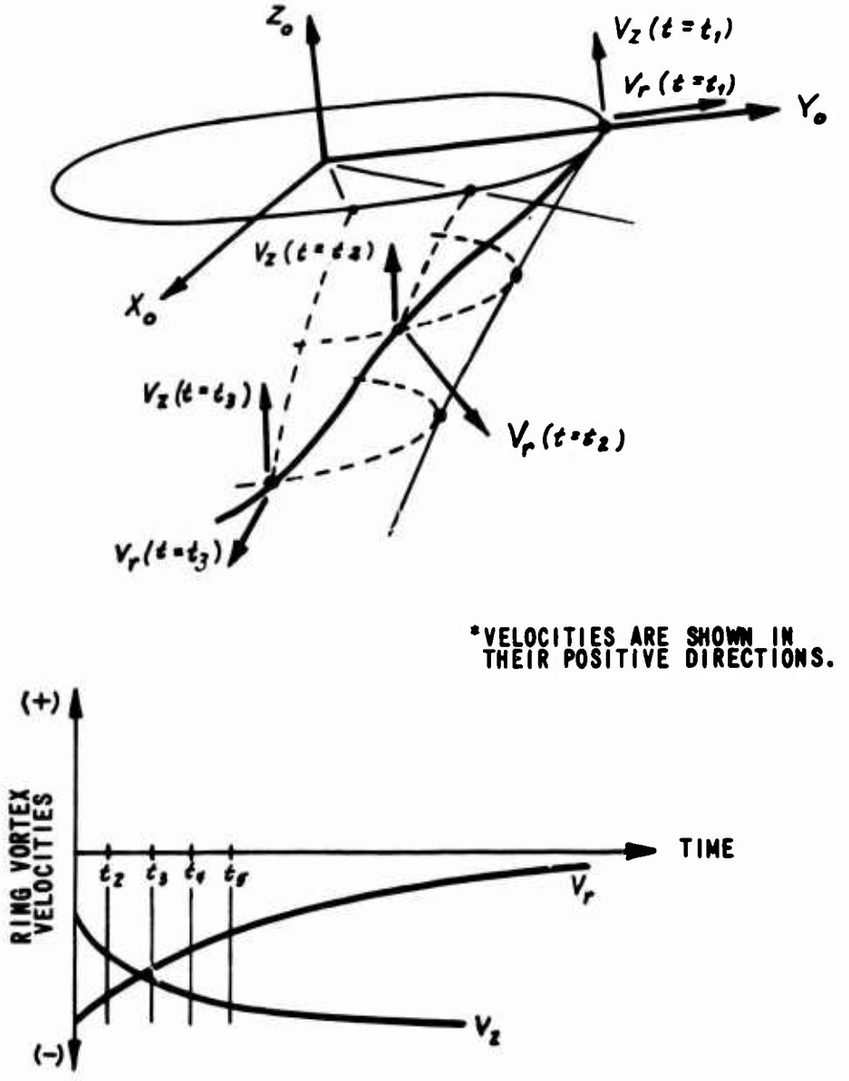

Figure 2. PICTORIAL REPRESENTATION OF TIP VORTEX MOVING DOWN RING VORTEX TRAJECTORY

The result is a tip helix of va ying pitch and diameter.

To place the mesh interior to the tip elements, it was assumed that (1) all interior elements move with the same axial velocity as the tip vortex element, and (2) the radial velocity of the interior elements is proportional to the product of the radial position of the

element and the radial tip velocity.

There is no mechanism, at present, to allow for a tangential, or swirl, component of velocity.

This wake model will be referred to as the RVM (ring vortex model).

The wake, as positioned by the RVM, is used as a base from which small perturbations due to the free stream, wing, and nacelle are allowed in the case of low forward speeds. These perturbations are included as incremental velocities at each control point in the wake (as determined from the RVM).

Thus, in the hovering condition, a distorted wake is used which includes the effects of contraction, radial and axial velocity variations, and interference effects from wing and nacelle. For the initial stages of transition, i. e., low forward speeds, the free stream is included as an additional perturbation. For higher forward velocities, the model postulated above breaks down, and the wake is treated as a skewed helix of uniform pitch, with none of the effects of contraction or of the wing and nacelle. However, if a wake shape, i. e., position, is known for a given flight condition, it can be included in the program.

For details of the mathematical model, see Appendix I, page 55.

Representation of the Wing and Nacelle

The interference effects of the wing and nacelle can be treated in terms of, first, their direct effect on the angle of attack at the propeller and, second, their effect in distorting the wake. The direct effect is always included when applicable. The second effect is included only in the hovering and low forward speed transition cases.

To model the nacelle, it was assumed that its effects could be adequately approximated by treating it as a Rankine body (source-sink combination). The Rankine body length was taken equal to the nacelle length, and the Rankine body diameter was taken such that its projected frontal area equals that of the nacelle.

The wing was simply treated as a bound vortex placed at the wing quarterchord. For details of the mathematical model of the wing and nacelle, see Appendix II, page 60.

Development of the Mathematical Model of the Propeller and Wake

The equations which will eventually give the aerodynamic forces required for the aeroelastic problem will now be developed. The equations will be formulated in terms of the strength of the bound vortex Γ. Consider an element of a blade of a propeller in skewed flight with a wing and nacelle immersed in the propeller slipstream (see Figure 3).

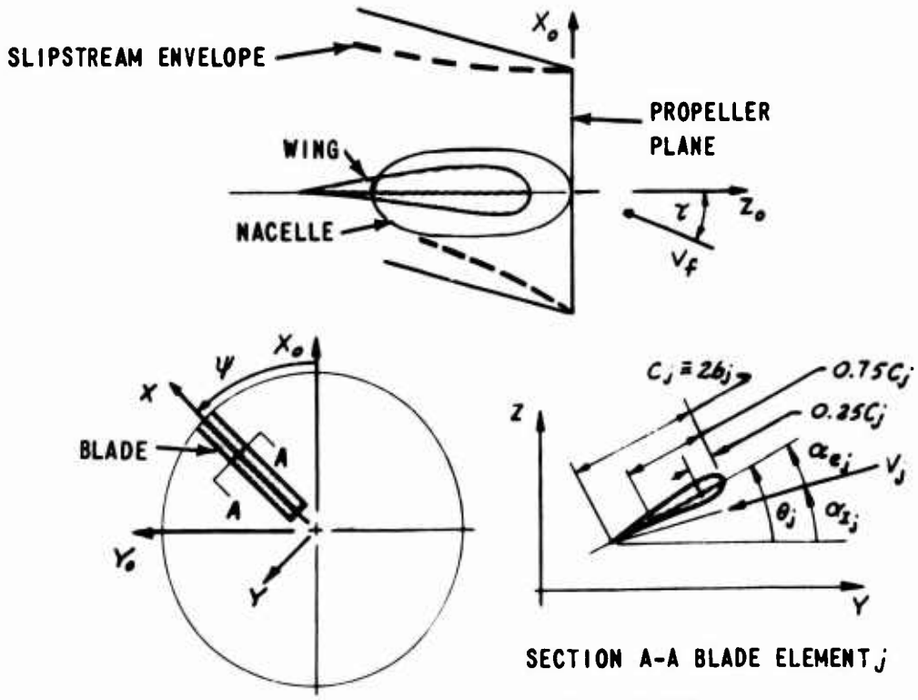

Figure 3. GEOMETRY FOR AERODYNAMIC MODEL OF PROPELLER, WING, AND NACELLE

The lift per unit length on this j^{th} blade element is

$$\ell_j = \rho V_j \Gamma_j \tag{1}$$

where

ρ = fluid density
V_j = local total velocity
Γ_j = local vortex strength

But ℓ_j can also be written as

$$\ell_j = b_j \rho V_j^2 c_{\ell_j} \tag{2}$$

where

c_{ℓ_j} = local section lift coefficient
b_j = local blade semichord

Then from (1) and (2),

$$\Gamma_j = b_j V_j c_{\ell_j} . \tag{3}$$

The section lift coefficient, c_{ℓ_j}, is a nonlinear function of the effective angle of attack, α_{e_j}. To allow for this nonlinearity, as well as to provide a mechanism by which Reynolds number and Mach number effects can be introduced, the c_{ℓ_j} curve was expanded in a Taylor series about an arbitrary reference angle α_{o_j}; i.e.,

$$c_{\ell_j} = \left[c_{\ell_o} + \left.\frac{dc_\ell}{d\alpha}\right|_{\alpha_o} (\alpha_e - \alpha_o) + \frac{1}{2} \left.\frac{d^2 c_\ell}{d\alpha^2}\right|_{\alpha_o} (\alpha_e - \alpha_o)^2 + \cdots \right]_j . \tag{4}$$

It is now required that

$$(\alpha_e - \alpha_o)_j << 1,$$

and, hence, terms higher than $(\alpha_e - \alpha_o)_j$ may be neglected in Equation (4).

Thus, Equation (3) becomes

$$\Gamma_j = b_j V_j \left[c_{\ell_o} + \frac{dc_\ell}{d\alpha}\bigg|_{\alpha_o} (\alpha_e - \alpha_o) \right]_j . \tag{5}$$

Equation (5) is regrouped to get

$$\Gamma_j = \Gamma_{o_j} + b_j V_j a_j \alpha_{e_j} \tag{6}$$

where

$$\Gamma_{o_j} = b_j V_j \left[c_{\ell_o} - \frac{dc_\ell}{d\alpha}\bigg|_{\alpha_o} \alpha_o \right]_j$$

$$a_j = \frac{dc_\ell}{d\alpha}\bigg|_{\alpha_{o_j}} .$$

The assumption is now made that

$$\sin \alpha_{e_j} \approx \alpha_{e_j} .$$

This approximation leads to a maximum error in lift of approximately 2% when $\alpha_{e_j} = 20^\circ$. Since α_{e_j} will generally be much less than 20°, it was felt that this assumption would not significantly limit the validity of the theory.

From Figure 3, it is recognized that

$$V_j \alpha_{e_j} \approx V_j \sin \alpha_{e_j} \equiv v_j .$$

From lifting-line theory, v_j must be the velocity perpendicular to the airfoil chord at the three-quarterchord point. Its sense must be positive up to give increased lift for increased α_j. Equation (6) now becomes

$$\Gamma_j = \Gamma_{o_j} + b_j a_j v_j . \tag{7}$$

The perpendicular velocity includes contributions from free stream, wake, nacelle, wing, and blade elastic motions; thus,

$$v_j = \left[(X\Omega + V_f \sin\tau \sin\psi)\sin\theta - \dot{h} + v^W + v^N + v^I\right]_j \qquad (8)$$

where, for the j^{th} blade element,

X_j = radial distance from centerline of rotation to j^{th} blade element

Ω = rotor speed

θ_j = total geometric angle including built-in twist, β_j , and elastic motions, ϕ_j, of the j^{th} blade element

$\dot{h}_j$ = $V_f \cos\tau\cos\theta$ + elastic motions perpendicular to the airfoil chord of the j^{th} blade element

v_j^W = velocity due to wing perpendicular to chord of j^{th} blade element

v_j^N = velocity due to nacelle perpendicular to chord of j^{th} blade element

v_j^I = velocity due to wake perpendicular to chord of j^{th} blade element.

Using the Biot-Savart law applied to the wake mesh, the velocity perpendicular to the airfoil chord induced by the wake can be written as

$$v_j^I = \sum_{i=1}^{\infty} \bar{\sigma}_{ij}\,\gamma_i \qquad (9)$$

where

$\bar{\sigma}_{ij}$ = the geometric portion of the Biot-Savart law for the effect of the i^{th} element at the j^{th} point

γ_i = strength of the i^{th} wake element of vorticity.

For a detailed derivation of Equation (9), see Appendix III, page 64.

Recall that the γ's of the wake are proportional to the Γ's of the blade bound vortices at various radial and azimuthal positions. Hence, when Equation (9) is substituted into Equation (8) and the wake terms regrouped, the following is obtained from Equation (7),

$$\left[b_j a_j \sigma_{jj} - 1\right] \Gamma_j + b_j a_j \sum_{\substack{i=1 \\ i \neq j}}^{\infty} \sigma_{ij} \Gamma_i = - I_j \qquad (10)$$

where

$$I_j = \Gamma_{o_j} + b_j a_j \left[(X\Omega + V_f \sin\tau \sin\psi)\sin\theta - \dot{h} + v^w + v^N\right]_j ,$$

and σ_{ij} results from a regrouping of the $\bar{\sigma}_{ij}$'s.

Equation (10) was written for one blade element at one azimuthal position. Since Γ_j changes with radius and azimuth, similar equations for all values of Γ_j can be written. Since Γ_j is limited to ($\overline{NR} \times \overline{NA}$) values, ($\overline{NR} \times \overline{NA}$) simultaneous algebraic equations in Γ_j result.

In matrix notation,

$$[\sigma]\{\Gamma\} = \{I\} \qquad (11)$$

where

$[\sigma]$ is a square matrix of order ($\overline{NA} \times \overline{NR}$) whose diagonal elements have the form

$$\left[b_j a_j \sigma_{jj} - 1\right]$$

and whose off-diagonal elements have the form

$$b_j a_j \sigma_{ij}$$

$\{\Gamma\}$ is a column matrix of the unknown Γ_j

$\{I\}$ is a column matrix of the known quantities

$$-\left[\Gamma_{o_j} + b_j a_j \left[(X\Omega + V_f \sin\tau \sin\psi)\sin\theta - \dot{h} + v^w + v^N\right]_j\right] .$$

At this point in the development, let it suffice to say that everything in Equation (11) is known, except the Γ_j's. Hence, if the matrix Equation (11) can be solved for the Γ_j's, then sufficient information will be available to generate the required aerodynamic forces in the aeroelastic problem.

Summary of Assumptions

To develop Equation (11), the following assumptions have been made:

(1) The propeller-wing-nacelle combination is in steady-state flight.

(2) The propeller blade can be represented aerodynamically as a bound vortex placed at the quarterchord.

(3) The radial and azimuthal variation of Γ can be represented by a finite series of discrete values.

(4) The continuous wake can be represented as a mesh of concentrated shed and trailing vortex elements.

(5) $\sin \alpha_e \approx \alpha_e$.

(6) The wake position can be computed.

(7) The wing can be represented by a concentrated vortex at its quarterchord.

(8) The nacelle can be represented as a Rankine body.

Structural Model

To determine the inertia and elastic forces required for the aeroelastic problem, a Lagrangian approach was used. Following the development of Reference 7, the kinetic and potential energy of a twisted rotating beam was written. A dissipation term proportional to the elastic displacement and in phase with the elastic velocity was written to account for structural damping forces. The elastic displacements were then expanded in terms of the normal modes

of the blades, and the Lagrangian was applied. Since the forcing function of the system, i.e., aerodynamic load, is periodic with its fundamental frequency being Ω, the steady-state response of the linearized system must be periodic of fundamental frequency Ω. Hence, both the motions and the generalized forces were expanded in a Fourier series on Ω. Then, by the uniqueness theorem for trigonometric series, corresponding coefficients must be equal. The result is a set of $2M$ (where M is the number of modes retained) simultaneous algebraic equations in the Fourier coefficients (of sine and cosine components) of the motions for each of p harmonics. The zeroth harmonic has only M simultaneous equations, since there are no corresponding sine terms in the series.

For the purpose of this study, six degrees of freedom were used – the first four coupled bending modes and the first two uncoupled torsion modes. A detailed development of these equations and the results are presented in Appendix IV, page 69. A detailed developement of the generalized forces is presented in Appendix V, page 79.

The following assumptions were made in defining the structural model:

(1) Simple beam theory was applicable.
(2) Airfoil cross sections were symmetrical with respect to the major neutral axis; hence, the center of gravity lay on this axis.
(3) Gravity forces were negligible.
(4) Flight conditions were steady state.
(5) Damping (structural) was proportional to the elastic displacement and in phase with the elastic velocity.
(6) Blade elastic deformations were small.
(7) The blades were effectively cantilevered, and the hub had infinite impedance.

All the forces required for the aeroelastic problem of a propeller in transitional steady-state flight have now been defined. There now remains the problem of solving the resultant set of

simultaneous equations for the loads and motions.

SOLUTION OF THE AERO. ASTIC PROBLEM

Iterative Solution

An iterative approach to the solution was adopted. First, the Γ - equations are solved for an assumed set of motions. The resultant loads are then used to compute the generalized forces for the equations of structural deformation of the blade. The equations of blade deformation are treated as a forced response problem, and new motions are determined. Since, in general, the new motions do not agree with the assumed set, the Γ -equations must be resolved using the new motions. The process is repeated until the Γ's and blade elastic motions from the n^{th} iteration agree with the Γ's and blade elastic motions from the $(n+1)^{th}$ iteration to within some specified tolerance. At this point, it is argued that a consistent set of loads and motions have been obtained, since no change in either occurs with iteration. Further, since the problem has a unique solution, this must be it.

The iterative path between the loads (the Γ -equations) and motions (the structural equations) is interrupted because of the nonlinear character of the c_ℓ curve. Recall, from page 10, Equation (4), that the c_ℓ was expanded in a Taylor series about some known reference angle of attack α_0 . So long as, from iteration to iteration, $\alpha_0 \approx \alpha_e$, to within some amount ($\pm\Delta\alpha$, say), the same α_0 , a, and c_{ℓ_0} are used in the Γ -equations in each iterative step. If $\alpha_0 + \Delta\alpha < \alpha_e$ or $\alpha_0 - \Delta\alpha > \alpha_e$, a new α_0 is determined, and hence a new a and c_{ℓ_0} , for use in the Γ -equations in the next iterative step. This is accomplished by dividing the c_ℓ vs. α curve into a series of increments in α . At the center of each is evaluated α_0 , a, and c_{ℓ_0} . Then, as each new α_e is determined, it is checked to see if it lies in the range corresponding to the α_0 used to compute it (i. e., does $\alpha_0 - \Delta\alpha \leq \alpha_e \leq \alpha_0 + \Delta\alpha$). If not, it is placed in the proper range, and the iteration is continued. The process is described in the logic diagram, Figure 4.

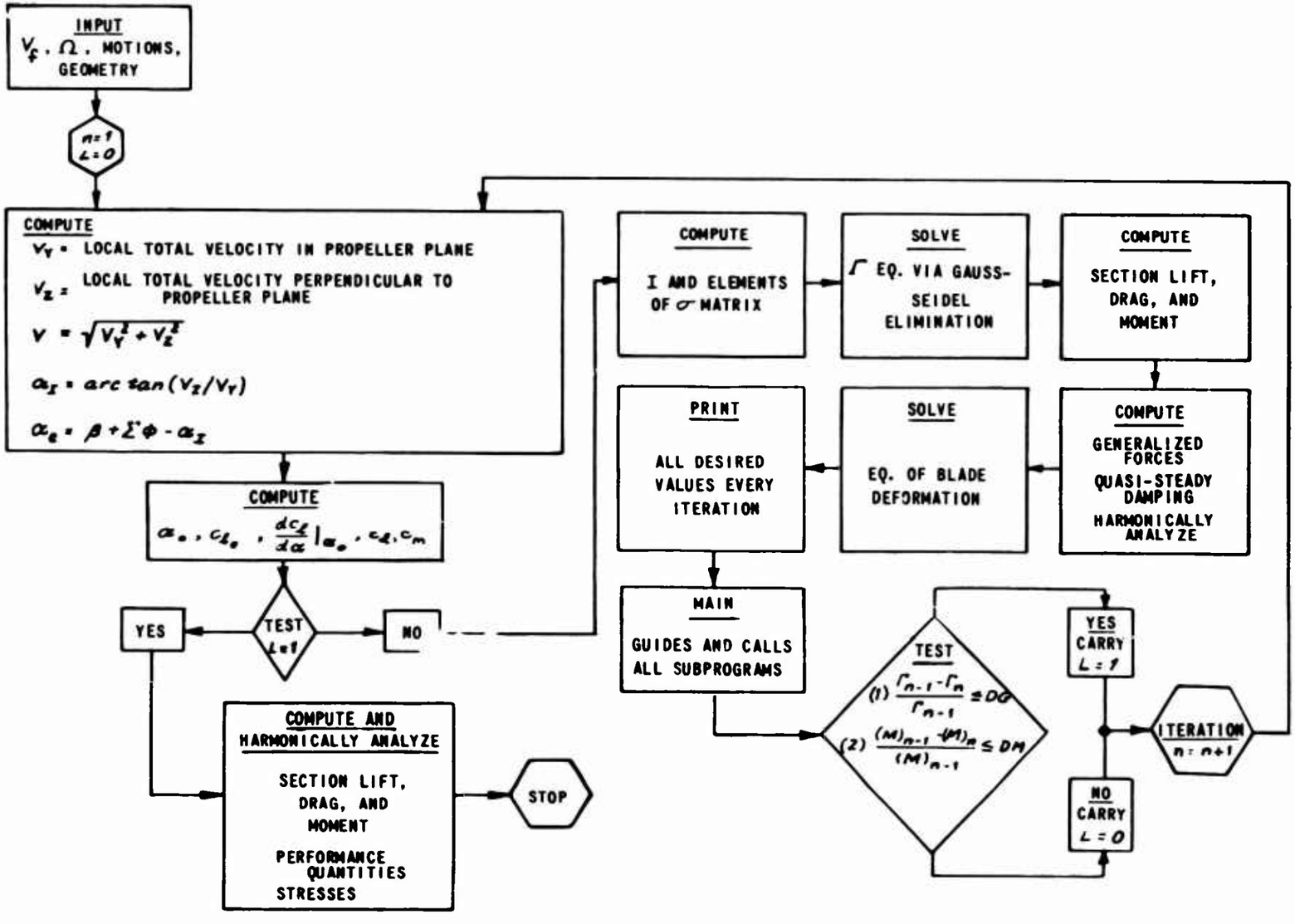

Figure 4. LOGIC DIAGRAM

To insure convergence of the iterative scheme employed to solve the equations of motion, it was found that the right-hand side, i. e. the generalized force, should be relatively free from a dependence upon the dependent variables, i. e., the elastic motions. In the present development it is impossible to extract this dependence of the generalized force on the motions. It was proposed to accomplish this artificially by subtracting from both sides of the equations of blade deformation the contribution from an approximation to the quasi-steady damping. This term was chosen because it is one of the largest motion-dependent contributors to the generalized force.

The term to be subtracted from both sides of the equations of blade deformation is derived in Appendix VII, page 94. The treatment of this term in the equations of blade deformation differs depending upon whether we consider the right- or the left-hand side of these equations. On the right-hand side, the motions are assumed known from the previous iterative step. On the left-hand side, the deformations are the unknowns to be used in the succeeding iterative step. For example, consider the following representation of the deformation equation at the $(n+1)^{th}$ iteration:

$$m\ddot{X}_{n+1} + k\dot{X}_{n+1} + CX_{n+1} = F_n$$

where F_n is assumed to be a linear function of the elastic motions determined in the n^{th} iteration; i. e.,

$$F_n = C_0 + C_1\ddot{X}_n + C_2\dot{X}_n + C_3X_n .$$

Subtract $C_2\dot{X}_{n+1}$ from the left-hand side and $C_2\dot{X}_n$ from the right-hand side of the equation to obtain

$$m\ddot{X}_{n+1} + [k-C_2]\dot{X}_{n+1} + CX_{n+1} = F_n - C_2\dot{X}_n .$$

When the iterative process has converged,

$$X_n = X_{n+1} \pm \epsilon$$

where

$\epsilon \leq \sigma$ = predetermined allowable error.

Then

$$m\ddot{X}_{n+1} + k\ddot{X}_{n+1} + CX_{n+1} \approx F_n ,$$

and the solution is effected.

Performance and Stresses

Once a converged set of Γ's and motions have been obtained, there only remains the proper combination of these quantities to obtain the forces acting on the propeller shaft and the blade stresses. The prop thrust, torque, normal force, side force, pitching moment, and yawing moment are then determined (see Figure 5).

Section lift, drag, and torsional moment (ℓ_j, d_j, m_j respectively) are computed at each radial and azimuthal position of the blade based on the converged loads and motions. These quantities are resolved into components with respect to the inertial coordinate system (X_o, Y_o, Z_o). At each azimuthal position, a summation of the spanwise integration over each blade yields the instantaneous values of the thrust, torque, etc. This process is repeated for all azimuthal positions. The result is a set of $\overline{NA}$ values of each of the performance quantities. Hence, with $\overline{NA}$ equally spaced azimuthal positions, the performance quantities may be represented by a finite Fourier series of $\overline{NA}$ terms, the zeroth term of which yields the desired mean values over one revolution:

$$THRUST = T = \frac{1}{\overline{NA}} \sum_{k=1}^{\overline{NA}} \left\{ \sum_{a=1}^{\overline{NC}} \left[\sum_{j=1}^{\overline{NR}} (F_{Z_j}) \Delta X_j \right]_a \right\}_k \tag{12}$$

$$TORQUE = Q = -\frac{1}{\overline{NA}} \sum_{k=1}^{\overline{NA}} \left\{ \sum_{a=1}^{\overline{NC}} \left[\sum_{j=1}^{\overline{NR}} (X_j F_{Y_j}) \Delta X_j \right]_a \right\}_k \tag{13}$$

$$NORMAL\ FORCE = NF = +\frac{1}{\overline{NA}} \sum_{k=1}^{\overline{NA}} \left\{ \sum_{a=1}^{\overline{NC}} \left[\sum_{j=1}^{\overline{NR}} (F_{X_j} \cos\psi - F_{Y_j} \sin\psi) \Delta X_j \right]_a \right\}_k \tag{14}$$

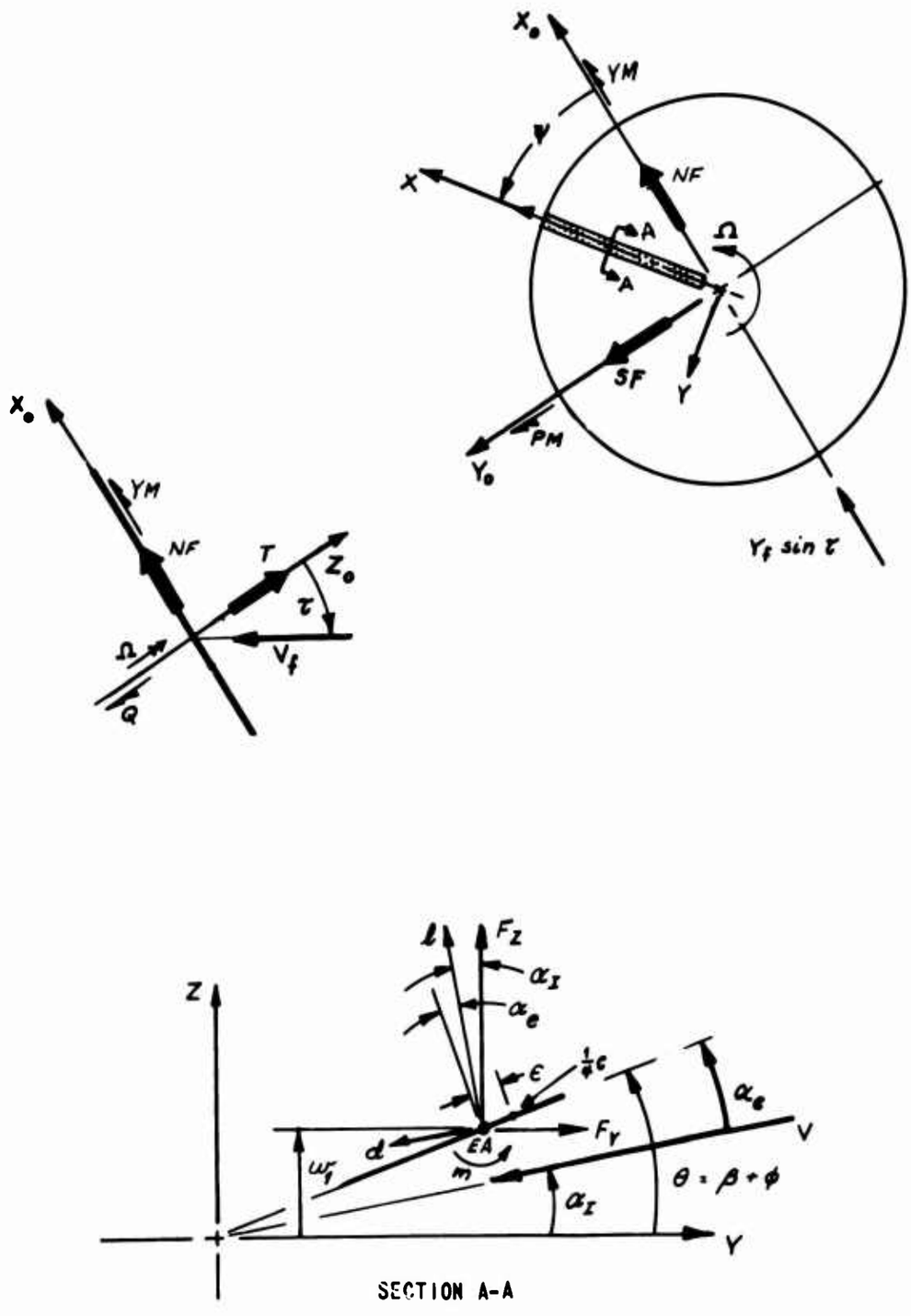

Figure 5. GEOMETRY FOR DETERMINATION OF PERFORMANCE AND STRESSES

$$\text{SIDE FORCE} = SF = \frac{1}{\overline{NA}} \sum_{k=1}^{\overline{NA}} \left\{ \sum_{s=1}^{\overline{NC}} \left[\sum_{j=1}^{\overline{NR}} (F_{x_j} \sin\psi + F_{y_j} \cos\psi) \Delta X_j \right]_s \right\}_k \tag{15}$$

$$\text{PITCHING MOMENT} = PM = \frac{1}{\overline{NA}} \sum_{k=1}^{\overline{NA}} \left\{ \sum_{s=1}^{\overline{NC}} \left[\sum_{j=1}^{\overline{NR}} (F_{z_j} X_j \cos\psi - m_j \sin\psi) \Delta X_j \right]_s \right\}_k \tag{16}$$

$$\text{YAWING MOMENT} = YM = \frac{1}{\overline{NA}} \sum_{k=1}^{\overline{NA}} \left\{ \sum_{s=1}^{\overline{NC}} \left[\sum_{j=1}^{\overline{NR}} (F_{z_j} X_j \sin\psi + m_j \cos\psi) \Delta X_j \right]_s \right\}_k \tag{17}$$

where

k = azimuthal station number

s = blade number

$\overline{NA}$ = total number of azimuthal stations

$\overline{NC}$ = number of blades

$F_{x_{j_s}} = -\ell_j (dw/dX)_j$ on blade s

$F_{y_{j_s}} = -\left[\ell \sin\alpha_I + d \cos\alpha_I \right]_j$ on blade s

$F_{z_{j_s}} = \left[\ell \cos\alpha_I - d \sin\alpha_I \right]_j$ on blade s

$m_{j_s} = \left[2b^2 \rho V^2 c_{m_{c/4}} \right]_j + \epsilon_j \left[\ell \cos\alpha_e + d \sin\alpha_e \right]_j$ on blade s

$c_{m_{c/4_j}}$ = section moment coefficient about airfoil quarterchord.

A detailed development of the stresses at any point in the blade is presented in Appendix VI, page 86. Consistent with the structural model adopted, i. e., simple beam theory, only the longitudinal and shear stresses are developed at any point in the blade cross section. These quantities are also harmonically analyzed.

The Digital Program

The entire iterative approach to the solution of the aeroelastic problem has been programmed in FORTRAN IV for use on the IBM 7044 digital computer. The program consists of six main parts.

Part 1

This program positions the wake. The coordinates of the elemental wake vortex end points are computed. These coordinates are computed, including the effects of (1) free-stream velocity, (2) wake contraction, (3) wing interference, and (4) nacelle interference in any combination desired. The midpoints of the bound vortex elements are also computed. The program can handle 24 azimuthal stations and 10 radial stations.

Part 2

From the coordinates obtained in Part 1, the effect of the wake vortices of unit strength on the blades is computed, i. e., the $\overline{\sigma}$ of each individual wake element. The proper combinations are made, and the elements which contribute to the $[\sigma]$ matrix of Equation (11) are computed.

Part 3

Part 3 evaluates all the mass and elastic integrals necessary for computing the elements of the structural deformation equations. It also writes the coefficients of the least-square polynomial fit to the two-dimensional airfoil section data used to evaluate α_o , a , c_{ℓ_o} , c_m, and c_d . The mass-elastic integrals can be evaluated at a maximum of 30 spanwise stations.

Part 4

From the aerodynamic data of Part 3 and the σ elements of Part 2, the $[\sigma]$ matrix of Equation (11) is formed. The set of simultaneous equations is solved by using the Gauss-Siedel reduction technique (Reference 13). The technique is one of iteration until the set of Γ's from one iteration agrees with the previous set to within some prespecified tolerance. The generalized force is then computed and approximated by an n^{th} order polynomial in χ. This is required by the fact that the lift is computed at only 10 spanwise stations, while the mass-elastic properties are known at up to 30 stations.

The generalized forces are harmonically analyzed for a fundamental period of one propeller revolution, and the equations of deformation for each harmonic are solved by employing the Gauss elimination process (Reference 13).

Overall convergence tests on Γ's and deformations are made by comparing values obtained in the n^{th} iteration to those obtained in the $(n+1)^{th}$ iteration.

If the Γ's and deformations are not converged, α_e and α_I are recomputed and the aerodynamic tapes are searched to determine if the same α_o is to be used. Control is returned to Part 3 or continues to Part 5, depending upon the results of the convergence tests.

Part 5

Part 5 computes a time history of the propeller thrust, torque, side and normal forces, pitching and yawing moments, and stresses. These quantities are also harmonically analyzed. The printed output from the program includes the following distributions given as functions of the radial and azimuthal position in the disk: (1) strength of bound vorticity, (2) section lift, drag, and moment, (3) section displacement (total), (4) section effective angle of attack,

(5) section induced velocity, and (6) section stresses – longitudinal and shear. Also printed is the azimuthal distribution of (7) thrust, (8) torque, (9) normal and side forces, and (10) pitching and yawing moments. The harmonic components of (1), (2), (3), (6), (7), (8), (9), and (10) are also printed.

EXPERIMENTAL PROGRAM

OBJECTIVE

The expressed purpose of the experimental phase of this program was to obtain a consistent set of performance (mean thrust, torque) and stress data with a high degree of accuracy. These data could then be used to correlate with those of the theoretical phase of this program. Of the available existing data examined, none of the performance quantities were known to be within the desired accuracy. Furthermore, no set of stress data taken in conjunction with performance data existed.

At the time, the most economical means for obtaining such a set of data seemed to lie with the tests of the 0.6-scale model of the XC-142; the model had four sets of three-bladed propellers. The tests were being conducted by National Aeronautics and Space Administration - Ames in the 40-ft x 80-ft wind tunnel for the purpose of obtaining individual propeller shaft loads, as well as ship total loads, for various flight configurations. It was arranged that CAL, under USAAVLABS sponsorship, would be allowed to instrument one blade of each of two prop sets in order that blade strains might be measured during the tests, along with the propeller shaft loads being obtained by NASA. Thus a consistent set of strain and thrust and torque data could be obtained, recognizing that these data pertain only for a specific configuration having such interference effects as wing, wing tip, nacelle, wing flaps and slats, propeller-propeller overlap, and fuselage. Some of these effects could have been evaluated by performing tests with selected prop sets running. For instance, prop-prop interference could be eliminated simply by running tests with only one prop operative. However, due to test schedule pressures, no such configurations were tested.

MODEL, APPARATUS, AND PROCEDURE

NASA was responsible for all aspects of the tests except gathering of the strain data, which was CAL's responsibility. [illegible] Ames was to collect measured values of prop thrust, torque, normal force, and pitching moment by using a rotating balance system developed and tested by NASA. Since both the performance and strain data were to be collected in a rotating frame of reference, a set of slip-rings was required. Unfortunately, the number of rings available was insufficient to handle both the strain and performance data simultaneously, and a switching arrangement to be mounted on the rotating hub had to be devised. So long as the flight conditions, i. e., free-stream velocity, prop rotor speed, etc., were maintained constant for sufficient time, no difficulty was anticipated with this sequenced recording.

Relays to provide the required switching capabilities were tested to insure their operability in the high g-field to which they would be subjected. These tests also provided the assurance that the relays would not interfere with the electrical signals being transmitted through them by excessive attenuation or by contributing noticeable amounts of noise from sources such as relay point chatter.

One blade on each of two prop sets was instrumented with two rosette strain gages. One rosette was located at 2.67 feet from the centerline of rotation, and the other at 3.67 feet from the centerline. Both were at the 50% chord. These locations were selected because experimental data reported in Reference 2 indicated that the maximum steady bending and first vibratory bending mode strains would be maximum at 50% span ($\approx$ 2.67 ft) and that the first vibratory torsion mode strains would be maximum at 75% span ($\approx$ 3.67 ft). Since the blades of Reference 2 were similar to the blades on the 0.6-scale model of the XC-142, these stations were selected.

Signal wires were bonded to the blade trailing edge and terminated at a junction plate which held the dummy resistors required for the gage bridges and the relays required for switching. From the junction plate, signal wires were attached directly to the platter-type slipring, from whence they entered the wind-tunnel electrical system. On the output end of the wind-tunnel system, parallel recording units were provided which allowed both CAL and Ames to record the rotating balance signals. Only CAL could record the strain signals.

The test procedure for those points of mutual interest to CAL and Ames was as follows:

(1) Wind-tunnel variables (i.e., tunnel density, velocity, total force measurements, etc.) were recorded by Ames.
(2) Ames recorded the signals from the rotating balance.
(3) The signals from the rotating balance were then switched to and recorded by the CAL units (Ames units being shunted out).
(4) The relays were then actuated. This allowed one set of strain data to be recorded.
(5) The relays were reset to a new position, and then the second set of strain data was recorded.
(6) Control was then returned to Ames.

Just prior to and immediately after a sequence of runs, a resistance calibration check was made. This run consisted of switching a known resistance in and out of the circuit and recording the oscillograph trace deflection. From pretest calibrations, the load per inch of trace deflection could then be determined.

Also recorded at the beginning and end of each run were the first and last turnovers of the propeller with the wind off.

A description of the model tested is given in detail in Reference 4.

CONFIGURATIONS TESTED

The prime variables of interest during these tests were wing angle (α_W) with respect to the fuselage centerline, fuselage angle (α_F) with respect to the free stream, prop speed (Ω), tunnel velocity (V_f), and prop thrust and torque. Also of interest were the effects of yaw angle (α_Y), flap angle (α_P), and leading-edge slats.

A configuration run was determined by the wing angle. For a given run, subcases were determined by various combinations of the above variables. A configuration was referred to as "clean" if there were no leading-edge slats and $\alpha_P = 0$. The configuration was "dirty" if both leading-edge slats and flap angle were employed.

The configurations for which both strain and performance data were collected are:

Clean Configurations ($\alpha_Y \equiv 0$, $\alpha_P \equiv 0$) (i.e., without flaps and slats)

$\alpha_W = 40^\circ$

$\alpha_F = 10^\circ$
$\alpha_F = 0^\circ$
$\alpha_F = -10^\circ$
} $V_f = 39.8$ FT/SEC ; $\Omega \approx 1264$ r.p.m.

$\alpha_W = 60^\circ$

$\alpha_F = 0^\circ$; $V_f = 33.7$ FT/SEC ; $\Omega \approx 1380$ r.p.m.

$\alpha_W = 90^\circ$

$\alpha_F = 0^\circ$; $V_f = 0$; $\Omega \approx 1380$ r.p.m.

Dirty Configurations ($\alpha_T = 0$, $\alpha_p = 60^\circ$) (i.e., with flaps and slats)

$\alpha_W = 40^\circ$

$\left.\begin{array}{l} \alpha_F = 10^\circ \\ \alpha_F = 0^\circ \\ \alpha_F = -10^\circ \end{array}\right\}$ $V_f = 39.8$ ft/sec; $\Omega \approx 1264$ r.p.m.

DISCUSSION OF RESULTS

THEORETICAL RESULTS

The digital program discussed on page 22 was used to obtain theoretical results for seven flight cases of the 0.6-scale model of the XC-142. The mass-elastic data for the model (i.e., the distributions of mass, stiffness, inertia, area, etc.) were obtained from the Hamilton Standard Company, which built the model blades. Also received from Hamilton Standard Company and incorporated into the program were two-dimensional airfoil section characteristics for the airfoil sections used in the model blades.

Five of the cases analyzed correspond to the clean configurations for which experimental data were collected (see section titled Configurations Tested, page 28.) The $\tau = 40^{\circ}$ case was computed a second time to show the effect of changing the wing load with all other parameters held fixed. The $\tau = 90^{\circ}$ (hovering) was computed twice to indicate the effect of ground proximity on the 0.6-scale model of the XC-142. The time histories of thrust, torque, normal and side forces, pitching, and yawing moments are presented for each case in Figures 6 through 10.

Note that, in Figures 6 through 10, the mean values of the thrust, torque, normal force, etc., are printed at the top of each graph and the oscillatory components are plotted about zero mean.

The dominant frequency contents of the oscillatory values of the thrust and torque for all cases except $\tau = 90^{\circ}$ are 3P (i.e., a frequency equal to 3 times the prop speed), 6P, 9P, etc. The peak-to-peak magnitude of the 3P component of the thrust is approximately 5% of the mean thrust; the magnitude of the 6P component is approximately 10% of the 3P component. The magnitudes of the 1P, 2P, 4P, 5P, 7P, etc., harmonics are of the order of 1×10^{-6} lb. Since the only harmonics of the performance quantities which can

be transmitted to the shaft during steady-state flight must be integer multiples of the number of blades, the magnitudes of these latter harmonic components become a measure of the accuracy of the numerical method employed. Torque, normal and side forces, and pitching and yawing moments exhibit the same characteristics as the thrust of dominant 3P, 6P, and 9P harmonics, with all other harmonics negligibly small; however, for the normal and side forces, and pitching and yawing moments, the phasings of the significant harmonics are such as to cause their time (ψ) histories to appear less sinusoidal. Note also the relatively large mean and oscillatory pitching and yawing moments predicted in all cases.

A comparison of Figures 7 and 8 indicates the effect of changing the wing load. With all other parameters held fixed, the strength of the wing bound vortex (Γ_W) was decreased from 400 ft^2/sec (Figure 7; this case corresponds to the experimental configuration) to 298 ft^2/sec (Figure 8), a reduction of 25%. Almost no change in the mean thrust or torque was noted. The peak-to-peak amplitudes of the time-dependent portions of the thrust and torque were reduced by approximately 25%. The mean values of the remaining performance quantities (side force, pitching moment, etc.) were reduced by approximately 11%, while the oscillatory portions of these quantities were reduced by approximately 21%. The apparent one-to-one correspondence between Γ_W and the peak-to-peak amplitude of the performance quantities is believed to be coincidental.

Two hovering ($\tau = 90^\circ$, $V_f = 0$) cases were computed. One case was intended to simulate the model sitting on the ground; hence, the prop plane was approximately one rotor diameter above the ground; the other case was computed for the same parameters except with the prop plane well out of ground effect. It was found that the effect of the ground was slightly detrimental. The table below presents the thrust and torque values for the two cases.

	Thrust (lb)	Torque (ft-lb)
Hovering In-Ground Effect	1176	639
Hovering Out-of-Ground Effect	1213	642

While the torque remained essentially constant, the thrust decreased by approximately 3%, due to the effect of ground. Examination of the RVM in the two cases revealed that for the near wake (i.e., within, say, a quarter prop radius) the shape and spacing of the wake were essentially the same. Farther down the wake, however, the shape and spacing were no longer the same. At approximately one prop radius, the wake boundary for the in-ground effect case increased in diameter, while that for the out-of-ground effect case continued to contract. It is believed that for the case in hand the small increase in thrust and torque obtained as the height above ground increased was due to the fact that the far wake had contracted more. That the increase was small is attributed to the fact that the near wakes are almost identical in the two cases.*

* Note that the effect of the ground can be either beneficial or detrimental, depending upon (1) the degree of wake distortion, (2) the wake spacing, and (3) the load distribution on the blade. For example, if the blade load distribution is such that a major portion of the load is carried on the most outboard blade sections (say from 90% span out), then contraction of the wake will result in a decrease in load. That is provided that the wake contraction does not move inboard of the 90% span. If the contracted wake moves inboard of the 90% span, the wake effect is such as to increase the load.
An additional contributing factor which was not included in the above analysis is the influence of the ground image system on the induced velocity at the rotor plane.

Presented in Figure 11 are the spanwise variations of the harmonics (zeroth to the fourth only) of the theoretically computed longitudinal stress for $\tau = 50^{\circ}$. The plot is representative of the stress distributions computed for all the cases.

EXPERIMENTAL RESULTS

Considerable difficulty was encountered in trying to reduce the experimental data. Even before the wind-tunnel program was completed, peculiarities were noted in the data from nacelle number 1 (the outboard nacelle on the pilot's left). It was subsequently found that an intermittent short had developed in one of the gages of the balance system. Since all the gages on nacelle number 1 were powered from a common supply, it was felt that the signals of all gages, both from the balance system and the strain gages, would be affected by the intermittent short. Hence, none of the data collected on nacelle 1 were reduced.

The raw thrust and torque and strain data collected from nacelle number 2 (inboard nacelle on pilot's left) were examined. It was noted that these were not periodic over the time interval during which records were taken. This nonperiodicity was much more pronounced on the strain records than on the thrust and torque records. It was determined that the nonperiodic loadings were due to the fact that the two adjacent propellers were not synchronized; i.e., they did not have the same prop speed. Thus, the propellers experienced a slightly different wake geometry for every revolution. Since the difference in speed was small, the effect of the wake changes was not as noticeable in the thrust and torque data as in the strain data, which showed variations from one revolution to the next in some cases.

Harmonic analysis of the thrust and torque data revealed relatively large 1P and 2P frequency components (on the order of 10% of the mean values for some cases). These components could not have existed if the thrust and torque had been periodic.

Because of nonperiodicity of the loads, the sequencing procedure (see section titled Model, Apparatus, and Procedure, page 26) used in collecting the test data, in particular the strains, becomes highly questionable. Reduction of some of the strain data was performed based upon certain restrictive assumptions as discussed in Appendix VIII, page 97. Since the thrust and torque exhibited the least effect of the nonperiodicity, it was reasoned that, at least, the means of these quantities could be obtained from the data.

Reduction of the thrust and torque data posed another problem in addition to the ones concerned with nonperiodicity. Certain anomalies were noted in the rotating balance data collected during the test which gave rise to questions concerning the accuracy of the calibration of the balance unit and, in particular, to the amount of crosstalk between the various components.

The anomalies were observed in the thrust and torque data taken during the very slow rotation of the propellers prior to bringing the wind tunnel up to speed. Because of the low prop r. p. m., it was expected that the inertia and aerodynamic loads would be negligibly small. Since the weight components had been electrically nulled at zero r. p. m., no changes from the zero r. p. m. positions in the thrust and torque signals were expected at these low r. p. m.'s. However, a mean shift, plus a 1P oscillatory signal in thrust and torque, was observed. The origin of this signal is unknown, as is its behavior with the variables of Ω, τ, etc.

Because of the errors associated with (1) data recording and reduction, (2) the nonperiodicity of the loads, and (3) the above noted anomalies in the experimental thrust and torque, the data presented in this report for the thrust and torque are believed to be good only to within $\pm$ 10%.

Presented in Figures 12 through 17 are the mean and oscillatory values of the harmonically analyzed experimental thrust and torque.

The dominant nonzero harmonic of the thrust for all cases including $\tau = 90°$ is the 3rd. It has a peak-to-peak value of approximately 10% of the mean. Note the large 1P frequency component in most of the configurations. The oscillatory portion of the torque contains large components at frequencies from 1P through 6P in almost all cases.

A comparison of Figures 14 and 15 shows the effects of adding slats and 60° of wing flaps. Figure 14 is the clean configuration, i. e., without slats and flaps, while Figure 15 is the dirty configuration, with slats and flaps. The mean and oscillatory components of the thrust show almost no effect due to slats and flaps. However, the mean torque was reduced by approximately 10% with the addition of flaps and slats, while the dominant frequency component shifted from 3P to 6P.

Figure 17 presents the thrust and torque for the hovering case. Note the relatively large oscillatory components of thrust and torque. The peak-to-peak oscillatory thrust is approximately 10% of the mean thrust. The peak-to-peak oscillatory torque is approximately 7% of the mean torque. These oscillatory loads are believed to be due to the interference effects of prop-prop overlap, the wing, nacelle, and fuselage.

Because of the nature of the rotating balance and the fact that the prop loads were not periodic, the total normal force could be measured only at $\psi = 0$ and 180°, while the total side force could be measured only at $\psi = 90^{\circ}$ and 270°. Hence, no information concerning the nature of the mean or oscillatory normal forces or side forces could be obtained from the measured data. The same comments apply to the pitching and yawing moments.

COMPARISON OF THE EXPERIMENTAL AND THEORETICAL RESULTS

Comparison of the mean theoretical and experimental thrust and torque are presented in Figure 18. The experimental data values are shown with a band indicating the estimated error of $\pm$ 10%.

In the range $30^{\circ} \leq \tau \leq 50^{\circ}$, the theoretical thrust values lie within the estimated accuracy of the experimental thrust data. At $\tau = 60^{\circ}$ and $\tau = 90^{\circ}$, the theoretical thrust is slightly greater than the experimental thrust.

The theoretically predicted torque was greater than the experimentally measured torque for all configurations tested.

No comparison between the oscillatory loads could be made because of the nonperiodicity of the experimental thrust and torque.

Since the experimental data are not sufficiently accurate and include interference effects (prop-prop overlap and fuselage) not included in the present mathematical model, it was not possible to make sufficient comparisons for a definitive evaluation of the theoretical method developed.

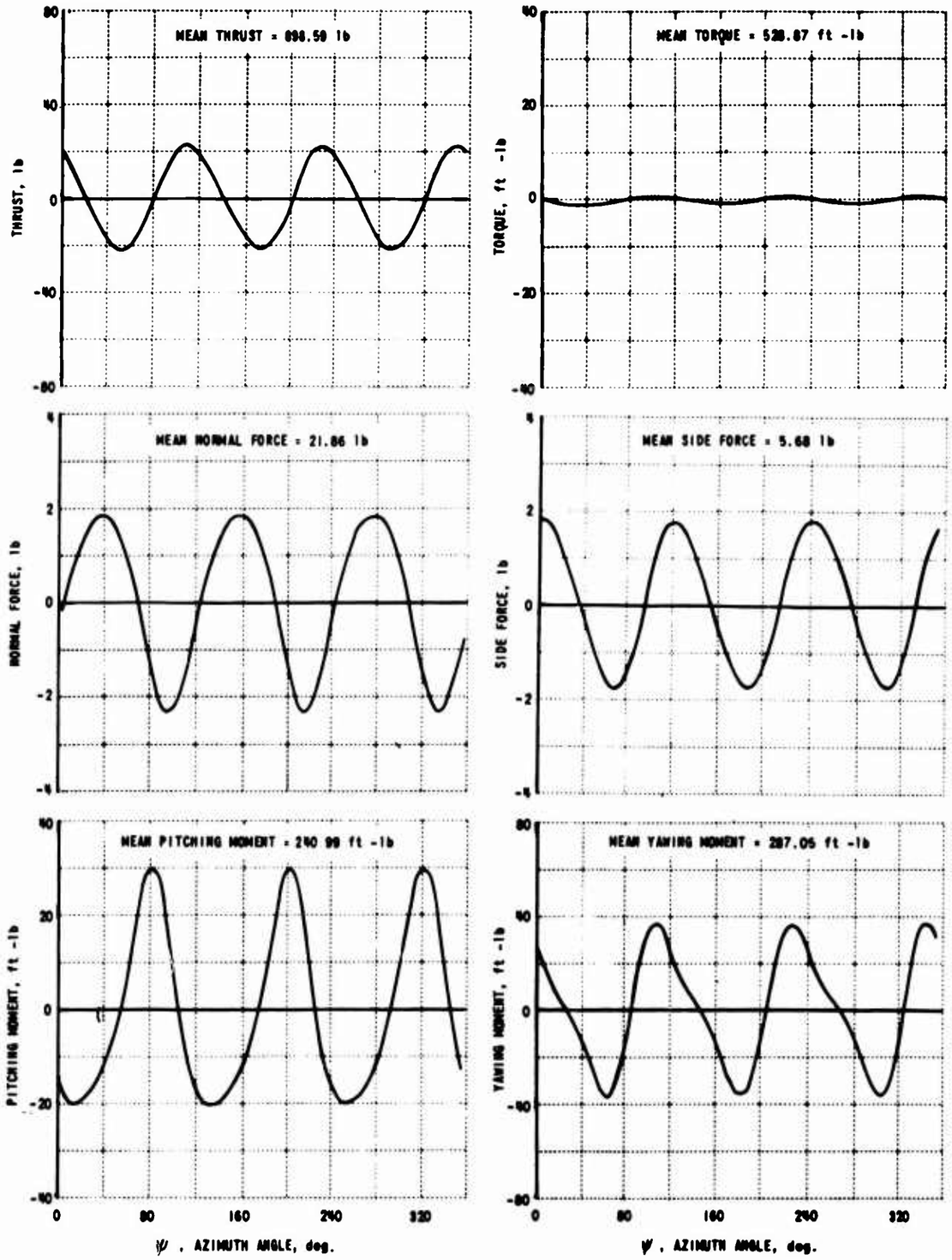

Figure 6. MEAN AND INSTANTANEOUS VALUES OF THEORETICAL PERFORMANCE FOR V_f = 39.8 ft /sec ; τ = 30°; Ω = 1264 r.p.m.; Γ_w = 310 ft ^{2}/sec

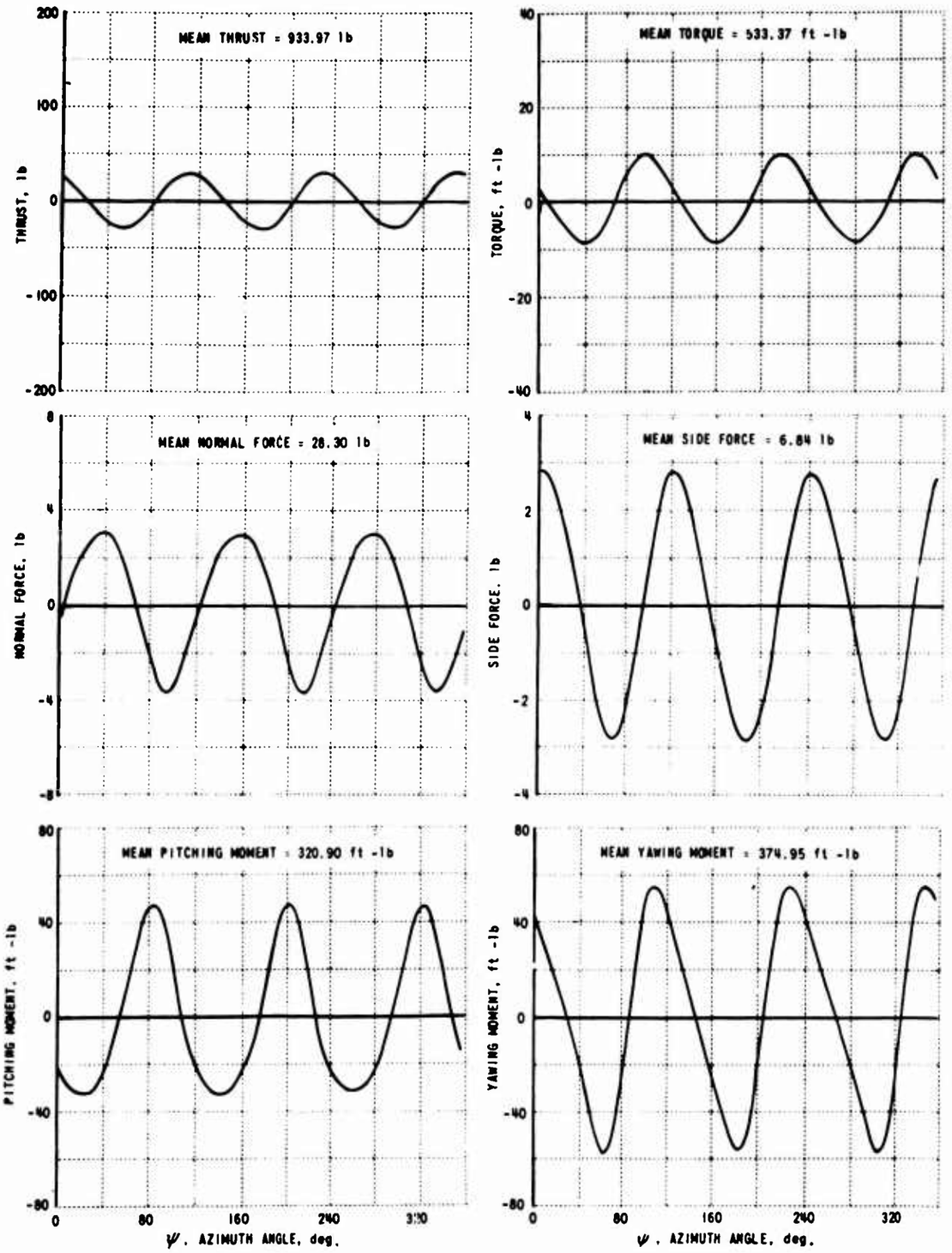

Figure 7. MEAN AND INSTANTANEOUS VALUES OF THEORETICAL PERFORMANCE FOR V_f = 39.8 ft /sec ; τ = 40°; Ω = 1264 r.p.m.; Γ_w = 400 ft ^{2}/sec

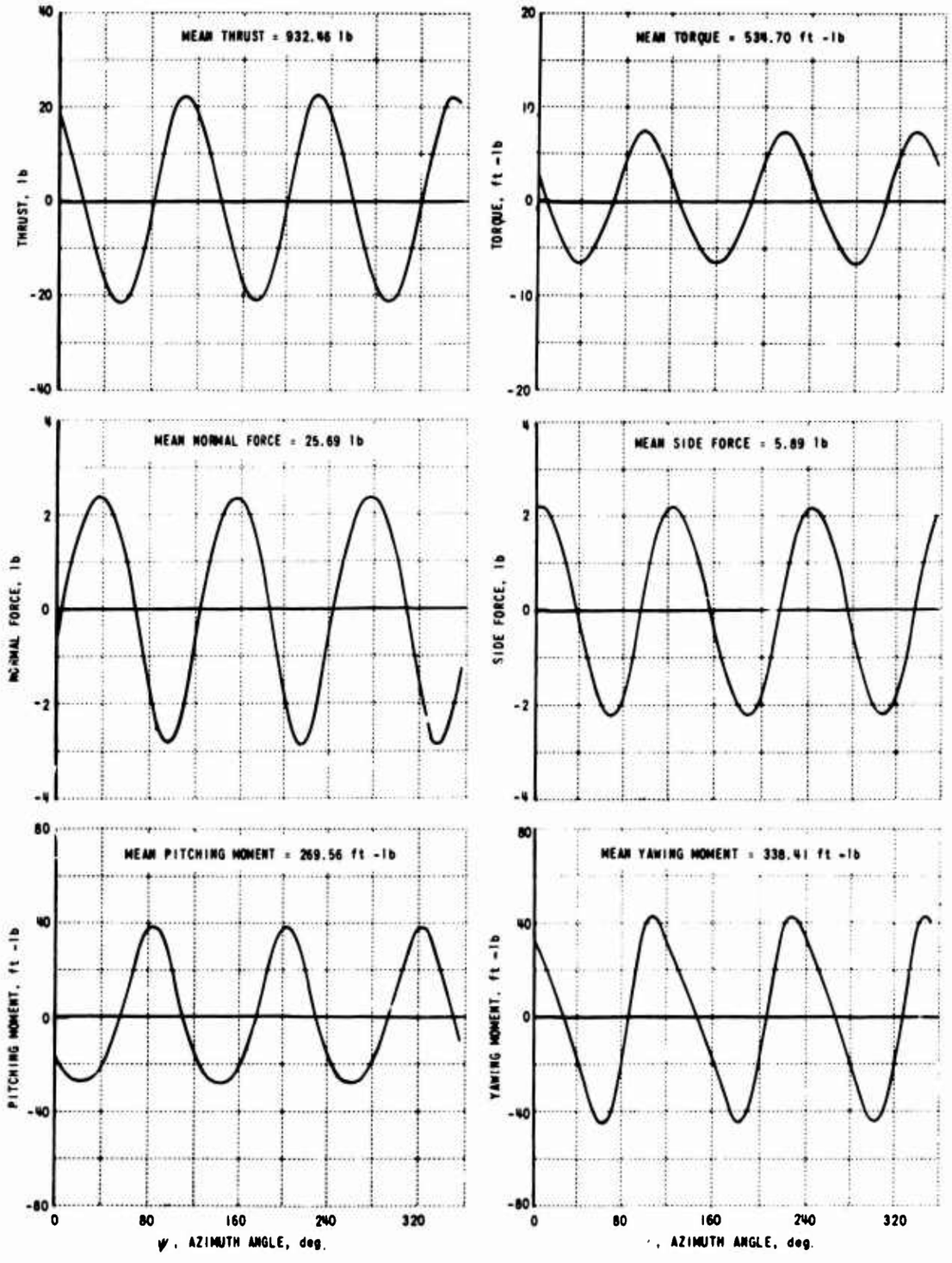

Figure 8. MEAN AND INSTANTANEOUS VALUES OF THEORETICAL PERFORMANCE FOR V_f = 39.8 ft /sec ; τ = 40°; Ω = 126 r.p.m.; Γ_w = 298 ft ^{2}/sec

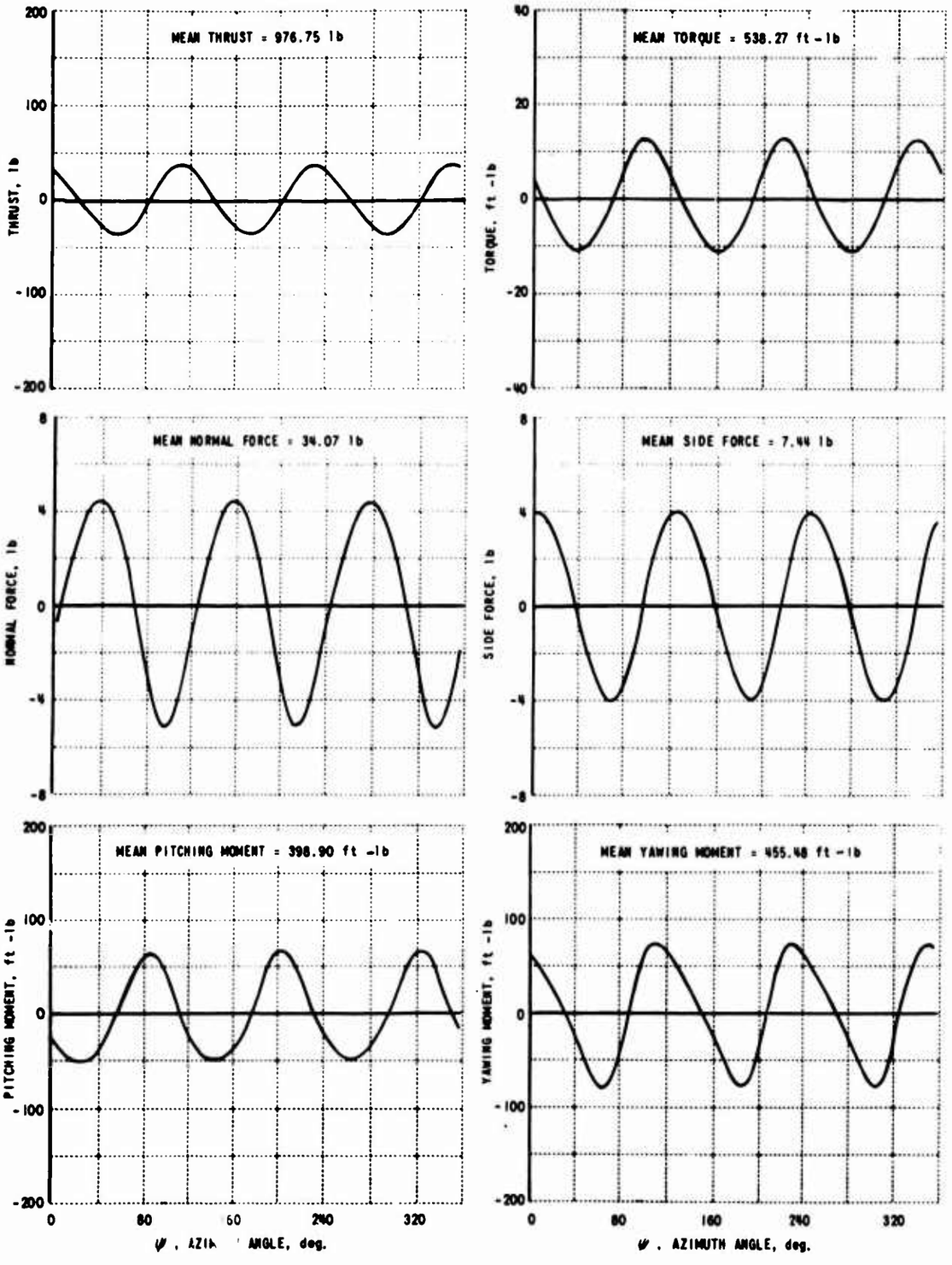

Figure 9. MEAN AND INSTANTANEOUS VALUES OF THEORETICAL PERFORMANCE FOR V_f = 39.8 ft /sec ; τ = 50°; Ω = 1264 r.p.m.; Γ_w = 479 ft ^{2}/sec

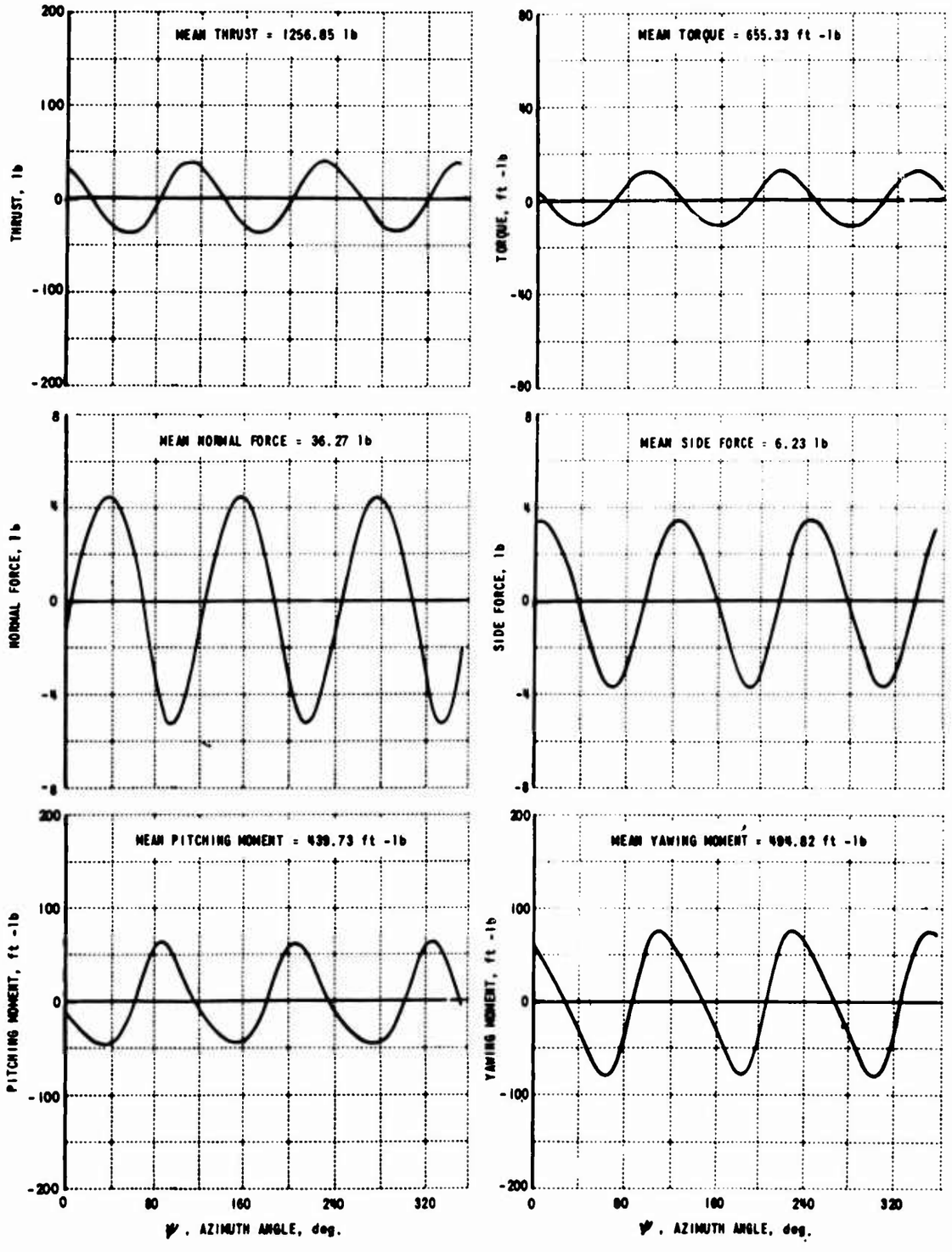

Figure 10. MEAN AND INSTANTANEOUS VALUES OF THEORETICAL PERFORMANCE FOR V_f = 33.7 ft /sec ; τ = 60°; Ω = 1380 r.p.m.; Γ_w = 457 ft ^{2}/sec

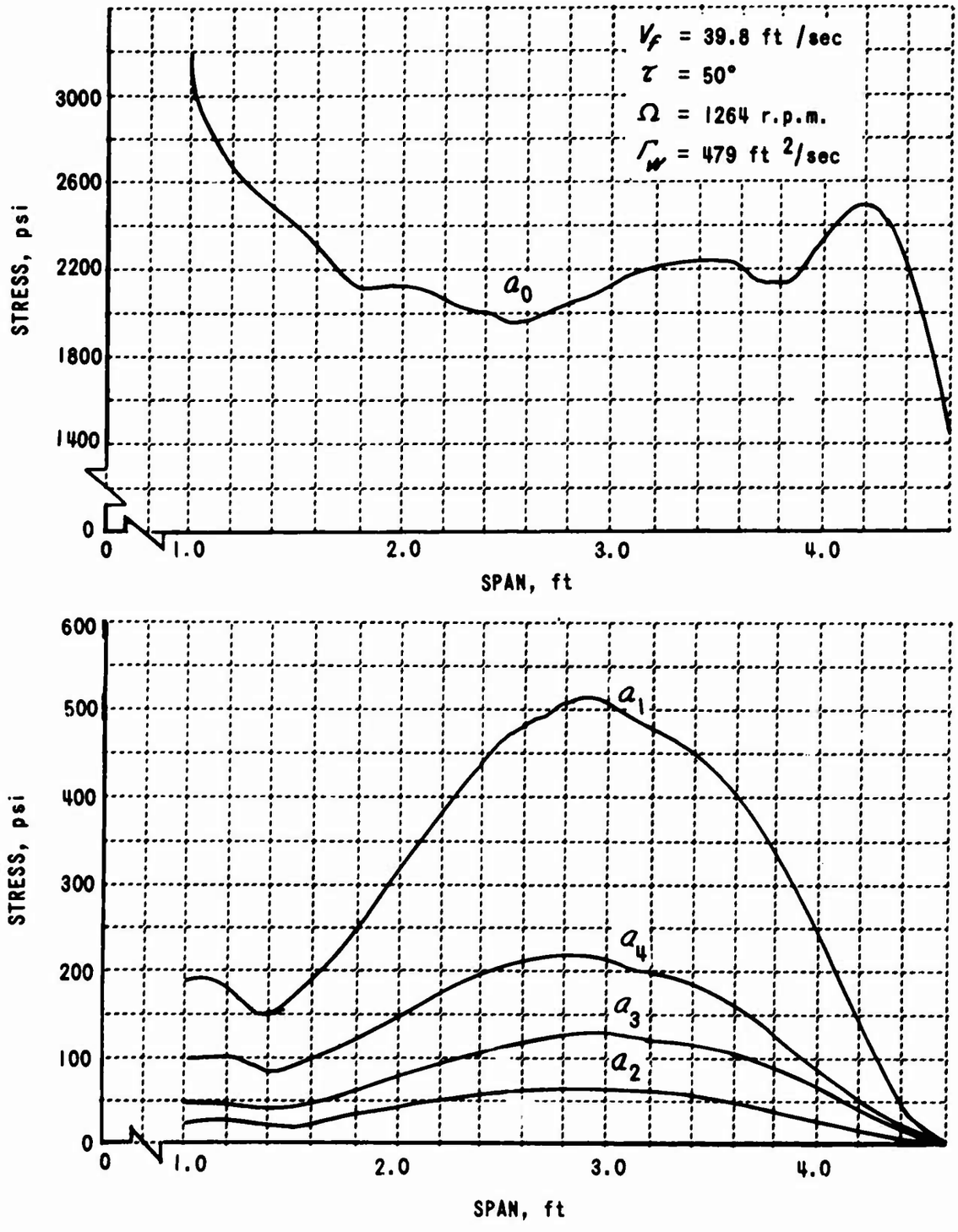

Figure 11. THEORETICAL HARMONICS OF LONGITUDINAL STRESS VS. RADIAL POSITION FOR τ = 50°

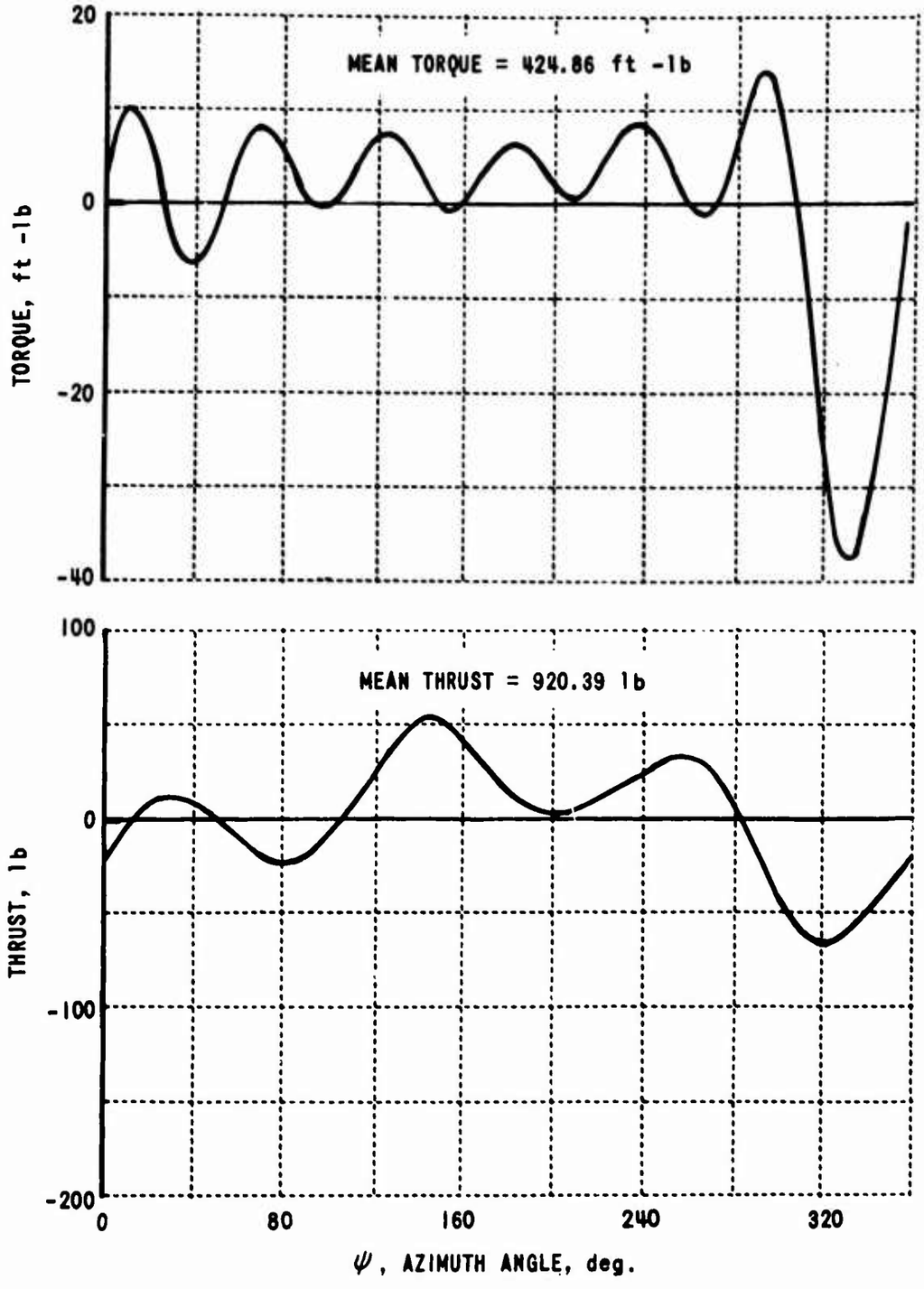

Figure 12. MEAN AND INSTANTANEOUS VALUES OF EXPERIMENTAL THRUST AND TORQUE DATA FOR V_f = 39.8 ft /sec ; τ = 30°; Ω = 1264 r.p.m.

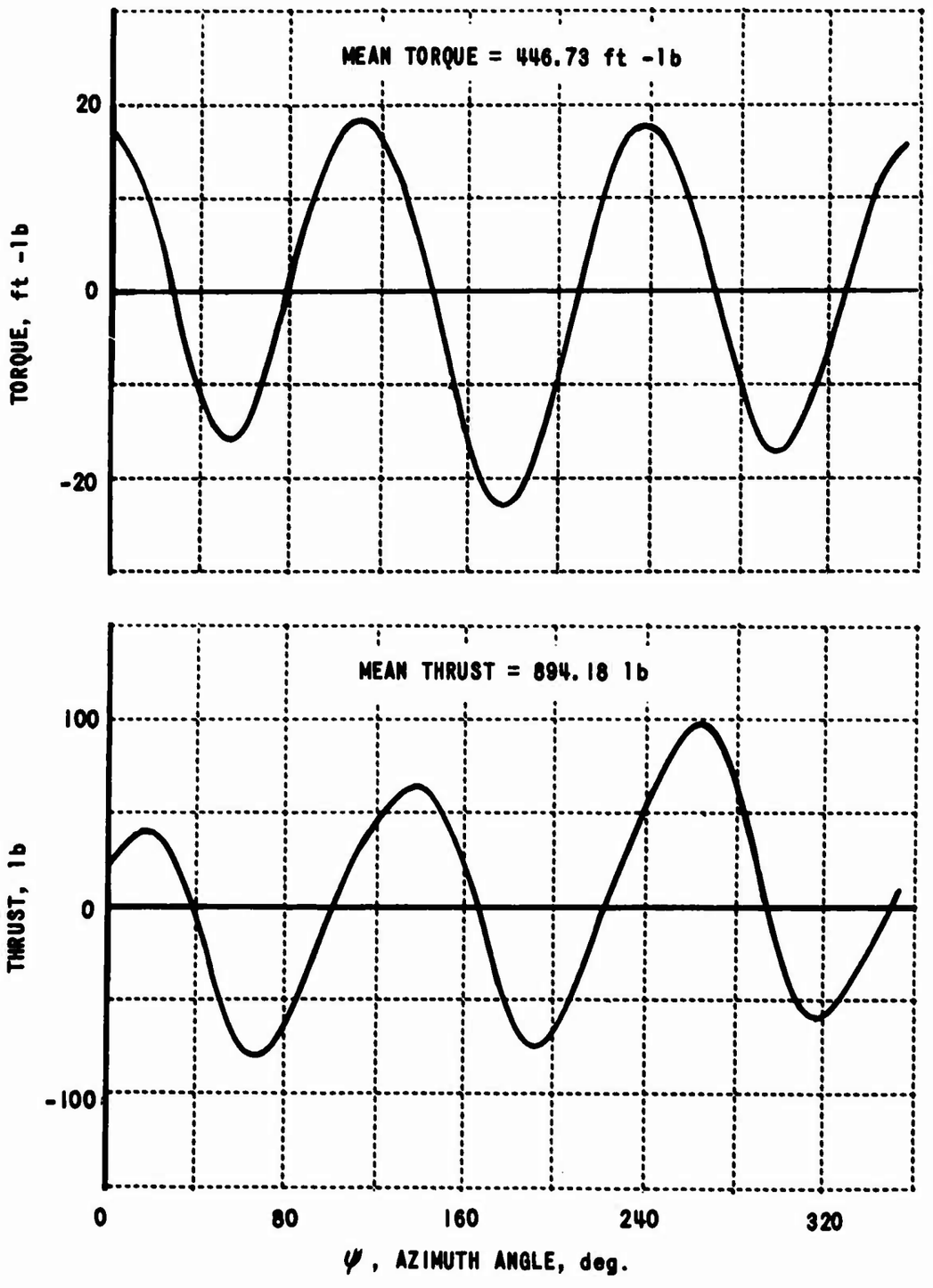

Figure 13. MEAN AND INSTANTANEOUS VALUES OF EXPERIMENTAL THRUST AND TORQUE DATA FOR V_f = 39.8 ft /sec ; τ = 40°; Ω = 1264 r.p.m.

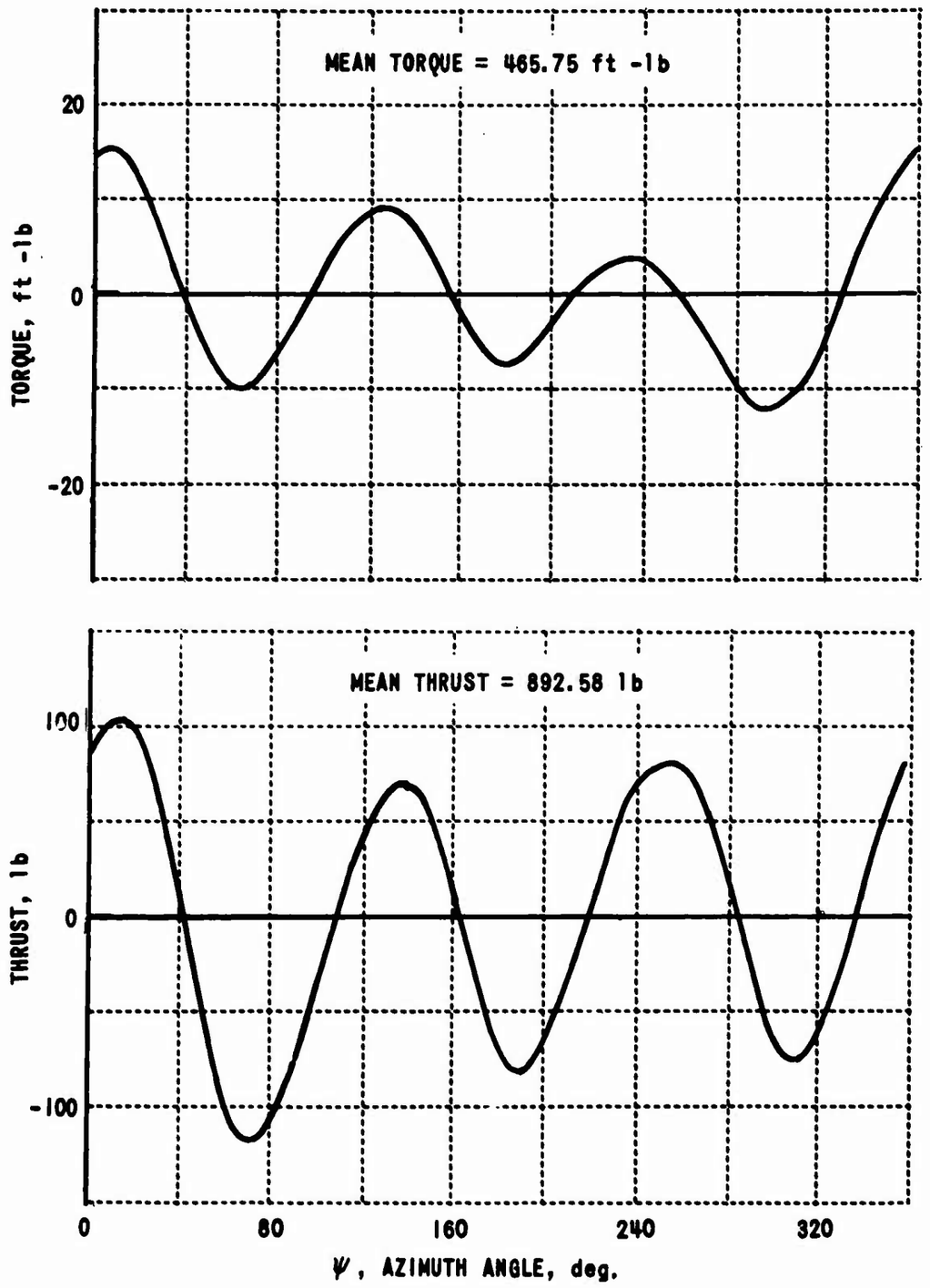

Figure 14. MEAN AND INSTANTANEOUS VALUES OF EXPERIMENTAL THRUST AND TORQUE DATA FOR V_f = 39.8 ft /sec ; τ = 50°; Ω = 1264 r.p.m.; WITHOUT FLAPS AND SLATS

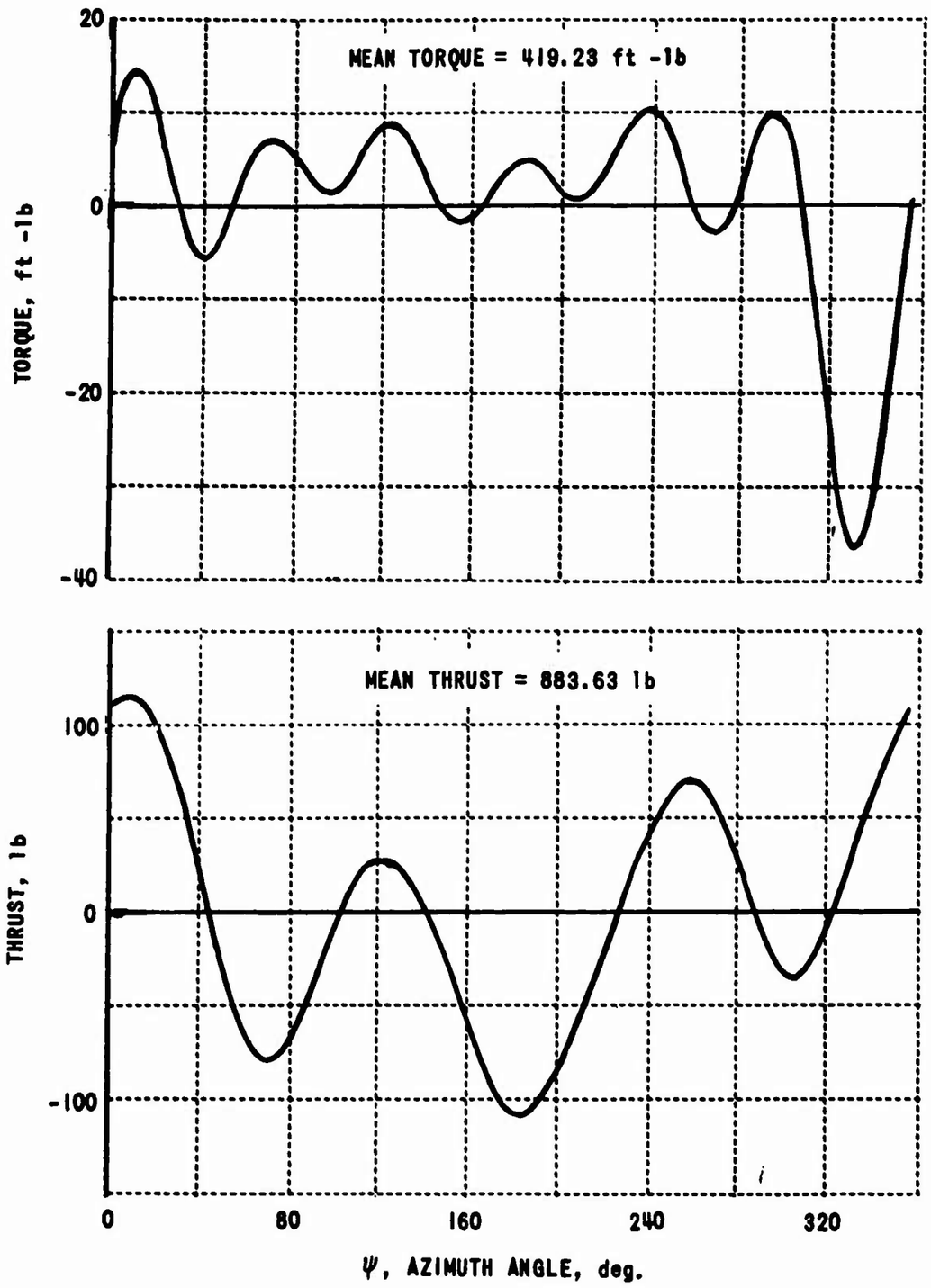

Figure 15. MEAN AND INSTANTANEOUS VALUES OF EXPERIMENTAL THRUST AND TORQUE DATA FOR V_f = 39.8 ft /sec ; τ = 50°; Ω = 1264 r.p.m.; WITH FLAPS AND SLATS

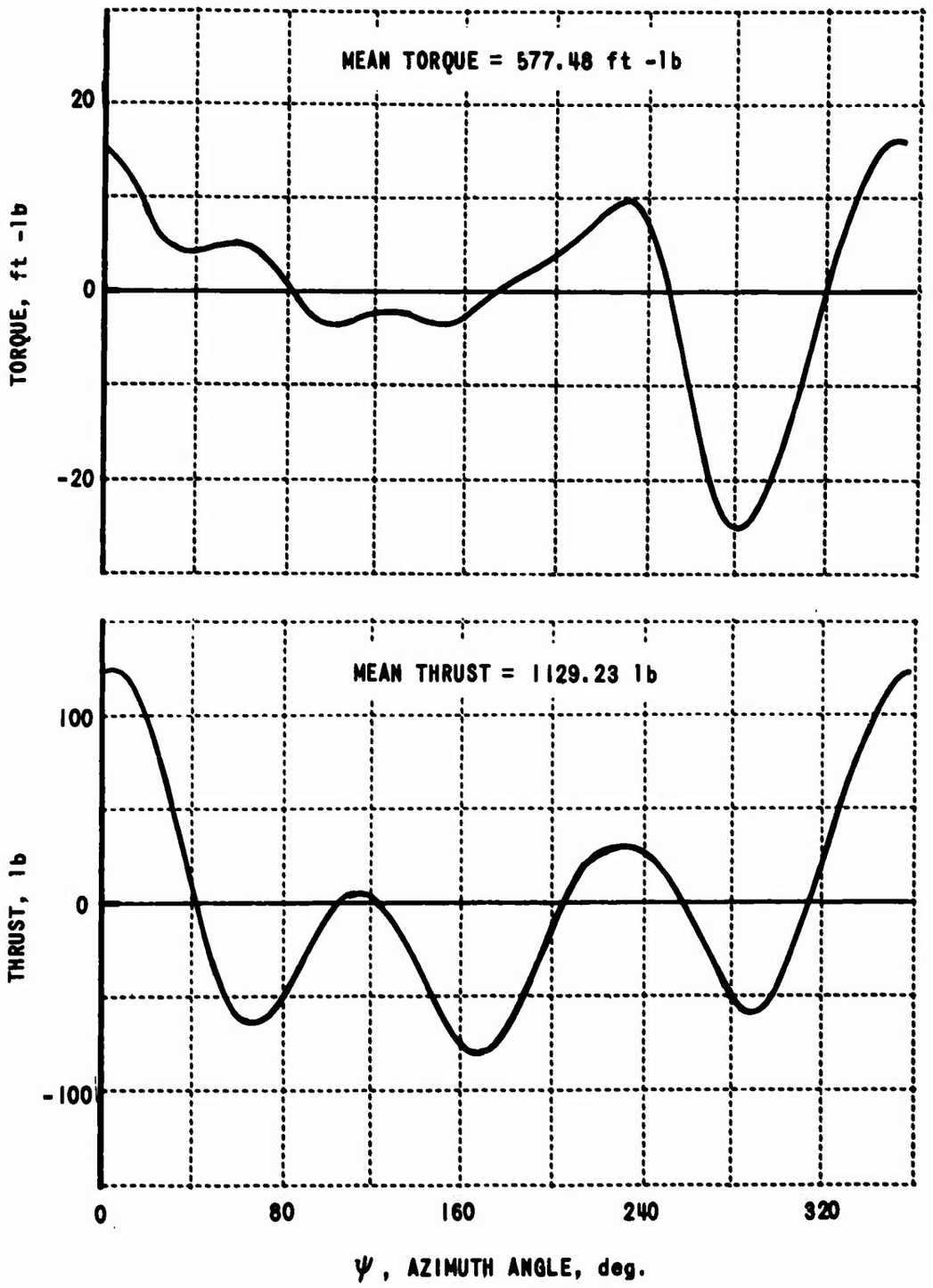

Figure 16. MEAN AND INSTANTANEOUS VALUES OF EXPERIMENTAL THRUST AND TORQUE DATA FOR V_f = 33.7 ft /sec ; τ = 60°; Ω = 1380 r.p.m.

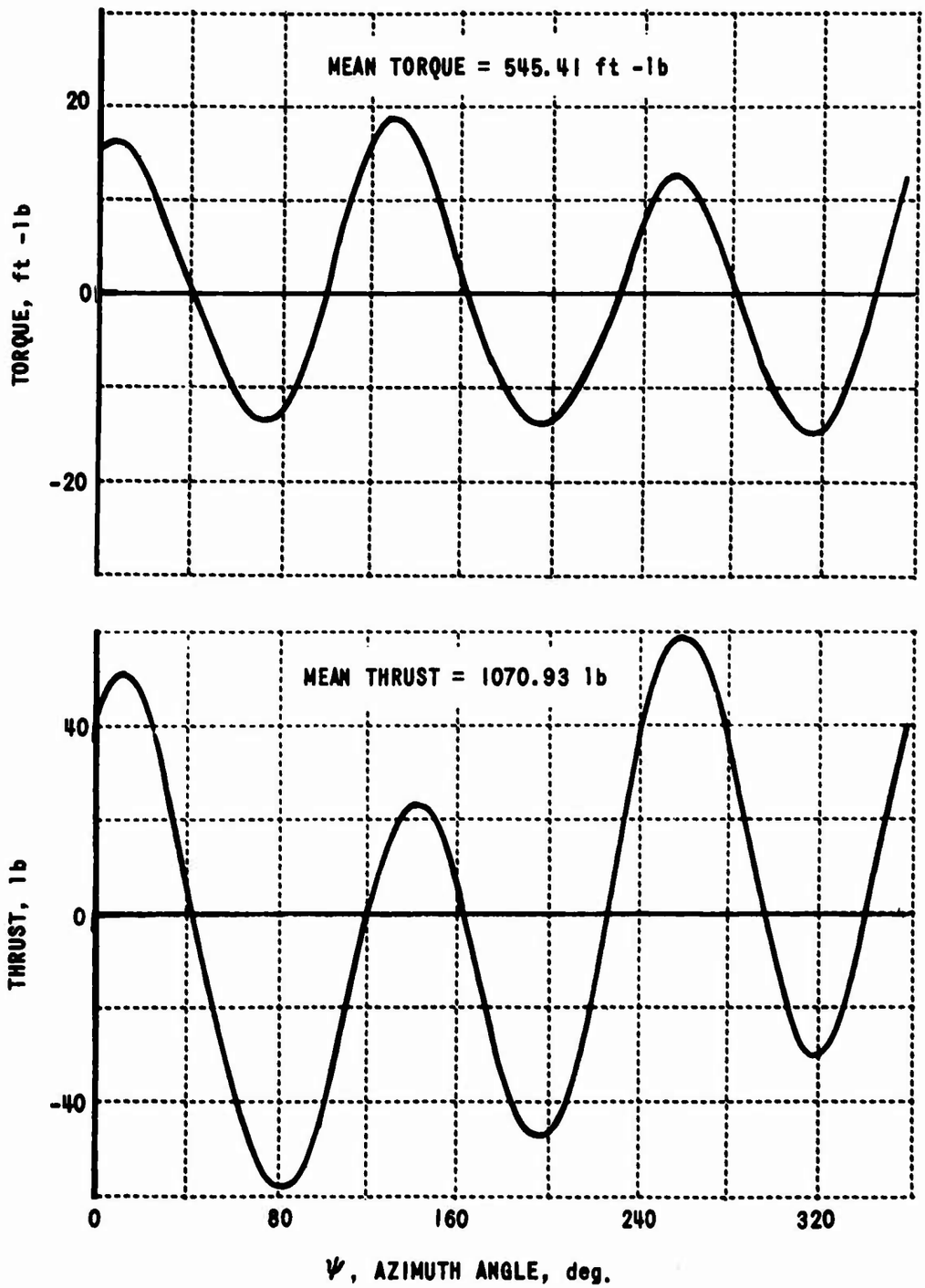

Figure 17. MEAN AND INSTANTANEOUS VALUES OF EXPERIMENTAL THRUST AND TORQUE DATA FOR V_f = 0 ft /sec ; τ = 90°; Ω = 1380 r.p.m.

THEORETICAL	EXPERIMENTAL	V_f ft /sec	Ω r.p.m.	Γ_w ft ^{2}/sec
○	○	39.8	1264	310
△	△	39.8	1264	400
⬭	⬭	39.8	1264	479
□	□	33.7	1380	457
◇	◇	0	1380	0

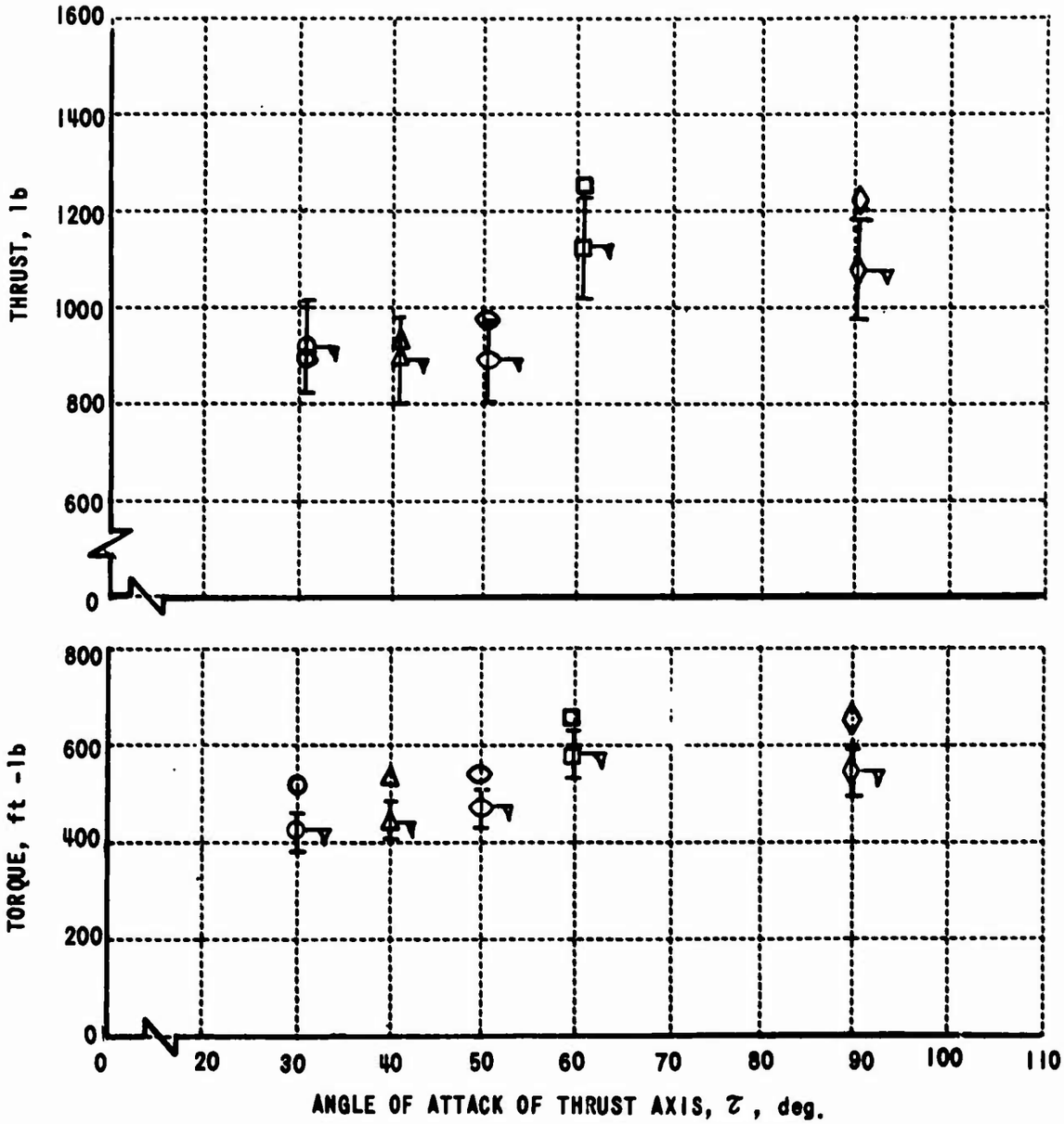

Figure 18. COMPARISON OF MEAN THEORETICAL AND EXPERIMENTAL THRUST AND TORQUE VS. ANGLE OF ATTACK OF THRUST AXIS

CONCLUSIONS

Based on the results obtained in this study, the following conclusions were drawn.

It has been shown during the course of this study that the approach employed to define and formulate the aeroelastic problem associated with VTOL-type propellers operating in all flight regimes from hovering (in- and out-of-ground effect) through transition and into axial flight is a feasible one. Furthermore, the digital program developed to implement solution of the resultant aeroelastic equations converges to a unique solution in a reasonable length of time (approximately 0.75 hour on the IBM 7044).

The experimental thrust and torque data collected during the NASA-Ames wind-tunnel test program are believed to be good only to ± 10%, which is not considered sufficiently accurate to provide the desired evaluation of the model developed herein. Although it was possible to collect the thrust and torque data, certain other needed information, such as the mean and oscillatory normal and side forces as well as pitching and yawing moments, was not obtained because the propeller load measurement system could not properly account for the nonperiodic character of the data. As a result, the rotating balance unit employed in these tests yielded data which could not be converted into the desired inplane forces and moments. Furthermore, it was concluded that the measured blade strains, which were also nonperiodic, could not be converted to stresses without certain assumptions. These assumptions were highly questionable in light of the nonperiodicity of the strain measurements; hence, the stresses obtained were questionable.

RECOMMENDATIONS

CAL is currently working on a modification to the contract under which this report was written. The purpose of this modification is to obtain accurate experimental thrust, torque, and blade strains and stresses on an isolated propeller (i.e., no interference effects from other props, wings, etc.). The data will be used to correlate with those of the theoretical approach developed herein. This effort is expected to satisfy the foremost recommendation, namely, that of obtaining accurate experimental data for an isolated propeller.

It is further recommended that (1) the computational program be employed to provide quantitative answers to the effects of wing, wake, forward velocity, and nacelle, (2) the present program be expanded to include the effects of prop-prop overlap and fuselage, and to investigate whether the lifting-line model of the blade and wing should be abandoned in favor of a model which accounts for a chordwise distribution of vorticity, and (3) theoretical and experimental programs be undertaken with the objective of improving the wake model.

REFERENCES

1. Brady, W.G., and Crimi, P., Representation of Propeller Wakes by Systems of Finite Core Vortices, Cornell Aeronautical Laboratory, Inc., Buffalo, New York, CAL Report No. BB-1665-S-2, February 1965.

2. Burquest, Marshall O., and Carpenter, James E., Cornell Aeronautical Laboratory, Inc., Structural and Vibrational Characteristics of WADC S-2 Model Propeller Blades, Wright Air Development Center, Dayton, Ohio, WADC TR 56-28, December 1955.

3. Chang, T.T., A Flutter Theory for a Flexible Helicopter Rotor Blade in Vertical Flight, Cornell Aeronautical Laboratory, Inc., Buffalo, New York, CAL Report No. SB-862-S-1, July 1954.

4. Deckert, W.H., Page, V. Robert, and Dickinson, Stanley O., Large-Scale Wind-Tunnel Tests of Descent Performance of an Airplane Model with a Tilt Wing and Differential Propeller Thrust, National Aeronautics and Space Administration, Moffett Field, California, NASA TN D-1857, October 1964.

5. DuWaldt, F.A., Gates, C.A., and Piziali, R.A., Cornell Aeronautical Laboratory, Inc., Investigation of the Flutter of a Model Helicopter Rotor Blade in Forward Flight, Wright Air Development Division, Dayton, Ohio, WADD TR 60-328, July 1960.

6. Hirsch, H., Kline, J., and Mertens, R., A Preliminary Design Study of Main Rotor Blades for a Variable Stiffness Flight Program, Cornell Aeronautical Laboratory, Inc., Buffalo, New York, CAL Report No. BB-427-S-2, September 1946.

7. Houboult, J.C., and Brooks, G.W., Differential Equations of Motion for Combined Flapwise Bending, Chordwise Bending, and Torsion of Twisted Nonuniform Rotor Blades, National Advisory Committee for Aeronautics, Langley Field, Virginia, NACA TN 3905, February 1957.

8. Kline, J., Structural Analysis of Fiberglass Main Rotor Blade for the R-5 Helicopter, Cornell Aeronautical Laboratory, Inc., Buffalo, New York, CAL Report No. BB-427-S-3, February 1947.

9. Loewy, R. G., A Two-Dimensional Approximation to the Unsteady Aerodynamics of Rotary Wings, Cornell Aeronautical Laboratory, Inc., Buffalo, New York, CAL Report No. 75, IAS Preprint No. 605, October 1955.

10. Martin, George B., Helicopter Main Rotor Blades, Cornell Aeronautical Laboratory, Inc., Buffalo, New York, CAL Report No. BB-427-S-1, May 2, 1946.

11. Piziali, R. A., and DuWaldt, F. A., Cornell Aeronautical Laboratory, Inc., A Method for Computing Rotary Wing Air Load Distributions in Forward Flight, U. S. Army Transportation Research Command,* Fort Eustis, Virginia, TCREC TR 62-44, November 1962.

12. Roark, R. J., Formulas for Stress and Strain, McGraw-Hill Book Company, Inc., New York and London, 1943.

13. Sokolnikoff, I. S., and Redheffer, R. M., Mathematics of Physics and Modern Engineering, McGraw-Hill Book Company, Inc., New York, 1958.

14. Yaggy, Paul F., and Rogallo, Vernon L., A Wind Tunnel Investigation of Three Propellers Through an Angle-of-Attack Range From 0^{o} to 85^{o}, National Aeronautics and Space Administration, Moffett Field, California, NASA TN D-318, May 1960.

*Now U. S. Army Aviation Material Laboratories

BLANK PAGE

APPENDIX I
POSITIONING THE WAKE

HIGH AXIAL AND TRANSITIONAL FORWARD VELOCITIES

For the case where the wake is carried back from the prop plane at high velocity in both the axial and in-plane direction, the wake is assumed to be a helix of constant pitch having no contraction. The interference effects of the wing and nacelle on the wake shape are neglected. The coordinates of any point in the wake can then be determined in a straightforward fashion. Consider a blade in some azimuthal position trailing a mesh of vorticity. Let KA denote the azimuthal position of the blade ($KA = 1, 2, \ldots \overline{NA}$), k denote radial position of a blade element ($k = 1, 2, \ldots \overline{NR}$), i denote the azimuthal position in the wake ($i = 1$ (at the blade), $2, \ldots \overline{NA} \times W$ where W is the number of revolution of wake), and j denote the radial position in the wake ($j = 1, 2, \ldots \overline{NR}$).

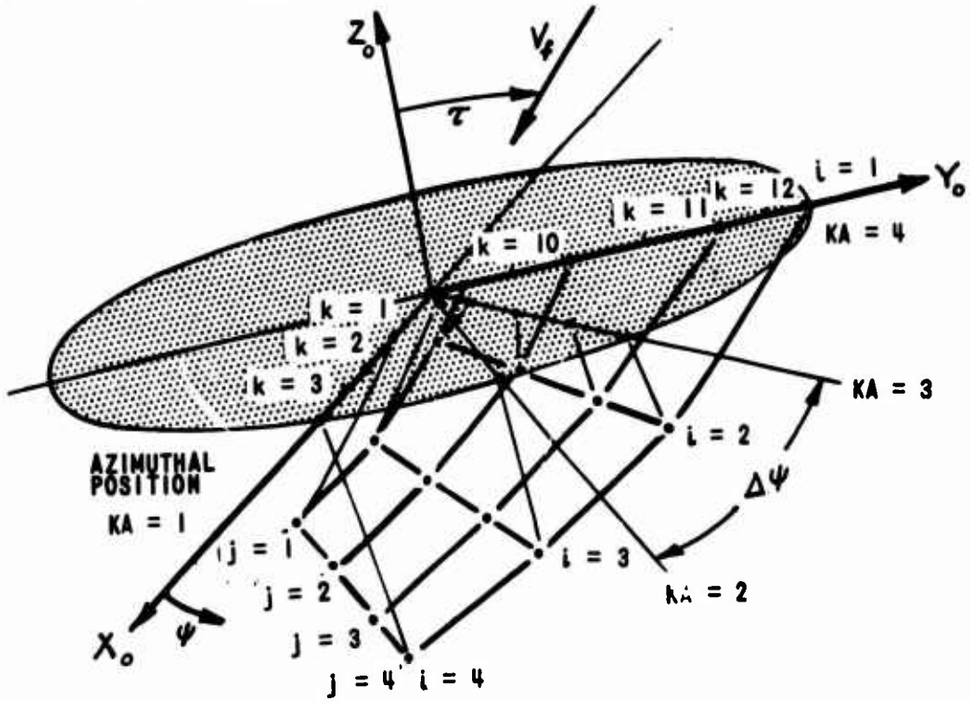

Figure 19. WAKE MODEL DETAILS

Note: At the end of each appendix is a list of symbols which applies to that appendix.

Then the coordinates of any point in the wake, for a given rotor position, are given by

$$\xi_{ij} = r_j \cos\left(\{KA - i\}\Delta\psi\right) + V_f \sin\tau\left(\frac{\Delta\psi}{\Omega}\right)(i-1) \tag{18}$$

$$\eta_{ij} = r_j \sin\left(\{KA - i\}\Delta\psi\right) \tag{19}$$

$$\zeta_{ij} = \left[\overline{W} - V_f \cos\tau\right]\left(\frac{\Delta\psi}{\Omega}\right)(i-1) \tag{20}$$

where

r_j = radial distance from centerline of rotation to j^{th} point in wake

$\overline{W}$ = inflow velocity (constant over disk).

HOVERING AND LOW TRANSITIONAL VELOCITIES

For the cases of hovering and low transitional velocities, the effects of wake contraction, axial and radial velocity variation, wing, nacelle, and forward velocity are accounted for. The effects of wing, nacelle, and forward velocity are treated as perturbations from the wake geometry obtained from the ring vortex model (RVM). The ring vortex model represents the rotor wake by a series of discrete ring vortices which are deposited in the wake one at a time at specified intervals and then allowed to move under their own mutual interactions. After a sufficient number of rings have been deposited in the wake, a stabilized trajectory is obtained down which all subsequent rings pass. This trajectory is used to represent the wake trajectory of an equivalent rotor. The RVM yields a time history of the radial and axial components of displacement and velocity of each ring released into the wake. This information is used to position the propeller wake.

In accordance with Figure 2 and Figure 19, the coordinates of the tip vortex are given by

$$\bar{\xi}_{iR} = \sum_{\delta=1}^{(i-1)} \left[V_{\delta T}^{R} \left(\frac{\Delta\psi}{\Omega} \right) \cos\left(\{KA - i\} \right) \Delta\psi \right] + R \cos\left(\{KA - i\} \Delta\psi, \right. \quad (21)$$

$$\bar{\eta}_{iR} = \sum_{\delta=1}^{(i-1)} \left[V_{\delta T}^{R} \left(\frac{\Delta\psi}{\Omega} \right) \sin\left(\{KA - i\} \right) \Delta\psi \right] + R \sin\left(\{KA - i\} \Delta\psi \right) \quad (22)$$

$$\bar{\zeta}_{iR} = \sum_{\delta=1}^{(i-1)} \left[W_{\delta T}^{R} \left(\frac{\Delta\psi}{\Omega} \right) \right] \quad (23)$$

where

$V_{\delta T}^{R}$ = radial velocity of the ring at time δ *

$W_{\delta T}^{R}$ = axial velocity of the ring at time δ

R = distance from centerline of rotation to blade tip.

To position the wake mesh interior to the tips, it is assumed that the inboard elements of vorticity are translated with the same axial velocity as the tip, while the radial velocity is taken as proportional to $\left(\frac{r}{R} \right) V_{\delta T}^{R}$. Thus Equations (21) through (23) become, for any point in the wake,

$$\bar{\xi}_{ij} = \sum_{\delta=1}^{(i-1)} \left[\left(\frac{r_j}{R} \right) V_{\delta T}^{R} \left(\frac{\Delta\psi}{\Omega} \right) \cos\left(\{KA - i\} \Delta\psi \right) \right] + r_j \cos\left(\{KA - i\} \Delta\psi \right) \quad (24)$$

$$\bar{\eta}_{ij} = \sum_{\delta=1}^{(i-1)} \left[\left(\frac{r_j}{R} \right) V_{\delta T}^{R} \left(\frac{\Delta\psi}{\Omega} \right) \sin\left(\{KA - i\} \Delta\psi \right) \right] + r_j \sin\left(\{KA - i\} \Delta\psi \right) \quad (25)$$

$$\bar{\zeta}_{ij} = \sum_{\delta=1}^{(i-1)} \left[W_{\delta T}^{R} \left(\frac{\Delta\psi}{\Omega} \right) \right]. \quad (26)$$

Now if we evaluate the perturbation velocities due to the wing and nacelle at the points ($\bar{\xi}_{ij}$, $\bar{\eta}_{ij}$, $\bar{\zeta}_{ij}$) and denote them as

*Note: Recall that for the steady-state conditions, time and azimuthal position are synonymous.

$V^N_{\delta j}$ = radial velocity at j^{th} wake point at time δ due to the nacelle

$W^N_{\delta j}$ = axial velocity at j^{th} wake point at time δ due to the nacelle

$q^{Wx}_{\delta j}$ = X component of velocity at j^{th} wake point at time δ due to the wing

$q^{Wy}_{\delta j}$ = Y component of velocity at j^{th} wake point at time δ due to the wing

$q^{Wz}_{\delta j}$ = Z component of velocity at j^{th} wake point at time δ due to the wing

and include the perturbing effect of the free stream, we can write Equations (24) through (26) as

$$\xi_{ij} = \left[r_j + \left(\frac{r_j}{R}\sum_{\delta=1}^{(i-1)} V^R_{\delta T} + \sum_{\delta=1}^{(i-1)} V^N_{\delta j}\right)\left(\frac{\Delta\psi}{\Omega}\right)\right]\cos\left(\{KA-i\}\Delta\psi\right) + \sum_{\delta=1}^{(i-1)} q^{Wx}_{\delta j}\left(\frac{\Delta\psi}{\Omega}\right) + V_f \sin\tau\left(\frac{\Delta\psi}{\Omega}\right)(i-1) \quad (27)$$

$$\eta_{ij} = \left[r_j + \left(\frac{r_j}{R}\sum_{\delta=1}^{(i-1)} V^R_{\delta T} + \sum_{\delta=1}^{(i-1)} V^N_{\delta j}\right)\right]\left(\frac{\Delta\psi}{\Omega}\right)\sin\left(\{KA-i\}\Delta\psi\right) + \sum_{\delta=1}^{(i-1)} q^{Wy}_{\delta j}\left(\frac{\Delta\psi}{\Omega}\right) \quad (28)$$

$$\zeta_{ij} = \sum_{\delta=1}^{(i-1)}\left[W^R_{\delta T} + W^N_{\delta i}\right]\left(\frac{\Delta\psi}{\Omega}\right) + \sum_{\delta=1}^{(i-1)} q^{Wz}_{\delta j}\left(\frac{\Delta\psi}{\Omega}\right) + \left[V_f\cos\tau\right]\left(\frac{\Delta\psi}{\Omega}\right)(i-1) \quad (29)$$

Equations (27) through (29) define the coordinates of any point in the wake mesh under the influence of wake contraction (axial and radial velocity variations), wing, nacelle, and free-stream velocity.

In the above development, it has been assumed that the blade azimuthal increments, $\Delta\psi$, are all equal. The radial increments may have any distribution desired.

LIST OF SYMBOLS FOR APPENDIX I

i	integer denoting azimuthal position in the wake
j	integer denoting radial position in the wake
k	integer denoting radial position of a blade element
KA	integer denoting azimuthal position of blade
$\overline{NA}$	total number of azimuthal stations
$\overline{NR}$	total number of radial stations
$q^{wx}_{\delta_j}$	X component of velocity at j^{th} wake point at time δ due to the wing, ft/sec
$q^{wr}_{\delta_j}$	Y component of velocity at j^{th} wake point at time δ due to the wing, ft/sec
$q^{wz}_{\delta_j}$	Z component of velocity at j^{th} wake point at time δ due to the wing, ft/sec
r_j	radial distance from centerline of rotation to the j^{th} wake point, ft
R	distance from centerline of rotation to the blade tip, ft
V_f	free-stream velocity, ft/sec
$V^R_{\delta T}$	radial velocity of the ring at time δ, ft/sec
$V^N_{\delta_j}$	radial velocity at j^{th} wake point at time δ due to the nacelle, ft/sec
W	number of revolutions of wake
$W^R_{\delta T}$	axial velocity of the ring at time δ, ft/sec
$W^N_{\delta_j}$	axial velocity at j^{th} wake point at time δ due to nacelle, ft/sec
(X_o, Y_o, Z_o)	nonrotating coordinates fixed at prop hub
$(\zeta, \eta, \zeta)_{ij}$	coordinates of the ij^{th} wake point
τ	angle free stream makes with thrust axis, deg.
ψ	azimuthal position, deg.
$\Delta\psi$	azimuthal increments, deg.
Ω	rotor speed, radians/sec

APPENDIX II

THE WING AND NACELLE MODELS

NACELLE MODEL

To model the aerodynamic effect of the nacelle, we replace it by a Rankine body of equivalent length and projected frontal area. Since the velocity distribution induced by the Rankine body is axially symmetric, only the radial and axial velocity components need be given:

$$V^N(r,Z) = \frac{V_R h \sqrt{h^2+\bar{a}^2}}{4}\left[\frac{x}{\left[r^2+(L-\bar{a}+Z)^2\right]^{3/2}} - \frac{x}{\left[r^2+(L+\bar{a}+Z)^2\right]^{3/2}}\right] \qquad (30)$$

$$W^N(r,Z) = \frac{V_R h \sqrt{h^2+\bar{a}^2}}{4}\left[\frac{(L-\bar{a}+Z)}{\left[r^2+(L-\bar{a}+Z)^2\right]^{3/2}} - \frac{(L+\bar{a}+Z)}{\left[r^2+(L+\bar{a}+Z)^2\right]^{3/2}}\right] \qquad (31)$$

where

V^N = radial velocity induced by nacelle

W^N = axial velocity induced by nacelle

V_R = velocity which the nacelle "sees"

h = Rankine body radius (maximum)

L = Rankine body semilength

$a = \frac{\bar{a}}{h}$ (note: to determine $\bar{a}$, $\left[\frac{(x^2-a^2)^2}{x} = \sqrt{1+a^2}\right]$ must be solved)

$x = \frac{L}{h}$

r = radial position at which velocity is desired

Z = axial position at which velocity is desired

If we consider the velocities V^N and W^N to lie in a plane defined by the axis of rotation of the prop and the blade radius at some azimuthal position, ψ , then we can resolve the V^N and W^N velocity components into the fixed (X_o , Y_o , Z_o) system shown in Figure 19 . We need only multiply V^N by $\cos\psi$ and $\sin\psi$ to obtain the velocity components along X_o and Y_o axes, respectively. The W^N component lies along the Z_o axis and needs no further manipulation.

Note that the (V^N, W^N) of this Appendix correspond directly to the ($V_{\delta_j}^N$, $W_{\delta_j}^N$) of Appendix I. The subscripts δ_j denote the evaluation of (V^N, W^N) at the points in the wake identified by δ and j .

To obtain the v_j^N referred to in Equation (8), page 12, the (V^N, W^N) are evaluated at the j^{th} blade element and resolved perpendicular to the airfoil chord.

WING MODEL

The wing is represented aerodynamically as a bound vortex placed at the quarterchord of the wing. The velocities induced by the wing at any point in the field are given, in the fixed coordinate system, as

$$q^{WX} = \frac{\Gamma_W}{4\pi} K \left[m_a n_b - n_a m_b \right] \tag{32}$$

$$q^{WY} = \frac{\Gamma_W}{4\pi} K \left[n_a l_b - l_a n_b \right] \tag{33}$$

$$q^{WZ} = \frac{\Gamma_W}{4\pi} K \left[l_a m_b - m_a l_b \right] \tag{34}$$

where

Γ_W = wing bound vortex strength

$$K = \frac{r_a + r_b}{r_a r_b \left[r_a r_b + \ell_a \ell_b + m_a m_b + n_a n_b \right]}$$

$$\left.\begin{aligned} r_i^2 &= \ell_i^2 + m_i^2 + n_i^2 \\ \ell_i &= X - \xi_i \\ m_i &= Y - \eta_i \\ n_i &= Z - \zeta_i \end{aligned}\right\} \quad i = a, b$$

(X, Y, Z) coordinates in the fixed system of the point at which the wing induced velocity is desired

(ξ_a, η_a, ζ_a) "a" end of bound vortex

(ξ_b, η_b, ζ_b) "b" end of bound vortex.

The velocities (q^{Wx}, q^{Wy}, q^{Wz}) correspond directly to the $(q^{Wx}_{\delta_j}, q^{Wy}_{\delta_j}, q^{Wz}_{\delta_j})$ of Appendix I. The subscripts δ_j denote evaluation of (q^{Wx}, q^{Wy}, q^{Wz}) at the points in the wake identified by δ and j .

Similarly the v_j^W of Equation (8), page 12, is obtained by evaluating the velocity components of this Appendix at the j^{th} blade element for a given blade azimuthal position and resolving them into a component normal to the airfoil chord.

See Appendix III for more information on the derivation of Equations (32), (33), and (34).

LIST OF SYMBOLS FOR APPENDIX II

a	$\frac{\bar{a}}{h}$ (note: to determine $\bar{a}$, $\left[\frac{(\chi^2-a^2)^2}{\chi} = \sqrt{1+a^2}\right]$ must be solved)
h	Rankine body radius (maximum), ft
K	$\left[r_a+r_b\right] / r_a r_b \left[r_a r_b + \ell_a \ell_b + m_a m_b + n_a n_b\right]$
L	Rankine body semilength, ft
$\ell_{a,b}$	$X - \xi_{a,b}$, ft
$m_{a,b}$	$Y - \eta_{a,b}$, ft
$n_{a,b}$	$Z - \zeta_{a,b}$, ft
q^{WX}	X component of the wing induced velocity, ft/sec
q^{WY}	Y component of the wing induced velocity, ft/sec
q^{WZ}	Z component of the wing induced velocity, ft/sec
r	radial position at which velocity is desired, ft
r_a^2	$\ell_a^2 + m_a^2 + n_a^2$, ft^2
r_b^2	$\ell_b^2 + m_b^2 + n_b^2$, ft^2
V^N	radial velocity induced by nacelle, ft/sec
V_R	velocity which the nacelle "sees", ft/sec
W^N	axial velocity induced by nacelle, ft/sec
(X, Y, Z)	coordinates in the fixed system of the point at which the wing induced velocity is desired
χ	$\frac{L}{h}$
z	axial position at which velocity is desired, ft
Γ_W	wing bound vortex strength, ft^2/sec
(ξ_a, η_a, ζ_a)	"a" end of bound vortex
(ξ_b, η_b, ζ_b)	"b" end of bound vortex

APPENDIX III

DERIVATION OF VELOCITY INDUCED BY THE WAKE

The induced velocity, $\vec{q}$, at any point P due to an arbitrarily oriented vortex element of strength γ per unit length is (in vector notation)

$$\vec{dq} = \frac{\gamma}{4\pi|\vec{r}|^3}(\vec{ds} \times \vec{r}) \tag{35}$$

$$\vec{q} = \frac{\gamma}{4\pi}\int_a^b \frac{\vec{ds} \times \vec{r}}{|\vec{r}|^3} \tag{36}$$

where

$$\vec{ds} = dX_o\vec{i} + dY_o\vec{j} + dZ_o\vec{k}$$

$\vec{i},\vec{j},\vec{k}$ = are unit vectors along the X_o, Y_o, Z_o axes

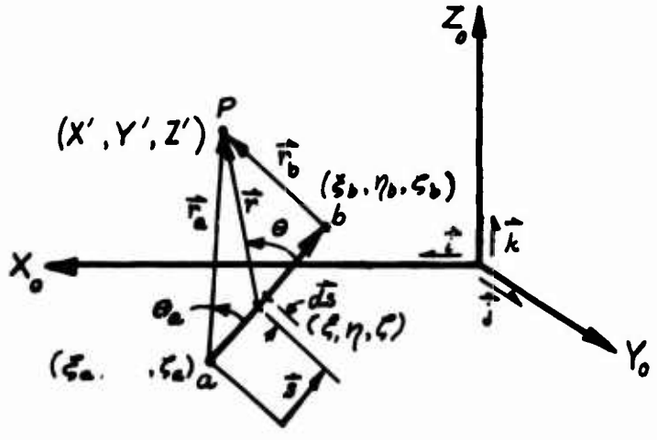

SENSE OF γ POSITIVE FROM a TO b.

Figure 20. ARBITRARILY ORIENTED VORTEX ELEMENT

The velocity components of Equation (36) can be written in terms of the coordinates of the end points of the elemental vortex and the coordinates of the point at which the velocities are desired. Thus,

$$q_{X_o} = \frac{\gamma}{4\pi}\left[\frac{(r_a + r_b)}{r_a r_b (r_a r_b + l_a l_b + m_a m_b + n_a n_b)}\right]\left[m_a n_b - n_a m_b\right] \tag{37}$$

$$q_{Y_o} = \frac{\gamma}{4\pi}\left[\frac{(r_a + r_b)}{r_a r_b (r_a r_b + \ell_a \ell_b + m_a m_b + n_a n_b}\right]\left[n_a \ell_b - \ell_a n_b\right] \qquad (38)$$

$$q_{Z_o} = \frac{\gamma}{4\pi}\left[\frac{(r_a + r_b)}{r_a r_b (r_a r_b + \ell_a \ell_b + m_a m_b + n_a n_b}\right]\left[\ell_a m_b - m_a \ell_b\right] \qquad (39)$$

where

$$r_a^2 = \ell_a^2 + m_a^2 + n_a^2$$

$$r_b^2 = \ell_b^2 + m_b^2 + n_b^2$$

$$\ell_a = X' - \xi_a$$

$$\ell_b = X' - \xi_b$$

$$m_a = Y' - \eta_a$$

$$m_b = Y' - \eta_b$$

$$n_a = Z' - \zeta_a$$

$$n_b = Z' - \zeta_b .$$

The components given by Equations (37) through (39) are applicable to both the bound vortex of the wing and the elemental vortices of the wake.

To determine the induced velocity perpendicular to the blade chord at any azimuthal and radial position of the blade due to a single arbitrarily oriented vortex element, we must make a transformation from the fixed (X_o, Y_o, Z_o) coordinate system to the (X, Y, Z) coordinate system rotating with the blade. Consider Figure 21 (all quantities shown are positive).

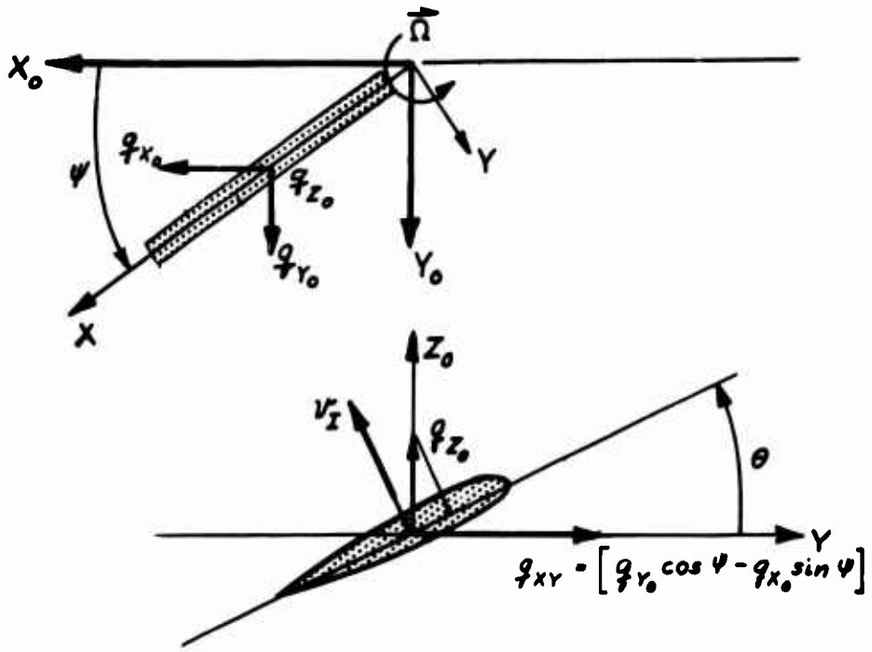

Figure 21. INDUCED VELOCITIES IN FIXED AND ROTATING FRAMES

Thus, in terms of the components (q_{X_o} , q_{Y_o} , q_{Z_o}) and the azimuthal position of the blade, the perpendicular velocity can be written as

$$v^I = \left[q_{X_o} \sin\psi - q_{Y_o} \cos\psi\right] \sin\theta + q_{Z_o} \cos\theta. \tag{40}$$

If we now define the geometric portion of Equations (37) through (39) as follows,

$$\frac{q_{X_o}}{\gamma} = \frac{1}{4\pi}\left[\frac{(r_a + r_b)}{r_a r_b (r_a r_b + \ell_a \ell_b + m_a m_b + n_a n_b)}\right](m_a n_b - n_a m_b) \equiv \sigma_{X_o}$$

$$\frac{q_{Y_o}}{\gamma} = \frac{1}{4\pi}\left[\frac{(r_a + r_b)}{r_a r_b (r_a r_b + \ell_a \ell_b + m_a m_b + n_a n_b)}\right](n_a \ell_b - \ell_a n_b) \equiv \sigma_{Y_o}$$

$$\frac{q_{Z_o}}{\gamma} = \frac{1}{4\pi}\left[\frac{(r_a + r_b)}{r_a r_b (r_a r_b + \ell_a \ell_b + m_a m_b + n_a n_b)}\right](\ell_a m_b - m_a \ell_b) \equiv \sigma_{Z_o},$$

then Equation (40) can be written as

$$v^I = \left[\left\{\sigma_{x_o} \sin\psi - \sigma_{y_o} \cos\psi\right\} \sin\theta + \sigma_{z_o} \cos\theta\right] \gamma$$

or simply as

$$v^I = \overline{\sigma}\gamma. \tag{41}$$

Equation (41) was written for one point and one vortex element. To determine the net contribution at some point j due to all the vortices i in the wake, we simply form

$$v_j^I = \sum_{i=1}^{\infty} \overline{\sigma}_{ij} \gamma_i \tag{42}$$

where $\overline{\sigma}_{ij}$ denotes the geometric influence function of the i^{th} vortex element at the j^{th} point.

LIST OF SYMBOLS FOR APPENDIX III

$(\vec{i}, \vec{j}, \vec{k})$	unit vectors along (X_o, Y_o, Z_o) axes
$\ell_{a,b}$	$X' - \xi_{a,b}$, ft
$m_{a,b}$	$Y' - \eta_{a,b}$, ft
$n_{a,b}$	$Z' - \zeta_{a,b}$, ft
$(q_{X_o}, q_{Y_o}, q_{Z_o})$	wake induced velocity components referenced to (X_o, Y_o, Z_o) system, ft/sec
$r^2_{a,b}$	$\ell^2_{a,b} + m^2_{a,b} + n^2_{a,b}$, ft^2
v_j^I	velocity perpendicular to the airfoil chord of the j^{th} blade element due to the wake, ft/sec
(X, Y, Z)	coordinate system rotating with the blade
(X', Y', Z')	coordinates in (X_o, Y_o, Z_o) system of point at which wake induced velocity is computed
(X_o, Y_o, Z_o)	nonrotating coordinates fixed at hub
γ_i	strength per unit length of the i^{th} vortex element, ft^2/sec
θ	angle between the airfoil chord and the prop plane, deg.
$(\sigma_{X_o}, \sigma_{Y_o}, \sigma_{Z_o})$	induced velocities in (X_o, Y_o, Z_o) directions due to a vortex element of unit strength, 1/ft
$\bar{\sigma}_{ij}$	geometric portion of the Biot-Savart law for the effect of the i^{th} vortex element at the j^{th} point, 1/ft
ψ	azimuthal position of the blade, deg.

APPENDIX IV
DERIVATION OF THE ELASTIC EQUATIONS OF MOTION

A Lagrangian approach is used to derive the equations of motion of the rotating propeller. In addition to the previously defined coordinate systems, (X_o, Y_o, Z_o) fixed in space and (X, Y, Z) rotating with the blade, the local coordinate system $(\xi, \eta, \bar{\zeta})$ as shown in Figure 22 is introduced. In Figure 22 the axes ξ and X are normal to the plane of the paper.

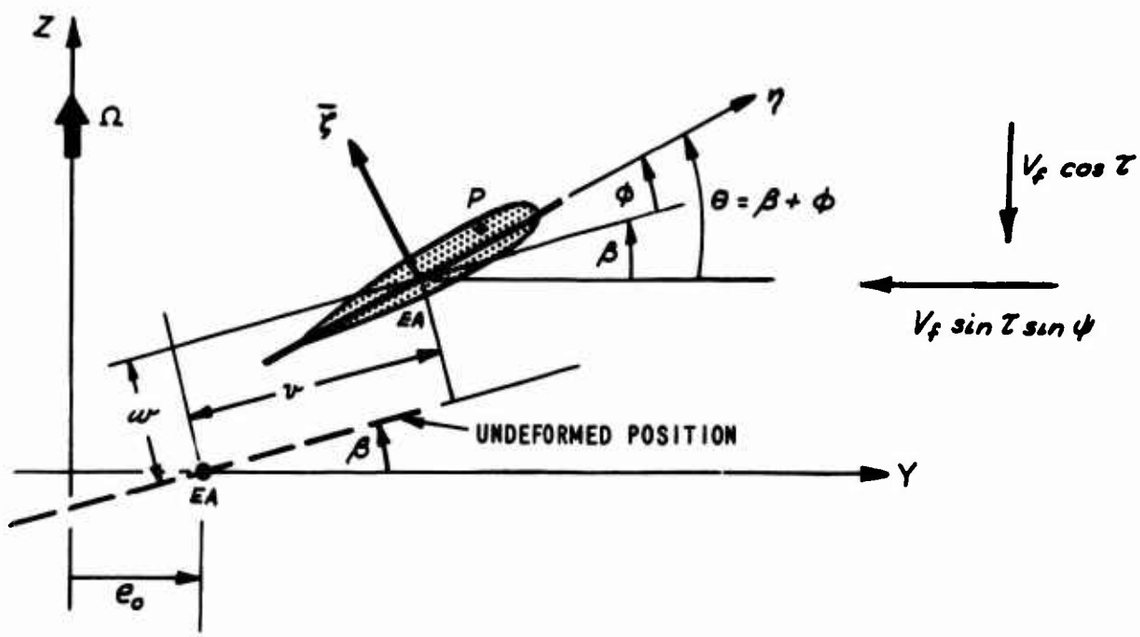

Figure 22. LOCAL BLADE SEGMENT COORDINATE SYSTEM

The airfoil is assumed to be thin and symmetrical. The components of the total velocity in the rotating frame of any point P on the airfoil is given by (dot indicates differentiation with respect to time)

$$V_X = \dot{X} - \Omega Y + V_f \sin\tau \cos\psi \qquad (43)$$

$$V_Y = \dot{Y} + \Omega X - V_f \sin\tau \cos\psi \tag{44}$$

$$V_Z = \dot{Z} + V_f \cos\tau \tag{45}$$

where

$$X = \xi$$

$$Y = e_o + \eta\cos\theta - \bar{\zeta}\sin\theta + v\cos\beta - w\sin\beta$$

$$Z = \eta\sin\theta + \bar{\zeta}\cos\theta + w\cos\beta + v\sin\beta,$$

and the displacements (v, w) are taken parallel and perpendicular to the undisturbed airfoil chord. The displacements (v, w, ϕ) are expanded in terms of the generalized coordinates ($w^{(p)}$, $v^{(q)}$, $\phi^{(s)}$), which are the tip deflections of the uncoupled flapwise, chordwise, and torsional vibration modes of the blade:

$$w = \sum_t w^{(t)} f_w^{(t)} \tag{46}$$

$$v = \sum_q v^{(q)} f_v^{(q)} \tag{47}$$

$$\phi = \sum_s \phi^{(s)} f_\phi^{(s)} \tag{48}$$

where

$f_w^{(t)}$ = flatwise mode shape of the t^{th} mode

$f_v^{(q)}$ = edgewise mode shape of the q^{th} mode

$f_\phi^{(s)}$ = torsional mode shape of the s^{th} mode

$w^{(t)}$ = tip deflection of the t^{th} flatwise mode; dependent on time only

$v^{(q)}$ = tip deflection of the q^{th} edgewise mode; dependent on time only

$\phi^{(s)}$ = tip deflection of the s^{th} torsional mode; dependent on time only.

At this point it was decided to employ the coupled flatwise-edgewise modes as the generalized coordinates. Hence, Equation (47) became

$$v = \sum_{p}^{-} w^{(p)} k_v^{(p)} f_v^{(p)} \tag{49}$$

where $k_v^{(p)}$ = constant determined from a coupled mode analysis as is the coupled mode shape $f_v^{(p)}$. Equation (46) has the same form when the coupled mode shape $f_w^{(p)}$ is used.

Lagrange's equations of motion are given as

$$\frac{d}{dt}\left(\frac{\partial T}{\partial \dot{q}_r}\right) - \frac{\partial T}{\partial q_r} - \frac{d}{dt}\left(\frac{\partial U}{\partial \dot{q}_r}\right) + \frac{\partial U}{\partial q_r} + \frac{\partial D}{\partial \dot{q}_r} = Q_r \tag{50}$$

where

T = kinetic energy of the system

U = potential energy of the system

D = dissipation function

Q_r = r^{th} generalized force

q_r = r^{th} generalized coordinate

$\dot{q}_r$ = r^{th} generalized velocity

r = number of generalized coordinates required to define the system.

The hub is assumed to have infinite impedance, and therefore each blade may be treated as an independent cantilever blade. Hence, the total kinetic energy of one blade is given by

$$T = \frac{1}{2}\int_{\substack{BLADE \\ MASS}} (V_x^2 + V_y^2 + V_z^2)\, dm \tag{51}$$

where for a blade of uniform density,

$$dm = \rho dA dX.$$

The potential energy is (following Reference 9)

$$U = \frac{1}{2}\int_{r_o}^{R} \left\{ EI_1 \zeta^2 + EI_2 \lambda^2 + \left[GJ + EB_1 \left(\frac{\partial \beta}{\partial X} \right)^2 \right] \left(\frac{d\phi}{dX} \right)^2 - 2EB_2 \lambda \frac{d\beta}{dX} \frac{d\phi}{dX} \right\} dX$$

$$- \int_{r_o}^{R} X e_A \lambda_\theta \, dX + \int_{r_o}^{R} X k_A^2 \left\{ \frac{1}{2} \left(\frac{d\phi}{dX} \right)^2 + \frac{d\beta}{dX} \frac{d\phi}{dX} \right\} dX \qquad (52)$$

where

$$\zeta = \frac{d^2 w}{dX^2} + 2 \frac{d\beta}{dX} \frac{dv}{dX} + \frac{d^2 \beta}{dX^2} v - \left(\frac{d\beta}{dX} \right)^2 w$$

$$\lambda = \frac{d^2 v}{dX^2} - 2 \frac{d\beta}{dX} \frac{dw}{dX} - \frac{d^2 \beta}{dX} w - \left(\frac{d\beta}{dX} \right)^2 v$$

$$\lambda_\theta = \lambda - 2 \frac{d\phi}{dX} \frac{dw}{dX} - \frac{d^2 \phi}{dX^2} w - 2 \frac{d\beta}{dX} \frac{d\phi}{dX} v$$

$$X = \Omega^2 \int_X^R mX \, dX$$

EI_1 = flexural rigidity about major neutral axis

EI_2 = flexural rigidity about minor neutral axis

GJ = torsional rigidity

$$e_A = \frac{1}{A} \int_A \eta \, dA$$

$$k_A^2 = \frac{1}{A} \int_A \eta^2 dA$$

$$EB_1 = E \int_A \eta^2 (\eta^2 - k_A^2) \, dA$$

$$EB_z = E\int_A \eta(\eta^2 - k_A^2)\, dA.$$

The dissipation energy is obtained by assuming that the total system damping can be defined in terms of a summation of the damping proportional to the displacement and in phase with the velocity of each degree of freedom of the system when they are individually performing simple harmonic motions.

The tip deflections are expanded in a Fourier series on ψ, the azimuthal position (which is equivalent to time for the steady-state case):

$$w^{(p)} = a_{w_0}^{(p)} + \sum_{n=1}^{\frac{\overline{NA}}{2}-1} a_{w_n}^{(p)} \cos(n\psi) + \sum_{n=1}^{\frac{\overline{NA}}{2}-1} b_{w_n}^{(p)} \sin(n\psi). \tag{53}$$

$$\phi^{(s)} = a_{\phi_0}^{(s)} + \sum_{n=1}^{\frac{\overline{NA}}{2}-1} a_{\phi_n}^{(s)} \cos(n\psi) + \sum_{n=1}^{\frac{\overline{NA}}{2}-1} b_{\phi_n}^{(s)} \sin(n\psi). \tag{54}$$

The generalized force is similarly expanded in a Fourier series:

$$Q_{w^{(p)}} = \mathcal{F}_{w_0}^{(p)} + \sum_{n=1}^{\frac{\overline{NA}}{2}-1} {}^{c}\mathcal{F}_{w_n}^{(p)} \cos(n\psi) + \sum_{n=1}^{\frac{\overline{NA}}{2}-1} {}^{s}\mathcal{F}_{w_n}^{(p)} \sin(n\psi). \tag{55}$$

$$Q_{\phi^{(s)}} = \mathcal{F}_{\phi_0}^{(s)} + \sum_{n=1}^{\frac{\overline{NA}}{2}-1} {}^{c}\mathcal{F}_{\phi_n}^{(s)} \cos(n\psi) + \sum_{n=1}^{\frac{\overline{NA}}{2}} {}^{s}\mathcal{F}_{\phi_n}^{(s)} \sin(n\psi). \tag{56}$$

The Lagrangian is applied to Equations (51) through (56), and like coefficients are equated. The resultant set of equations is given in the following: For the 0^{th} harmonic, $n = 0$

$$\left|\begin{array}{c|c} -\Omega^2\left[E_{ww}^{(ij)} - Q_{ww}^{(ij)}\right] + F_{ww}^{(ij)} & -\Omega^2\left[C_{w\phi}^{(ij)} - P_{w\phi}^{(ij)}\right] - G_{w\phi}^{(ij)} \\ \hline -\Omega^2\left[C_{\phi w}^{(ij)} - P_{\phi w}^{(ij)}\right] - G_{\phi w}^{(ij)} & \Omega^2\left[E_{\phi}^{(ij)}\right] + F_{\phi}^{(ij)} \end{array}\right| \left\{\begin{array}{c} a_{w_0}^{(j)} \\ \hline a_{\phi_0}^{(j)} \end{array}\right\} = \left\{\begin{array}{c} \mathcal{F}_{w_0}^{(i)} + F_{ww}^{(i)} - \Omega^2\left[A_{ww}^{(i)} + Q_{ww}^{(i)}\right] \\ \hline \mathcal{F}_{\phi_0}^{(i)} - F_{\phi}^{(i)} - \Omega^2 A_{\phi}^{(i)} \end{array}\right\}.$$

For 1st to m^{th} harmonic, $n = 1, 2, \ldots (\overline{NA}/2 - 1)$

$$
\begin{vmatrix}
-n^2\Omega^2 B_{ww}^{(ij)} + F_{ww}^{(ij)} & -n^2\Omega^2 D_{w\phi}^{(ij)} - G_{w\phi}^{(ij)} & g_{ww}^{(j)} F_{ww}^{(ij)} & -g_{\phi}^{(j)} G_{w\phi}^{(ij)} \\
-\Omega^2\left[E_{ww}^{(ij)} - Q_{ww}^{(ij)}\right] & -\Omega^2\left[C_{w\phi}^{(ij)} - P_{w\phi}^{(ij)}\right] & & \\
-n^2\Omega^2 D_{\phi w}^{(ij)} - G_{\phi w}^{(ij)} & -n^2\Omega^2 B_{\phi}^{(ij)} + F_{\phi}^{(ij)} & -g_{ww}^{(j)} G_{\phi w}^{(ij)} & g_{\phi}^{(j)} F_{\phi}^{(ij)} \\
-\Omega^2\left[C_{\phi w}^{(ij)} - P_{\phi w}^{(ij)}\right] & + \Omega^2 E_{\phi}^{(ij)} & & \\
-g_{ww}^{(j)} F_{ww}^{(ij)} & g_{\phi}^{(j)} G_{w\phi}^{(ij)} & -n^2\Omega^2 B_{ww}^{(ij)} + F_{ww}^{(ij)} & -n^2\Omega^2 D_{w\phi}^{(ij)} - G_{w\phi}^{(ij)} \\
 & & -\Omega^2\left[E_{ww}^{(ij)} - Q_{ww}^{(ij)}\right] & -\Omega^2\left[C_{w\phi}^{(ij)} - P_{w\phi}^{(ij)}\right] \\
g_{ww}^{(j)} G_{\phi w}^{(ij)} & -g_{\phi}^{(j)} F_{\phi}^{(ij)} & -n^2\Omega^2 D_{\phi w}^{(ij)} - G_{\phi w}^{(ij)} & -n^2\Omega^2 B_{\phi}^{(ij)} + F_{\phi}^{(ij)} \\
 & & -\Omega^2\left[C_{\phi w}^{(ij)} - P_{\phi w}^{(ij)}\right] & + \Omega^2 E_{\phi}^{(ij)}
\end{vmatrix}
\begin{Bmatrix} a_{ww_n}^{(j)} \\ a_{\phi_n}^{(j)} \\ b_{ww_n}^{(j)} \\ b_{\phi_n}^{(j)} \end{Bmatrix}
=
\begin{Bmatrix} {}^{c}\mathcal{F}_{ww_n}^{(i)} \\ {}^{c}\mathcal{F}_{\phi_n}^{(i)} \\ {}^{s}\mathcal{F}_{ww_n}^{(i)} \\ {}^{s}\mathcal{F}_{\phi_n}^{(i)} \end{Bmatrix}
$$

where

$$A_w^{(r)} \equiv \int_{r_o}^{R} m(e_o + e\cos\beta)(f_w^{(r)}\sin\beta - k_v^{(r)} f_v^{(r)}\cos\beta)\, dX$$

$$A_\phi^{(s)} \equiv \int_{r_o}^{R} (me_o e + \mu\cos\beta)\sin\beta\, f_\phi^{(s)}\, dX$$

$$B_w^{(rp)} \equiv \int_{r_o}^{R} m(f_w^{(r)} f_w^{(p)} + k_v^{(r)} f_v^{(r)} k_v^{(p)} f_v^{(p)})\, dX$$

$$B_\phi^{(sq)} \equiv \int_{r_o}^{R} \mu f_\phi^{(s)} f_\phi^{(q)}\, dX$$

$$C_{w\phi}^{(pq)} \equiv \int_{r_o}^{R} (me\sin\beta)(f_w^{(p)}\sin\beta - k_v^{(p)} f_v^{(p)}\cos\beta) f_\phi^{(q)}\, dX$$

$$D_{w\phi}^{(pq)} \equiv \int_{r_o}^{R} me\, f_w^{(p)} f_\phi^{(q)}\, dX$$

$$E_w^{(rp)} \equiv \int_{r_o}^{R} m(f_w^{(r)}\sin\beta - k_v^{(r)} f_v^{(r)}\cos\beta)(f_w^{(p)}\sin\beta - k_v^{(p)} f_v^{(p)}\cos\beta)\, dX$$

$$E_\phi^{(sq)} \equiv \int_{r_o}^{R} (me_o e\cos\beta + \mu\cos 2\beta) f_\phi^{(s)} f_\phi^{(q)}\, dX$$

$$F_w^{(rp)} \equiv \int_{r_o}^{R} (EI_1 f_\zeta^{(r)} f_\zeta^{(p)} + EI_2 f_\lambda^{(r)} f_\lambda^{(p)})\, dX$$

$$F_\phi^{(sq)} \equiv \int_{r_o}^{R} \left\{ GJ + EB_1 \left(\frac{d\beta}{dX}\right)^2 + X k_A^2 \right\} \frac{df_\phi^{(s)}}{dX} \frac{df_\phi^{(q)}}{dX}\, dX$$

$$F_w^{(r)} \equiv \int_{r_o}^{R} X e_A f_\lambda^{(r)}\, dX$$

$$F_\phi^{(s)} \equiv \int_{r_o}^{R} X k_A^2 \frac{d\beta}{dX} \frac{df_\phi^{(s)}}{dX}\, dX$$

$$G_{\omega\phi}^{(pq)} \equiv \int_{r_o}^{R} \left(EB_2 \frac{d\beta}{dX} f_\lambda^{(p)} \frac{df_\phi^{(q)}}{dX} - \mathbb{X} e_A f_{\omega\phi}^{(pq)} \right) dX$$

$$Q_\omega^{(rp)} \equiv \int_{r_o}^{R} mX g_\omega^{(rp)} dX$$

$$Q_\omega^{(r)} \equiv \int_{r_o}^{R} mX e \left(k_\nu^{(r)} \frac{df_\nu^{(r)}}{dX} - \frac{d\beta}{dX} f_\omega^{(r)} \right) dX$$

$$P_{\omega\phi}^{(pq)} \equiv \int_{X_o}^{R} mX e \left(\frac{df_\omega^{(p)}}{dX} + \frac{d\beta}{dX} k_\nu^{(p)} f_\nu^{(p)} \right) f_\phi^{(q)} dX$$

$\mathbb{X}$ $\equiv$ INITIAL AXIAL TENSION $= \Omega^2 \int_{X_o}^{R} mX dX$

$$f_\zeta^{(p)} \equiv \frac{d^2 f_\omega^{(p)}}{dX^2} + 2 \frac{d\beta}{dX} k_\nu^{(p)} \frac{df_r^{(p)}}{dX} + \frac{d^2\beta}{dX^2} k_\nu^{(p)} f_r^{(p)} - \left(\frac{d\beta}{dX} \right)^2 f_\omega^{(p)}$$

$$f_\lambda^{(p)} \equiv k_\nu^{(p)} \frac{d^2 f_\nu^{(p)}}{dX^2} - 2 \frac{d\beta}{dX} \frac{df_\omega^{(p)}}{dX} - \frac{d^2\beta}{dX^2} f_\omega^{(p)} - \left(\frac{d\beta}{dX} \right)^2 k_\nu^{(p)} f_\nu^{(p)}$$

$$f_{\omega\phi}^{(pq)} \equiv 2 \frac{df_\phi^{(q)}}{dX} \frac{df_\omega^{(p)}}{dX} + \frac{d^2 f_\phi^{(q)}}{dX^2} f_\omega^{(p)} + 2 \frac{d\beta}{dX} \frac{df_\phi^{(q)}}{dX} k_\nu^{(p)} f_\nu^{(p)}$$

$$g_\omega^{(rp)} = \int_{r_o}^{X} \left\{ \left(\frac{df_\omega^{(r)}}{dX} + \frac{d\beta}{dX} k_\nu^{(r)} f_\nu^{(r)} \right) \left(\frac{df_\omega^{(p)}}{dX} + \frac{d\beta}{dX} k_\nu^{(p)} f_\nu^{(p)} \right) \right.$$
$$\left. + \left(k_\nu^{(r)} \frac{df_\nu^{(r)}}{dX} - \frac{d\beta}{dX} f_\omega^{(r)} \right) \left(k_\nu^{(p)} \frac{df_\nu^{(p)}}{dX} - \frac{d\beta}{dX} f_\omega^{(p)} \right) \right\} dX.$$

LIST OF SYMBOLS FOR APPENDIX IV

$a_{w_n}^{(p)}, b_{w_n}^{(p)}$	Fourier coefficients of blade flatwise response in the p^{th} degree of freedom
A	blade cross sectional area
$a_{\phi_n}^{(s)}, b_{\phi_n}^{(s)}$	Fourier coefficients of blade torsional response in the s^{th} degree of freedom
D	dissipation function
EB_1	$E\int_A \eta^2(\eta^2 - k_A^2)\,dA$, ft^4-lb
EB_2	$E\int_A \eta(\eta^2 - k_A^2)\,dA$, ft^3-lb
EI_1	flexural rigidity about major neutral axis, ft^2-lb
EI_2	flexural rigidity about minor neutral axis, ft^2-lb
e	distance from elastic axis to center of gravity of section, ft ($e \equiv 0$ for the case shown in Figure 22)
e_A	$\frac{1}{A}\int_A \eta\,dA$, ft
e_o	distance from the X -axis to the elastic axis of the undisturbed airfoil, ft
${}^{c}\mathcal{F}_{w_n}^{(p)}, {}^{s}\mathcal{F}_{w_n}^{(p)}$	Fourier coefficients of the generalized force in the p^{th} degree of freedom
${}^{c}\mathcal{F}_{w_n}^{(s)}, {}^{s}\mathcal{F}_{w_n}^{(s)}$	Fourier coefficients of the generalized force in the s^{th} degree of freedom
$f_v^{(q)}$	edgewise mode shape of the q^{th} m
$f_w^{(p)}$	flatwise mode shape of the p^{th} mode
$f_\phi^{(s)}$	torsional mode shape of the s^{th} mode
GJ	torsional rigidity, ft^2-lb
k_A^2	$\frac{1}{A}\int_A \eta^2\,dA$, ft^2
$k_v^{(p)}$	flatwise to edgewise coupling constant in the p^{th} mode
m	blade mass per unit span, slugs/ft
Q_r	r^{th} generalized force
q_r	r^{th} generalized coordinate
$\dot{q}_r$	r^{th} generalized velocity

R	radial distance from centerline of rotation to blade tip, ft
r_o	radial distance from centerline of rotation to blade root, ft
T	kinetic energy of the system
U	potential energy of the system
V_f	free-stream velocity, ft/sec
v	elastic deformation of the elastic axis parallel to the undisturbed position of the airfoil chord, ft/sec
$v^{(q)}$	tip deflection of the q^{th} edgewise mode; dependent on time only, ft
V_X, V_Y, V_Z	(X, Y, Z) components of the total velocity of any point on the blade, ft/sec
w	elastic deformation of the elastic axis perpendicular to the undisturbed position of the airfoil chord, ft/sec
$w^{(p)}$	tip deflection of the p^{th} flatwise mode; dependent on time only, ft
(X, Y, Z)	rotating coordinates fixed at the hub
(X_o, Y_o, Z_o)	nonrotating coordinates fixed at the hub
$\mathbb{X}$	$\Omega^2 \int_X^R mX dX$, lb
β	angle of built-in twist with respect to the prop plane, radians
θ	total geometric angle of blade section, radians
μ	section polar mass moment or inertia, slug/ft
$(\xi, \eta, \bar{\zeta})$	local coordinates fixed at the blade elastic axis
ρ	blade local density, slugs/ft^3
τ	angle free-stream velocity makes with thrust axis, deg.
ϕ	torsional displacement of a given blade element, radians
$\phi^{(s)}$	tip deflection of the s^{th} torsional mode; dependent on time only, radians
ψ	azimuthal position of blade, deg.
Ω	rotor speed, radians/sec

APPENDIX V

DERIVATION OF THE GENERALIZED FORCES

By definition, the product of the generalized force times the generalized coordinates, summed overall degrees of freedom, must equal the total virtual work done:

$$\sum_i \vec{F_i} \cdot \vec{dr_i} = \sum_j Q_j \, dq_j$$

where

$\vec{F_i}$ = net force acting on i^{th} particle (vector)

Q_j = j^{th} generalized force

$\vec{dr_i}$ = displacement of i^{th} particle (vector)

dq_j = differential of j^{th} generalized coordinate

i = number of particles

j = number of generalized coordinates.

Now since the position vector $\vec{r_i}$ is a function of the q_j's,

$$\vec{dr_i} = \sum_j \frac{\partial \vec{r_i}}{\partial q_j} \, dq_j \; ;$$

hence,

$$\sum_i \vec{F_i} \cdot \left(\sum_j \frac{\partial \vec{r_i}}{\partial q_j} \, dq_i \right) = \sum_j Q_j \, dq_j \; .$$

For each j, therefore,

$$\sum_i \vec{F_i} \cdot \left(\frac{\partial \vec{r_i}}{\partial q_i} \right) = Q_j \; . \qquad (57)$$

Now, to form the virtual work done by the force acting on the prop blades due to a virtual infinitesimal displacement of the generalized

coordinates, define the following geometry:

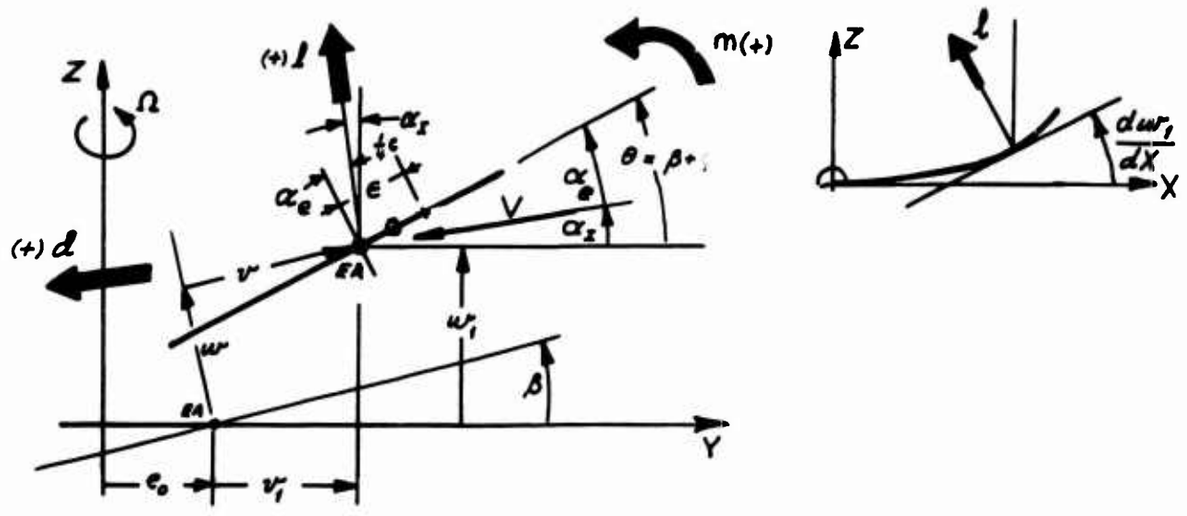

Figure 23. GEOMETRY FOR DERIVATION OF GENERALIZED FORCES

where

lift/unit span = l, taken positive perpendicular up from local relative velocity

drag/unit span = d, taken positive in direction of local relative velocity

moment/unit span = m, taken positive leading edge up about the elastic axis.

Then at each section of the blade and each azimuthal station,

$$l = \rho V \Gamma = b \rho V^2 c_l \tag{58}$$

$$d = b \rho V^2 c_d \tag{59}$$

$$m = \epsilon \left[\ell \cos \alpha_e + d \sin \alpha_e \right] + 2b^2 \rho V^2 c_{m_{c/4}} . \tag{60}$$

Now the virtual work is given by

$$dW = \int_{r_o}^{R} \left\{ F_X dX + F_Y dY + F_Z dZ + m d\theta \right\} dX \tag{61}$$

where

$$F_X = -\ell \sin \frac{dw_1}{dX} \approx -\ell \frac{dw_1}{dX}$$

$$F_Y = -\left[\ell \cos \frac{dw_1}{dX} \right] \sin \alpha_I - \left[d \right] \cos \alpha_I \approx -\left[\ell \sin \alpha_I + d \cos \alpha_I \right]$$

$$F_Z = \left[\ell \cos \frac{dw_1}{dX} \right] \cos \alpha_I - \left[d \right] \sin \alpha_I \approx \left[\ell \cos \alpha_I - d \sin \alpha_I \right]$$

α_I = arc tan $\left[\frac{V_Z}{V_Y} \right]$

V_Z = total velocity perpendicular to (X, Y) plane

V_Y = total velocity in the plane of (X, Y).

To obtain the differentials $dX, dY, dZ,$ and $d\theta$ e the following:

$$X = r - \frac{1}{2} \int_{r_o}^{x} \left\{ \left(\frac{\partial w_1}{\partial x} \right)^2 + \left(\frac{\partial v_1}{\partial x} \right)^2 \right\} dx - \frac{\partial w_1}{\partial x} \epsilon \sin \theta - \frac{\partial v_1}{\partial x} \epsilon \cos \theta \tag{62}$$

$$Y = e_o + v_1 \tag{63}$$

$$Z = w_1 \tag{64}$$

where

$$v_1 = v\cos\beta - w\sin\beta$$

$$w_1 = w\cos\beta + v\sin\beta$$

The displacements (v, w, ϕ) are expanded in terms of the generalized coordinates ($w^{(p)}$, $v^{(p)}$, $\phi^{(q)}$) which are the tip deflections of the flapwise, edgewise, and torsional vibration modes of the blade:

$$w = \sum_p w^{(p)} f_w^{(p)}$$

$$v = \sum_p w^{(p)} k_v^{(p)} f_v^{(p)} = \sum_p v^{(p)} f_v^{(p)}$$

$$\phi = \sum_q \phi^{(q)} f_\phi^{(q)} .$$

Introduce the small angle approximations

$$\phi << 1$$

and

$$\sin\alpha_e \approx \alpha_e .$$

Form the differentials of Equations (62) through (64) and substitute into Equation (61) to obtain the virtual work:

$$\begin{aligned} dW = &+\sum_p \int_{r_0}^{R} \ell\epsilon \left(f_w^{(p)} \frac{d\beta}{dX} + k_v^{(p)} \frac{df_w^{(p)}}{dX} \right) \left[\sum_r w^{(r)} \left(\left\{ \frac{df_w^{(r)}}{dX} + k_v^{(r)} f_v^{(r)} \frac{d\beta}{dX} \right\} \cos\beta + \left\{ k_v^{(r)} \frac{df_r^{(r)}}{dX} + f_w^{(r)} \frac{d\beta}{dX} \right\} \sin\beta \right) \right] dX\, dw^{(p)} \\ &- \sum_p \int_{r_0}^{R} (\ell \sin\alpha_I + d\cos\alpha_I)(k_v^{(p)} f_v^{(p)} \cos\beta - f_w^{(p)} \sin\beta)\, dX\, dw^{(p)} \\ &+ \sum_p \int_{r_0}^{R} (\ell\cos\alpha_I - d\sin\alpha_I)(f_w^{(p)} \cos\beta + k_v^{(p)} f_v^{(p)} \sin\beta)\, dX\, dw^{(p)} \\ &+ \sum_q \int_{r_0}^{R} \left[\epsilon(\ell\cos\alpha_e + d\sin\alpha_e) + 2\rho V^2 b^2 c_{m_{c/4}} \right] f_\phi^{(q)} dX\, d\phi^{(q)} . \end{aligned} \tag{65}$$

Apply Equation (57) through Equation (65) to obtain the generalized force:

$$Q_w^{(p)} = +\int_{r_o}^{R} \ell e \left(f_w^{(p)} \frac{d\beta}{dX} + k_w^{(p)} \frac{df_w^{(p)}}{dX} \right) \left[\sum_r w^{(r)} \left(\left\{ \frac{df_w^{(r)}}{dX} + k_v^{(r)} f_v^{(r)} \frac{d\beta}{dX} \right\} \cos\beta + \left\{ k_w^{(r)} \frac{df_v^{(r)}}{dX} - f_w^{(r)} \frac{d\beta}{dX} \right\} \sin\beta \right) \right] dX$$

$$-\int_{r_o}^{R} (\ell \sin\alpha_I + d\cos\alpha_I)(k_v^{(p)} f_v^{(p)} \cos\beta - f_w^{(p)} \sin\beta)\, dX \qquad (66)$$

$$+\int_{r_o}^{R} (\ell \cos\alpha_I - d\sin\alpha_I)(f_w^{(p)} \cos\beta + k_v^{(p)} f_v^{(p)} \sin\beta)\, dX \qquad \begin{matrix} p = 1,2,3,4 \\ r = 1,2,3,4 \end{matrix}$$

and

$$Q_\phi^{(s)} = \int_{r_o}^{R} \left[\epsilon(\ell \cos\alpha_e + d\sin\alpha_e) + 2\rho V^2 b^2 c_{m_{c/4}} \right] f_\phi^{(q)} dX. \qquad q = 1,2 \qquad (67)$$

Note that Equations (66) and (67) correspond to the left-hand side of Equations (55) and (56) of Appendix IV, page 73.

LIST OF SYMBOLS FOR APPENDIX V

b	local blade semichord, ft
c_d	section drag coefficient
c_ℓ	section lift coefficient
$c_{m_{c/4}}$	section moment coefficient about quarterchord
d	drag per unit span, lb/ft
$\vec{dr_i}$	displacement of i^{th} particle (vector), ft
dq_j	differential of j^{th} generalized coordinate
e_o	distance from X -axis to the elastic axis of the undisturbed airfoil, ft
$\vec{F_i}$	net force acting on i^{th} particle (vector), lb
$f_v^{(p)}$	edgewise mode shape of the p^{th} mode
$f_w^{(p)}$	flatwise mode shape of the p^{th} mode
$f_\phi^{(q)}$	torsional mode shape of the q^{th} mode
i	number of particles
j	number of generalized coordinates
$k_w^{(p)}$	flatwise to edgewise coupling constant in the p^{th} mode
ℓ	lift per unit span, lb/ft
m	moment per unit span, ft-lb/ft
Q_j	j^{th} generalized force
V	total local velocity, ft/sec
V_Y, V_Z	components of the total velocity in the plane of (X, Y) and perpendicular to the plane of (X, Y), ft/sec
v, w	elastic displacement of the elastic axis parallel and perpendicular to the undisturbed airfoil chord, ft
v_1, w_1	elastic displacement of the elastic axis parallel and perpendicular to the (X, Y) plane, ft
$w^{(p)}$	tip deflection of the p^{th} flatwise mode, ft
(X, Y, Z)	rotating coordinates fixed at the hub
α_e	local effective angle of attack, radians
α_I	angle local total velocity makes with the prop plane, radians
β	local built-in twist, radians

ϵ	distance from elastic axis to quarterchord, ft
θ	total geometric angle of blade section, radians
ρ	density of air, slugs/ft^3
ϕ	total elastic torsional displacement of the airfoil section, radians
$\phi^{(s)}$	tip deflection of the s^{th} torsional mode, radians

APPENDIX VI

DERIVATION OF BLADE STRESSES

From Reference 7, the longitudinal strains were derived. Assume that the airfoil consists of a bundle of fibers. Now pass a plane perpendicular to the elastic axis (EA) and consider the location of a fiber through the point P before and after a deformation:

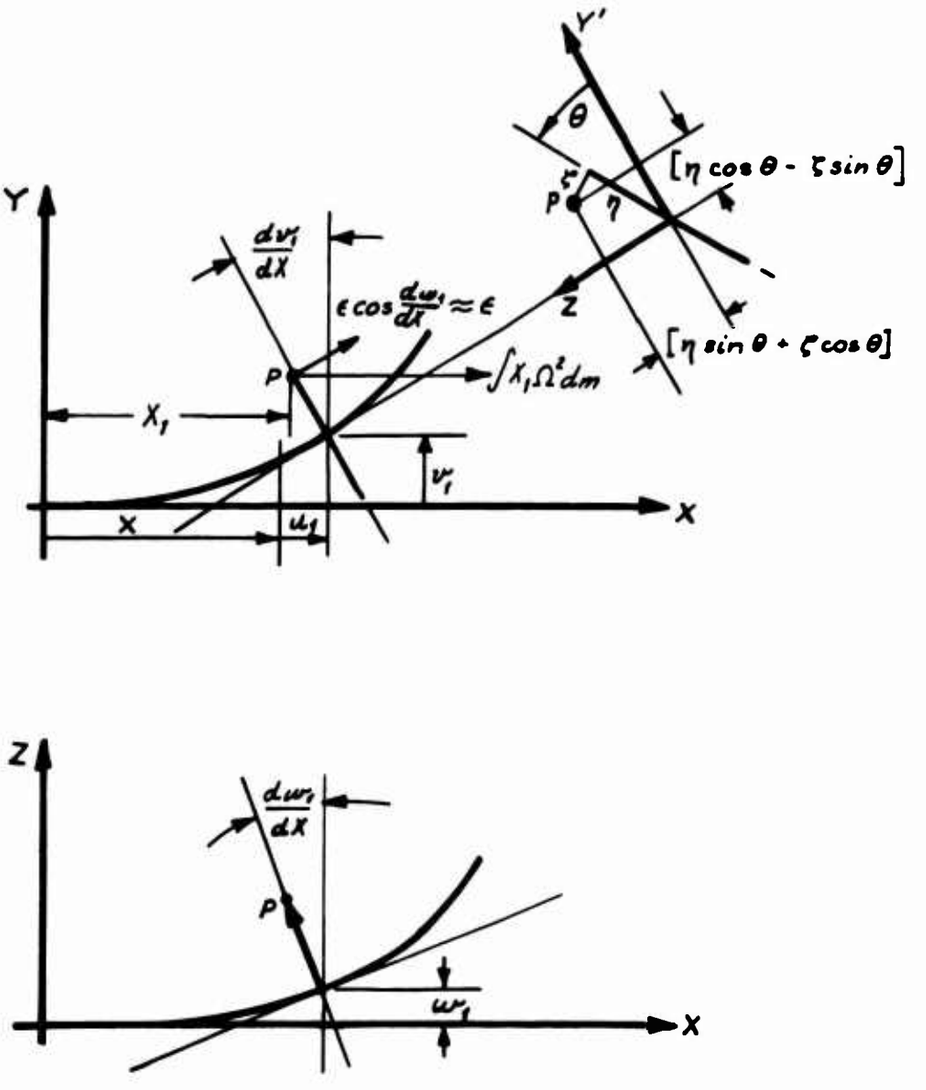

Figure 24. ELASTIC DEFORMATIONS

$$X_1 = X + u_1 - \frac{dv_1}{dX}\left[\eta\cos\theta - \zeta\sin\theta\right] - \frac{dw_1}{dX}\left[\eta\sin\theta + \zeta\cos\theta\right] \tag{68}$$

$$Y_1 = Y + v_1 + \left[\eta\cos\theta - \zeta\sin\theta\right] + \left[\eta\sin\theta + \zeta\cos\theta\right] \tag{69}$$

$$Z_1 = Z + w_1 + \left[\eta\sin\theta + \zeta\cos\theta\right]. \tag{70}$$

(u_1, v_1, w_1) = displacement in (X, Y, Z) directions of point P from its undeformed position

θ = built-in twist + torsional deformation = $\beta + \phi$

(X, Y, Z) = coordinates of the point P, prior to deformation

(X_1, Y_1, Z_1) = coordinates of the point P, after its deformation

To find the change in fiber length of the fiber through the point P, form

$$(ds_1)^2 = (dX_1)^2 + (dY_1)^2 + (dZ_1)^2. \tag{71}$$

The original fiber length was

$$(ds)^2 = (dX)^2 + (dY)^2 + (dZ)^2. \tag{72}$$

The tensile strain in the fiber is defined as

$$\epsilon = \frac{(ds_1) - (ds)}{ds}. \tag{73}$$

Thus (the primes indicate differentiation with respect to x),

$$\epsilon = u_1' - \eta\left(V_1''\cos\beta + W_1''\sin\beta\right) - \zeta\left(-V_1''\sin\beta + W_1''\cos\beta\right) + \left(\eta^2 + \zeta^2\right)\beta'\phi', \tag{74}$$

or in terms of the displacements parallel and perpendicular to the undisturbed airfoil chord (v, w), introduce the transformation

$$v_1 = v\cos\beta - w\sin\beta \tag{75}$$

$$w_1 = v\sin\beta - w\cos\beta . \tag{76}$$

Since the fiber is assumed to be effective in uniaxial strain only, the stress follows immediately as

$$\sigma = E\epsilon. \tag{77}$$

To eliminate u_1', equilibrium of forces in the X direction is imposed:

$$\mathcal{X} = E\int_{\eta_{TE}}^{\eta_{LE}}\int_{-t/2}^{t/2}\epsilon\, d\zeta\, d\eta \tag{78}$$

where

(η_{LE}, η_{TE}) = leading- and trailing-edge coordinates

t = the airfoil thickness

$\mathcal{X}$ = centrifugal and aerodynamic forces acting in X direction

$$= \int_X^R X\Omega^2\, dm + F_X .$$

The assumption of a thin symmetrical airfoil is applied and the equation is solved for u_1'; the result is used in Equation (74). Now the transformation of coordinates is made and Equation (77) becomes, in terms of the displacements parallel and perpendicular to the chord,

$$\sigma = E\left[\frac{\mathcal{X}}{EA} + (e_A - \eta)\left\{V'' - 2\beta'W' - \beta''W - (\beta')^2V\right\}\right.$$
$$\left. - \zeta\left\{W'' + 2\beta'V' + \beta''V - (\beta')^2W\right\} + (\eta^2 + \zeta^2 - k_A^2)\beta'\phi'\right] \tag{79}$$

where the primes indicate differentiation with respect to X and

E = Young's modulus

A = airfoil cross-sectional area

$$k_A^2 = \frac{1}{A}\int_A \eta^2 dA$$

$$e_A = \frac{1}{A}\int_A \eta\, dA \quad \text{(for a symmetric airfoil).}$$

To account for the torsional strains and stresses, it is assumed that there exists a St. Venant's torsional resisting stress which would

develop if the blade were not initially twisted, plus a shearing component developed by the longitudinal stress in the fibers. This component develops because of the live twist, ϕ , and also the built-in twist, β .

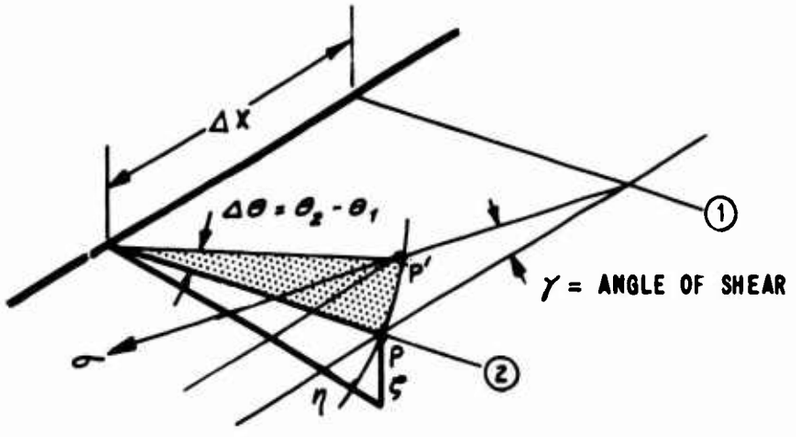

Figure 25. PICTORIAL REPRESENTATION OF TORSIONAL DEFORMATIONS

The in-plane component of fiber stress, σ, is (see Figure 25)

$$\sigma_s = \sigma \sin\gamma \approx \sigma\gamma,$$

but

$$\sqrt{\eta^2+\zeta^2}\,\Delta\theta = \gamma\Delta X;$$

thus,

$$\sigma_s = \sigma\sqrt{\eta^2+\zeta^2}\left(\frac{d\beta}{dX} + \frac{d\phi}{dX}\right). \tag{80}$$

The total resisting torque is given by

$$Q = GJ\phi' + \int_{\eta_{TE}}^{\eta_{LE}}\int_{-t/2}^{t/2} \sigma_s\sqrt{\eta^2+\zeta^2}\,d\zeta\,d\eta \tag{81}$$

where, after accounting for a thin, symmetric airfoil, Equation (81)

becomes

$$Q = \left[GJ + EB_1\left(\frac{d\beta}{dx}\right)^2\right]\frac{d\phi}{dx} + \mathcal{I}k_A^2\left(\frac{d\beta}{dx} + \frac{d\phi}{dx}\right) - EB_2\lambda\frac{d\beta}{dx} \tag{82}$$

where

G = shear modulus

$$J = \frac{4I_Y}{\left(1 + 16\frac{I_Y}{AC^2}\right)}$$

$$B_1 = \int_A \eta^2(\eta^2 - k_A^2)\,dA$$

$$B_2 = \int_A \eta(\eta^2 - k_A^2)\,dA$$

$$k_A^2 = \frac{1}{A}\int_A \eta^2 dA$$

$$\lambda = w'' - 2\beta' w' - \beta'' w + (\beta')^2 w.$$

I_Y = area moment of inertia about ζ

A = cross-sectional area

c = sectional chord

To determine the maximum shear stress, the section was treated as though it were in pure torsion. Then for a symmetrical airfoil (see Reference 12),

$$\sigma_{s_{max}} = \frac{Qs}{J} \tag{83}$$

where

$$s = \frac{D}{1 + \frac{\pi^2 D^4}{16A^2}}\left[1 + 0.15\left(\frac{\pi^2 D^4}{16A^2} - \frac{D}{2\bar{r}}\right)\right]$$

$\tilde{r}$ = radius of curvature of boundary at point of tangency

D = diameter of maximum inscribed circle.

Thus, in terms of Equation (82), Equation (83) becomes

$$\sigma_{s_{max}} = \frac{s}{J}\left[\left\{GJ + EB_1\left(\frac{d\beta}{dx}\right)^2\right\}\frac{d\phi}{dx} + \Sigma k_A^2\left(\frac{d\beta}{dx} + \frac{d\phi}{dx}\right) - EB_2\lambda\frac{d\beta}{dx}\right]. \quad (84)$$

The tensile stress at any point in the cross section is given by Equation (79), and the maximum shear stress at any blade section is given by Equation (84).

LIST OF SYMBOLS FOR APPENDIX VI

A	airfoil cross sectional area, ft^2
B_1	$\int_A \eta^2(\eta^2-k_A^2)\,dA$, ft^6
B_2	$\int_A \eta\,(\eta^2-k_A^2)\,dA$, ft^5
c	sectional chord, ft
D	diameter of maximum inscribed circle, ft
E	Young's modulus, lb/ft^2
e_A	$\frac{1}{A}\int_A \eta\,dA$, ft
G	shear modulus, lb/ft^2
I_Y	area moment of inertia about ζ, ft^4
J	$4I_Y/\left(1+16\frac{I_Y}{Ac^2}\right)$, ft^4
k_A^2	$\frac{1}{A}\int_A \eta^2\,dA$, ft^2
Q	total resisting torque at a blade section, lb-ft/ft
$\tilde{r}$	radius of curvature of boundary at point of tangency, ft
s	$\frac{D}{1+\frac{\pi^2D^4}{16A^2}}\left[1+0.15\left(\frac{\pi^2D^4}{16A^2}-\frac{D}{2\tilde{r}}\right)\right]$, ft
t	airfoil thickness distribution, ft
v	displacement of elastic axis parallel to the airfoil chord, ft
w	displacement of elastic axis perpendicular to the airfoil chord,
X	centrifugal and aerodynamic forces acting in x-direction, lb
(X,Y,Z)	rotating coordinates fixed at prop hub
β	local built-in twist, radians
γ	angle of shear, radians
ϵ	tensile strain of a fiber, inches/inch

θ	local total geometric angle ($=\beta+\theta$), radians
λ	$v''-2\beta'w'-\beta''w+(\beta')^2v$
(ξ,η,ζ)	coordinates of a point P in the (ξ,η,ζ) coordinate system fixed at the blade elastic axis
σ	tensile stress of a fiber, lb/ft^2
σ_s	component of σ in the plane of the airfoil section, lb/ft^2
ϕ	total torsional displacement of a section, radians

ft

APPENDIX VII

DERIVATION OF THE QUASI-STEADY DAMPING TERMS

To obtain the quasi-steady damping terms, follow the development given in Appendix V, page 79. For the purpose here, define an approximation to the quasi-steady lift and moment at the j^{th} blade section as follows: (Dot indicates differentiation with respect to time.)

$$\ell_j^{(QSD)} = -b_j \rho V_j a_j \left[\sum_p \dot{w}^{(p)} f_{w_j}^{(p)} + \sum_q n_{3/4 c_j} \dot{\phi}^{(q)} f_{\phi_j}^{(q)} \right] \tag{85}$$

$$m_j^{(QSD)} = \epsilon_j \ell_j^{(QSD)} . \tag{86}$$

Equations (85) and (86) are used to form the virtual work from which the desired quasi-steady damping terms of interest are obtained:

$$Q_w^{(p)} = + \sum_r \dot{w}^{(r)} R_w^{(pr)} + \sum_s \dot{\phi}^{(s)} S_{w\phi}^{(ps)} \tag{87}$$

$$\phi_\phi^{(q)} = - \sum_r \dot{w}^{(r)} T_{\phi w}^{(qr)} - \sum_s \dot{\phi}^{(s)} V_\phi^{(qs)} \tag{88}$$

where

$Q_w^{(p)}$ generalized force in $w^{(p)th}$ mode

$Q_\phi^{(q)}$ generalized force in $\phi^{(q)th}$ mode

$$R_w^{(pr)} = \int_{r_0}^{R} \rho b a f_w^{(r)} \Big\{ V_\phi \cos\tau \left(k_v^{(p)} f_v^{(p)} \cos\beta - f_w^{(p)} \sin\beta \right) - \left(X\Omega \right) \left(f_w^{(p)} \cos\beta + k_v^{(p)} f_v^{(p)} \sin\beta \right) \Big\} dX$$

$$S_{w\phi}^{(ps)} = \int_{r_0}^{R} \rho b a n_{3/4 c} f_\phi^{(s)} \Big\{ V_\phi \cos\tau \left(k_v^{(p)} f_v^{(p)} \cos\beta - f_w^{(p)} \sin\beta \right) - \left(X\Omega \right) \left(f_w^{(p)} \cos\beta + k_v^{(p)} f_v^{(p)} \sin\beta \right) \Big\} dX$$

$$T_{\phi\omega}^{(qr)} = \int_{r_0}^{R} \rho b a \epsilon \left[(X\Omega)^2 + (V_f \cos\tau)^2 \right]^{1/2} f_\phi^{(q)} f_\omega^{(r)} dX$$

$$V_\phi^{(qs)} = \int_{r_0}^{R} \rho b a n_{3/4c} \epsilon \left[(X\Omega)^2 + (V_f \cos\tau)^2 \right]^{1/2} f_\phi^{(q)} f_\omega^{(r)} dX .$$

The above quasi-steady terms are added to both the right-hand side and the left-hand side of the elastic equations of motion of Appendix III, page 64, and treated accordingly. The $Q_\omega^{(p)}$ and $Q_\phi^{(q)}$ will appear implicitly in the ${}^{c}\mathcal{F}_{\omega_n}^{(i)}$, ${}^{s}\mathcal{F}_{\omega_n}^{(i)}$, ${}^{c}\mathcal{F}_{\phi_n}^{(i)}$, and ${}^{s}\mathcal{F}_{\phi_n}^{(i)}$. The $R_\omega^{(pr)}$, $S_{\omega\phi}^{(ps)}$, $T_{\phi\omega}^{(qr)}$ and $V_\phi^{(qs)}$ will appear explicitly as elements of the square matrix on page 74.

LIST OF SYMBOLS FOR APPENDIX VII

a_j	section lift curve slope $(\equiv dc_\ell/d\alpha)_j$
b_j	local blade semichord, ft
$f_v^{(p)}$	edgewise mode shape of p^{th} mode
$f_w^{(p)}$	flatwise mode shape of p^{th} mode
$f_\phi^{(q)}$	torsional mode shape of q^{th} mode
$k_v^{(p)}$	flatwise to edgewise coupling constant in p^{th} mode
$\ell_j^{(QSD)}$	approximation to the quasi-steady lift at the j^{th} blade section, lb
$m_j^{(QSD)}$	approximation to the quasi-steady moment at the j^{th} blade section, ft-lb
V_f	free-stream velocity, ft/sec
V_j	local total velocity, ft/sec
$\dot{w}^{(p)}$	velocity in p^{th} bending mode at blade tip
X	radial distance from centerline of rotation, ft
β	local built-in twist, radians
ϵ_j	distance from elastic axis to quarterchord at j^{th} blade section, ft
$\eta_{3/4c_j}$	distance from elastic axis to three-quarterchord point at j^{th} blade element, ft
γ	angle free-stream velocity makes with thrust axis, deg.
ρ	air density, slugs/ft^3
$\dot{\phi}^{(q)}$	velocity in q^{th} torsion mode at blade tip
Ω	rotor speed, radians/sec

APPENDIX VIII

EXPERIMENTAL STRAIN DATA

The purpose of mounting strain rosettes on the blades was to obtain the true state of stress at the selected blade locations. The strain signals from each gage of the rosette were recorded. Then, at a given point in time, the three strain signals from a given rosette were combined to obtain the principal stresses and directions. From the principal stresses, the longitudinal and shear stresses at the locations of the rosettes were determined. The reduction of the measured strains to stresses required either that all the strains be read simultaneously or that they be in steady state. Neither requirement was truly satisfied for these data. Some of the strain data were reduced, however, by reasoning that, if any record could be found for which the propellers had maintained a fixed phase with respect to one another for the duration of the record, the strains could be considered periodic for that interval, and hence, stresses could be evaluated.

The mean and instantaneous values of the harmonically analyzed experimental stresses and strains are presented in Figures 26 through 29.

The mean longitudinal strains are plotted vs. τ, the angle between the free stream and the thrust axes, in Figure 30.

The effect of the "clean" vs. "dirty" configuration on the strains is indicated in Figures 28, 29, and 30. Figure 30 indicates that the "dirty" configuration had caused only a slight increase in the outboard (3.67 ft) mean longitudinal strain, but had caused a three-fold increase in the mean longitudinal strain at the inboard (2.67 ft) station. A comparison of Figures 28 and 29 indicates that the peak-to-peak amplitude of the longitudinal strain remained essentially the same, but the frequency content was appreciably altered at both stations.

Even under the restrictive assumption noted above, the experimental strains showed appreciable variations in magnitude and frequency content over the time interval recorded. In some cases, the peak-to-peak amplitude more than doubled and the dominant frequency shifted from 1P to 3P. Because of the nonperiodicity of the strains and the sequential method of collecting the strain data, noted previously, the resolved longitudinal and shear stress values are highly questionable, as are the harmonics of the longitudinal strains.

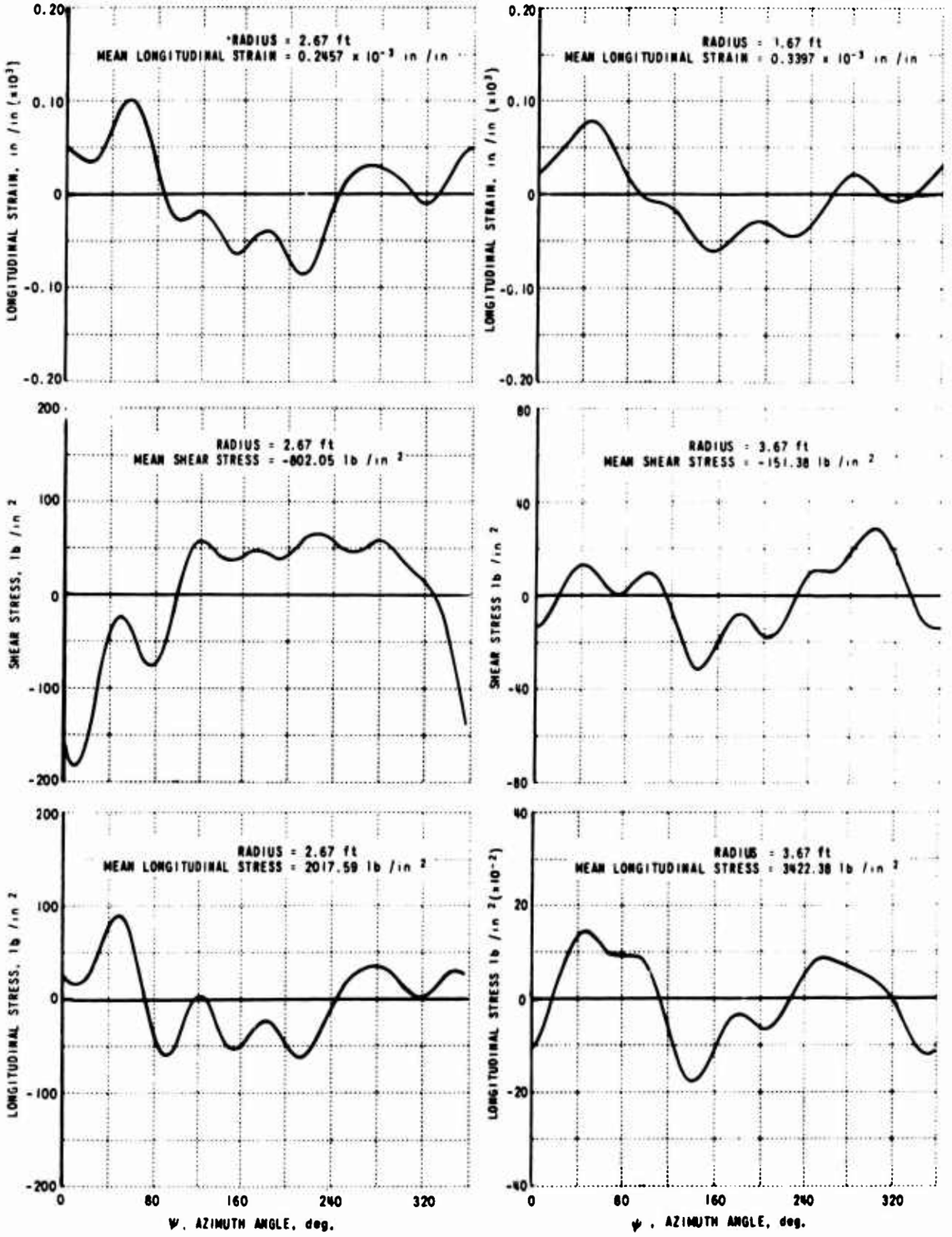

Figure 26. MEAN AND INSTANTANEOUS VALUES OF EXPERIMENTAL STRESSES AND STRAINS AT TWO RADIAL STATIONS FOR V_f = 39.8 ft /sec ; τ = 30°; Ω = 1264 r.p.m.

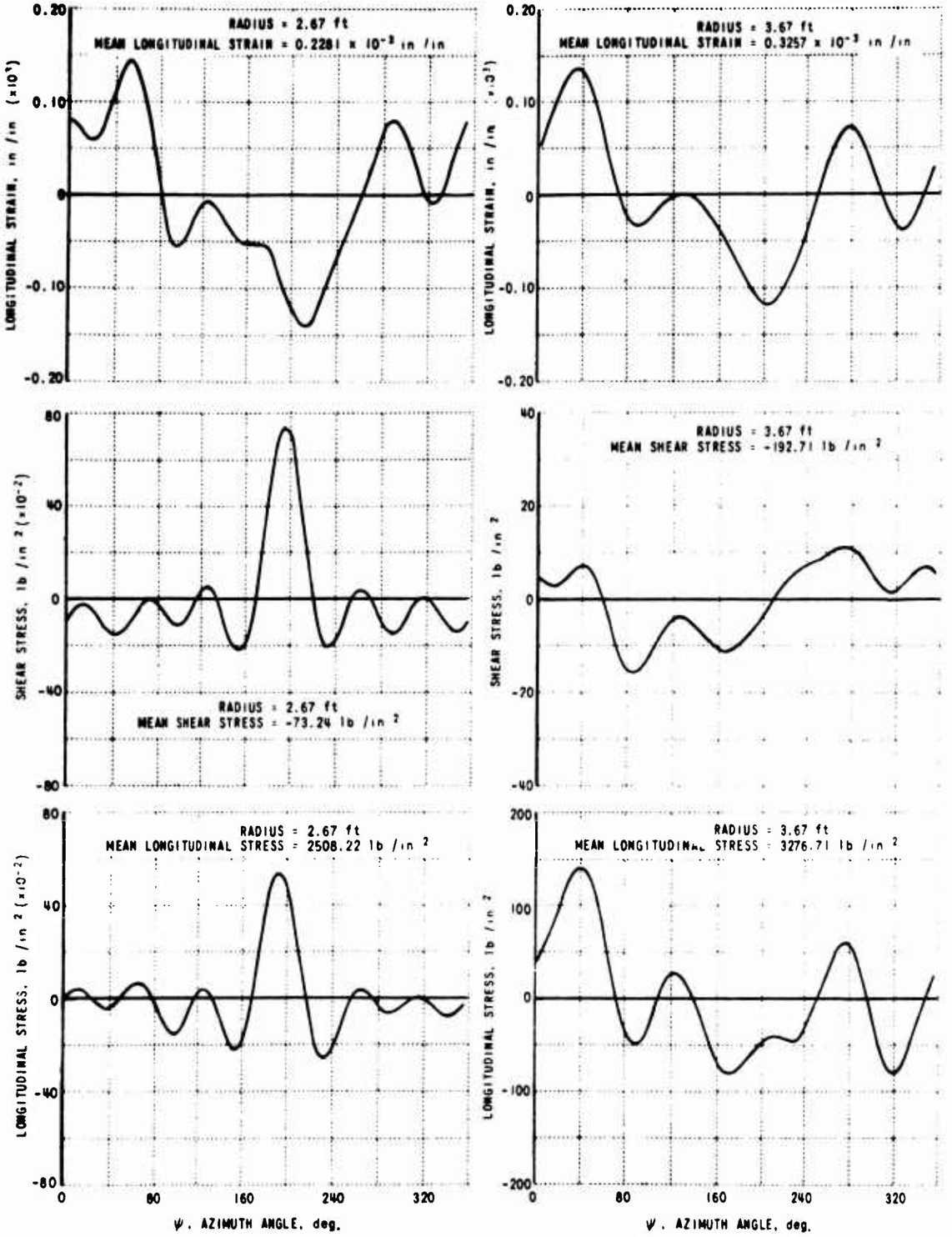

Figure 27. MEAN AND INSTANTANEOUS VALUES OF EXPERIMENTAL STRESSES AND STRAINS AT TWO RADIAL STATIONS FOR V_f = 39.8 ft /sec ; τ = 40°; Ω = 1264 r.p.m.

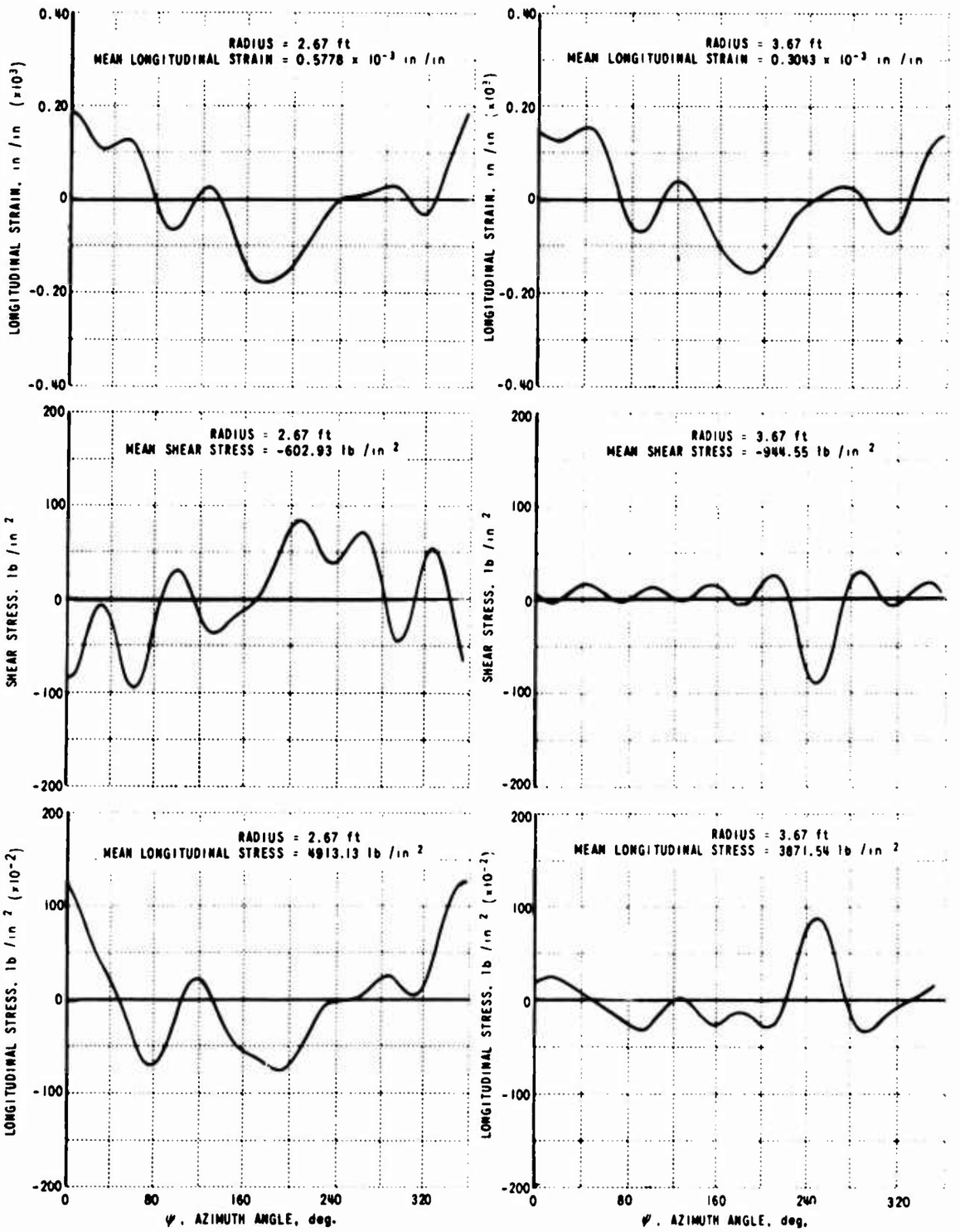

Figure 28. MEAN AND INSTANTANEOUS VALUES OF EXPERIMENTAL STRESSES AND STRAINS AT TWO RADIAL STATIONS FOR V_f = 39.8 ft /sec ; τ = 50°; Ω = 1264 r.p.m.; WITHOUT FLAPS AND SLATS

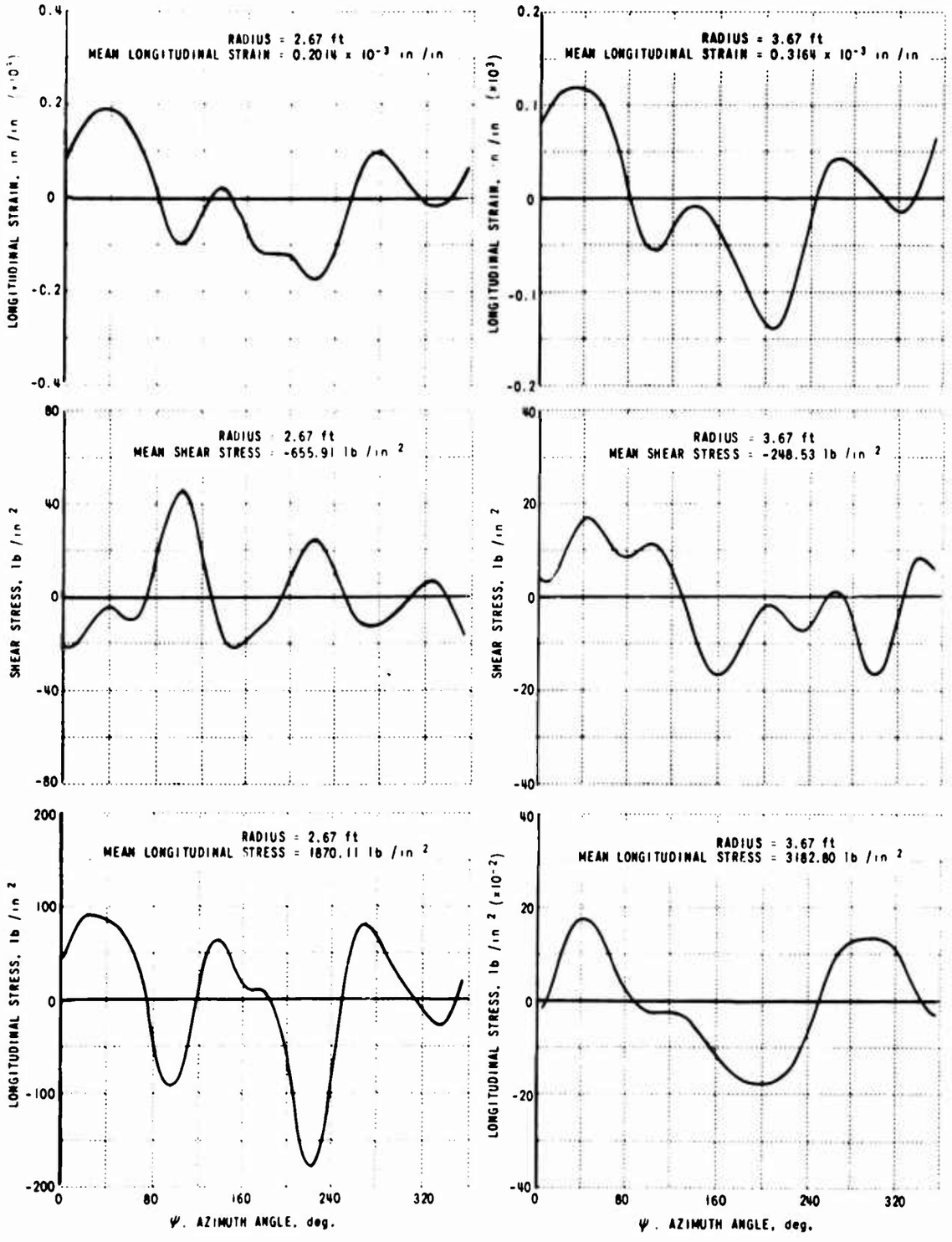

Figure 29. MEAN AND INSTANTANEOUS VALUES OF EXPERIMENTAL STRESSES AND STRAINS AT TWO RADIAL STATIONS FOR V_f = 39.8 ft /sec ; τ = 50 ; Ω = 1264 r.p.m.; WITH FLAPS AND SLATS

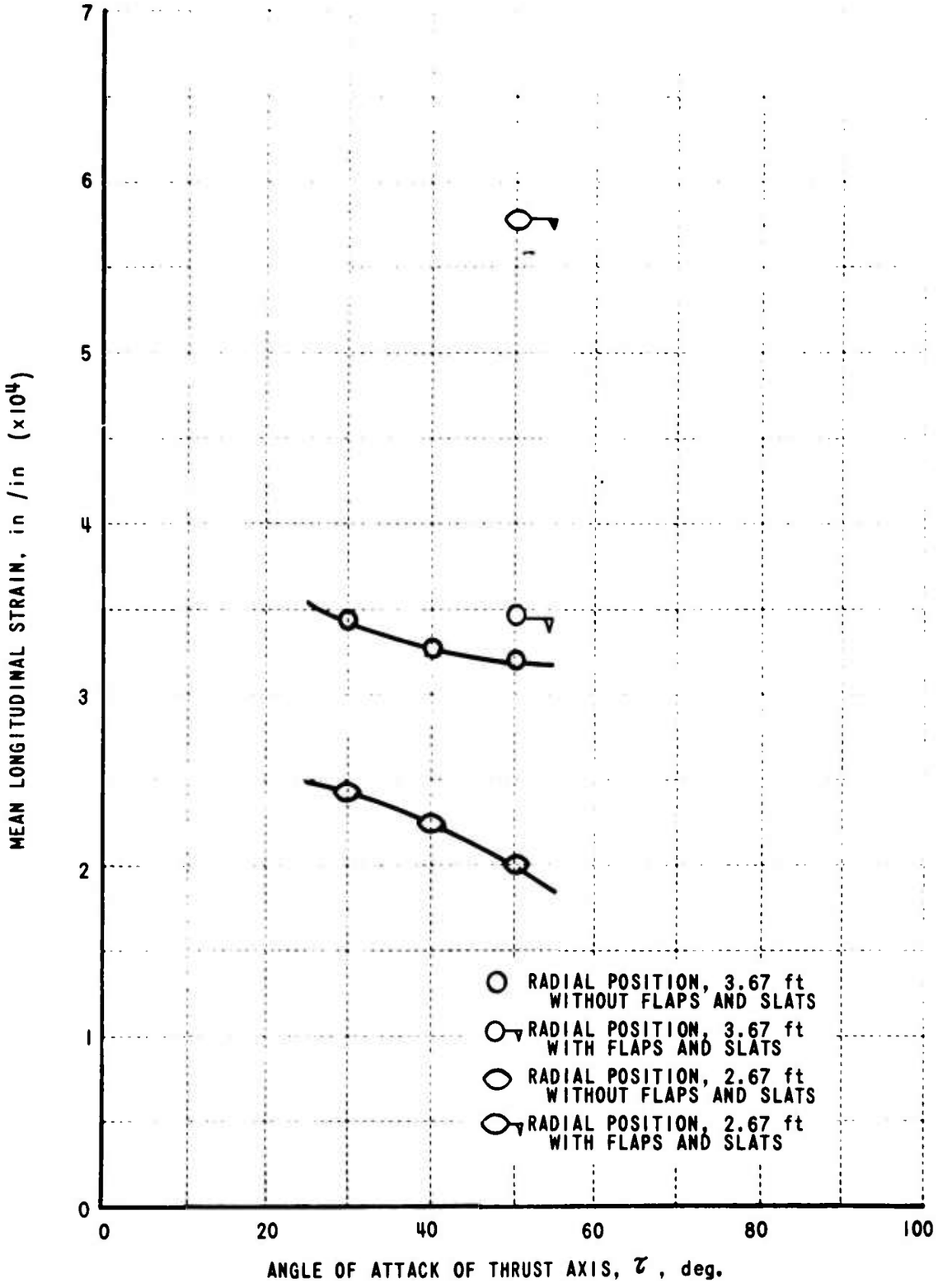

Figure 30. EXPERIMENTAL MEAN LONGITUDINAL STRAIN AT TWO RADIAL STATIONS VS. ANGLE OF ATTACK OF THRUST AXIS

BLANK PAGE

Unclassified

Security Classification

DOCUMENT CONTROL DATA - R&D

(Security classification of title, body of abstract and indexing annotation must be entered when the overall report is classified)

1. ORIGINATING ACTIVITY (Corporate author)	2a. REPORT SECURITY CLASSIFICATION
Cornell Aeronautical Laboratory, Inc. Buffalo, New York 14221	Unclassified
	2b GROUP

3. REPORT TITLE

Development of a Method for Predicting the Performance and Stresses of VTOL-Type Propellers

4. DESCRIPTIVE NOTES *(Type of report and inclusive dates)*

5. AUTHOR(S) *(Last name, first name, initial)*

Trenka, Andrew R.

6. REPORT DATE	7a. TOTAL NO. OF PAGES	7b NO. OF REFS
June 1966	103	14

8a. CONTRACT OR GRANT NO.	9a. ORIGINATOR'S REPORT NUMBER(S)
DA 44-177-AMC-75(T)	USAAVLABS Technical Report 66-26
b. PROJECT NO. Task 1D121401A142	
c.	9b. OTHER REPORT NO(S) *(Any other numbers that may be assigned this report)*
d.	BB-1846-S-1

10. AVAILABILITY/LIMITATION NOTICES

Distribution of this document is unlimited.

11. SUPPLEMENTARY NOTES	12. SPONSORING MILITARY ACTIVITY
	U. S. Army Aviation Materiel Laboratories, Fort Eustis, Virginia

13. ABSTRACT

This report presents a theoretical method which allows the prediction of performance and stress characteristics of a single VTOL-type of propeller-wing-nacelle combination operating in various flight conditions from hovering through transition and into axial flight. The method includes (1) the effects of a distorted wake, i.e., the effects of contraction and radial and axial velocity variations; (2) the effects of hovering close to the ground; (3) the interference effects from a nacelle and wing buried in the propeller slipstream.

Also presented are experimental thrust and torque data. However, because of the insufficient accuracy of the experimental data collected, no definite evaluation of the model is made.

DD FORM 1 JAN 64 1473

Unclassified

Security Classification

Unclassified

Security Classification

14. KEY WORDS	LINK A		LINK B		LINK C	
	ROLE	WT	ROLE	WT	ROLE	WT
Propeller Performance Stresses						

INSTRUCTIONS

1. ORIGINATING ACTIVITY: Enter the name and address of the contractor, subcontractor, grantee, Department of Defense activity or other organization *(corporate author)* issuing the report.

2a. REPORT SECURITY CLASSIFICATION: Enter the overall security classification of the report. Indicate whether "Restricted Data" is included. Marking is to be in accordance with appropriate security regulations.

2b. GROUP: Automatic downgrading is specified in DoD Directive 5200.10 and Armed Forces Industrial Manual. Enter the group number. Also, when applicable, show that optional markings have been used for Group 3 and Group 4 as authorized.

3. REPORT TITLE: Enter the complete report title in all capital letters. Titles in all cases should be unclassified. If a meaningful title cannot be selected without classification, show title classification in all capitals in parenthesis immediately following the title.

4. DESCRIPTIVE NOTES: If appropriate, enter the type of report, e.g., interim, progress, summary, annual, or final. Give the inclusive dates when a specific reporting period is covered.

5. AUTHOR(S): Enter the name(s) of author(s) as shown on or in the report. Enter last name, first name, middle initial. If military, show rank and branch of service. The name of the principal author is an absolute minimum requirement.

6. REPORT DATE: Enter the date of the report as day, month, year; or month, year. If more than one date appears on the report, use date of publication.

7a. TOTAL NUMBER OF PAGES: The total page count should follow normal pagination procedures, i.e., enter the number of pages containing information.

7b. NUMBER OF REFERENCES: Enter the total number of references cited in the report.

8a. CONTRACT OR GRANT NUMBER: If appropriate, enter the applicable number of the contract or grant under which the report was written.

8b, 8c, & 8d. PROJECT NUMBER: Enter the appropriate military department identification, such as project number, subproject number, system numbers, task number, etc.

9a. ORIGINATOR'S REPORT NUMBER(S): Enter the official report number by which the document will be identified and controlled by the originating activity. This number must be unique to this report.

9b. OTHER REPORT NUMBER(S): If the report has been assigned any other report numbers *(either by the originator or by the sponsor)*, also enter this number(s).

10. AVAILABILITY/LIMITATION NOTICES: Enter any limitations on further dissemination of the report, other than those imposed by security classification, using standard statements such as:

(1) "Qualified requesters may obtain copies of this report from DDC."

(2) "Foreign announcement and dissemination of this report by DDC is not authorized."

(3) "U. S. Government agencies may obtain copies of this report directly from DDC. Other qualified DDC users shall request through

_____."

(4) "U. S. military agencies may obtain copies of this report directly from DDC. Other qualified users shall request through

_____."

(5) "All distribution of this report is controlled. Qualified DDC users shall request through

_____."

If the report has been furnished to the Office of Technical Services, Department of Commerce, for sale to the public, indicate this fact and enter the price, if known.

11. SUPPLEMENTARY NOTES: Use for additional explanatory notes.

12. SPONSORING MILITARY ACTIVITY: Enter the name of the departmental project office or laboratory sponsoring *(paying for)* the research and development. Include address.

13. ABSTRACT: Enter an abstract giving a brief and factual summary of the document indicative of the report, even though it may also appear elsewhere in the body of the technical report. If additional space is required, a continuation sheet shall be attached.

It is highly desirable that the abstract of classified reports be unclassified. Each paragraph of the abstract shall end with an indication of the military security classification of the information in the paragraph, represented as *(TS)*, *(S)*, *(C)*, or *(U)*.

There is no limitation on the length of the abstract. However, the suggested length is from 150 to 225 words.

14. KEY WORDS: Key words are technically meaningful terms or short phrases that characterize a report and may be used as index entries for cataloging the report. Key words must be selected so that no security classification is required. Identifiers, such as equipment model designation, trade name, military project code name, geographic location, may be used as key words but will be followed by an indication of technical context. The assignment of links, rules, and weights is optional.

Unclassified

Security Classification

3623-66